WARWICK
THE UNIVERSITY OF WARWICK

A Thesis Submitted for the Degree of PhD at the University of Warwick

Permanent WRAP URL:
http://wrap.warwick.ac.uk/90156

Copyright and reuse:
This thesis is made available online and is protected by original copyright.
Please scroll down to view the document itself.
Please refer to the repository record for this item for information to help you to cite it.
Our policy information is available from the repository home page.

For more information, please contact the WRAP Team at: wrap@warwick.ac.uk

warwick.ac.uk/lib-publications

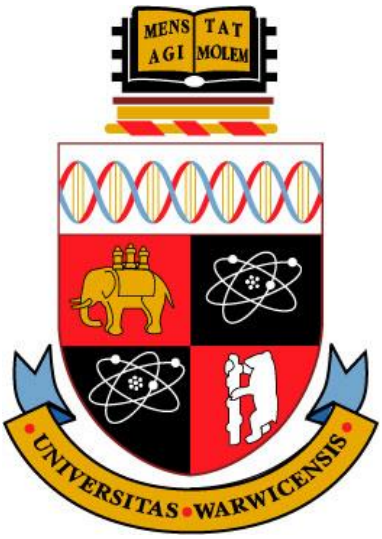

Development of an Artificial Neural Network (ANN) Based Phase Distribution Prediction Model for 22MnB5 Boron Steel during Tailored Hot Stamping

By

Prasun Chokshi

Thesis
Submitted to the University of Warwick
For the degree of
Doctor of Philosophy in Engineering
Warwick Manufacturing Group (March 2017)

THE UNIVERSITY OF WARWICK

Abstract

Due to demand for lower emissions and better crashworthiness, the use of boron ultra high strength steel (UHSS) has greatly increased in manufacturing of automotive components. However in many cases an idealized component has got different mechanical properties in different regions. For example in an automotive structural component such as B-pillar, which may undergo impact loading, it is desirable that there are certain regions in it which are softer and more ductile so that component's overall energy absorption is improved. The innovative process of tailored hot stamping allows for this by controlling the localized cooling rates, through actively dividing the tooling into heated and cooled zones. A barrier to optimal application of the technique is that a reliable phase distribution model is required to predict the distribution of different phases which occur in the different regions of a tailored hot stamped component. Currently most of the existing physical models for phase distribution prediction in boron steel after hot stamping only take into account the thermal history of the region while not accounting for the effect of deformation and thus have had only limited success so far.

This research has developed a novel state-of-the-art Artificial Neural Network (ANN) based phase distribution prediction model for 22MnB5 boron UHSS steel, which is able to successfully take into account both the thermal and mechanical history while making final phase distribution predictions during tailored hot stamping. The model was developed and validated using data generated from extensive tailored hot stamping thermo-mechanical physical simulation experiments and scanned surface instrumented nanoindentation based phase quantification method. For the development of the ANN based model, the backpropagation algorithm was deployed on the available experimental data from 40 thermo-mechanical physical simulation experiments to learn the complex multivariate functional relationship between the thermal and mechanical history of the samples and the final resulting phase distributions in them. Advanced statistical techniques were used for preventing overfitting in the ANN based model while learning, for making the optimal use of limited available experimental data and for quantification of uncertainties in the predictions made by the model.

After the ANN based model had been developed, its prediction performance was rigorously measured and analyzed. During measuring its prediction performance over the data used for its development, it had a prediction root mean square error of just 5.4% over 120 phase volume fraction predictions. During its validation over the completely new independent experimental data, the ANN based model had root mean square prediction error of just 7.7% over 30 phase volume fraction predictions. This excellent prediction performance of the developed ANN based model demonstrated its reliability and robustness and established the potential for ANN model to be used in future *computer aided engineering* applications for tailored hot stamping process.

Dedication

This work is dedicated to my loving sister who is the best sister that any brother can ask for and who has brought endless joy and happiness in my life. It is also dedicated to my mother for her limitless fortitude and her infinite wisdom

Acknowledgements

The author would like to acknowledge the following for their valuable help and support in this research work.

The University of Warwick and Tata Steel for supporting this project. In particular to my supervisors, Dr. Darren Hughes, Mr. David Norman and Prof. Richard Dashwood. Their help and guidance was invaluable and much appreciated.

Along with that the author is grateful for the valuable inputs provided for the project by Dr. Guido Hensen from Tata Steel IJmiuden Technology centre. The support offered by Dr. Zul Husain in preliminary Gleeble testing at Tata Steel Swinden Technology Centre is also acknowledged.

Author is also deeply grateful to Dr. Carl Slater for facilitating the final Gleeble testing at University of Birmingham and for all his support and assistance. Author also acknowledges the help of Dr. James Bowen and Science City Research Alliance for facilitating the instrumented nanoindentation testing at School of Chemical Engineering, University of Birmingham. Finally author thankfully acknowledges the assistance provided in the experimental work by the WMG workshop, University of Warwick.

Declaration

This thesis is submitted to the University of Warwick in accordance with the regulations for the degree of Doctor of Philosophy. It has been written by myself and has not been submitted in any previous application for any degree. All the work done in this thesis has been undertaken by me except where otherwise stated.

Table of Contents: (Page No.)

List of Figures: (Page No.)

List of Tables: (Page No.)

Chapter 1

Introduction

1.1 Background

Presently the automotive industry is faced with major contradictory challenges. On one hand there is a demand for increased passenger safety and more amenities in a car, whereas on the other hand engineers are required to come up with cars which consume minimal amount of fuel. Additionally the demand for increased passenger safety comes not only from consumers but also from stricter governmental passenger safety regulations. Similarly because of government's increasing focus on reducing CO_2 emissions and corresponding regulations, automobile manufacturers have to reduce the fuel consumption of their vehicles to meet the emission standards set by the government. Also the modern day consumers are becoming more and more environmental friendly & cost conscious and thus are demanding vehicles which give better mileage on the fuel. Faced with these conflicting requirements more and more automobile structural and safety components are being manufactured with ultra high strength steels (UHSS) [1].

Currently there is no globally accepted standard definition for ultra high strength

steels. However in the automotive industry, usually from a mechanical properties perspective, steels with tensile strength greater than 780 MPa are classified as ultra high strength steels [2]. Ultra high strength steels with their excellent strength to weight ratio are very well suited for helping the automotive industry in solving its dual problem of achieving increased passenger safety and reducing the fuel consumption of the car. They do so by light weighting of the car achieved through gauge reductions, while maintaining the structural integrity of the vehicle at the same time because of their high strength. Gauge reductions of the different structural components present in the body-in-white (BIW) leads to lesser amount of material being used in total, which in turn leads to reduction of the weight of the final automobile.

In the automotive industry, the 22MnB5 boron ultra high strength steel is the most widely used steel for making various structural and passenger safety components of the car by the hot stamping process [1-4]. This particular steel grade has excellent hardenability and after processing its final tensile strength (UTS) can be increased to more than 1500 MPa [4]. The final microstructure of the 22MnB5 boron steel after a conventional non-isothermal forming process consists of mainly martensite along with small amount of other phases [5]. It is this high martensitic content in the final microstructure of the boron steel, which leads to it achieving such high tensile strengths [6]. Since 22MnB5 boron steel is so widely used in the automotive industry, it is the material of focus for this research work and from

henceforth in this thesis it will be referred to as just boron steel.

The yield strength and tensile strength of the as received boron steel before processing are in the range of 350-400 MPa and 550-600 MPa respectively [8]. The as received hot rolled boron steel sheet microstructure has about 70-80% ferrite and the remaining 20-30% is pearlite [7]. The most common process by which the boron steel sheet is transformed into its final shape for making various automobile components is the direct hot stamping process [1]. In hot stamping terminology, a sheet of boron steel is commonly referred to as a blank. In this hot stamping process the boron steel blank undergoes both deformation and quenching at the same time inside the forming press.

Now based on the continuous cooling transformation diagram of the boron steel, the minimum cooling rate required for achieving a fully martensitic microstructure is approximately 27 K/s [9]. But this critical cooling rate is only valid when the boron steel does not undergo any plastic deformation. During the conventional hot stamping process the boron steel sheet undergoes both deformation and quenching simultaneously and it experiences cooling rates much higher than 27 K/s. This leads the final hot stamped parts to have a high martensite content in the final microstructure along with some presence of other phases like bainite and ferrite. Although it is the presence of the high martensite content in the final microstructure which ensures that the final parts have the desired high yield and

tensile strengths. In the Figure 1.1 given below, the microstructures of boron steel both before and after conventional hot stamping process are shown.

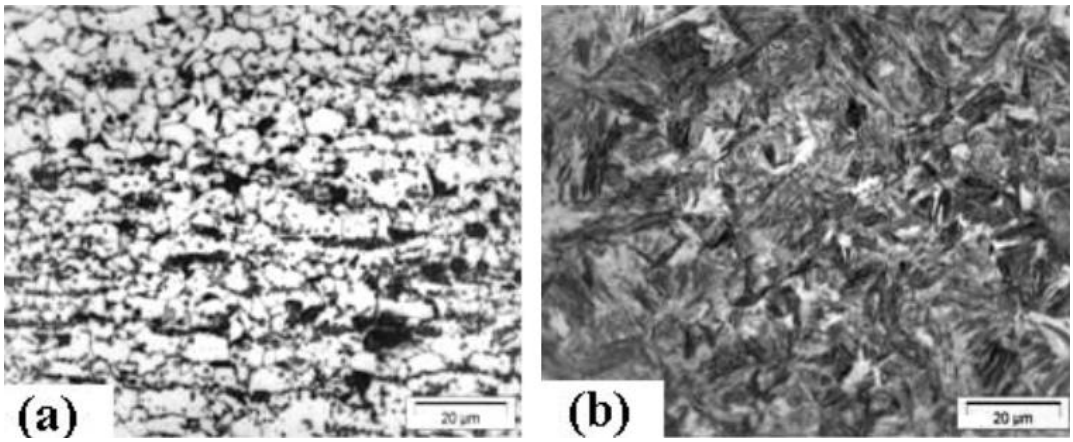

Figure 1.1: (a) Microstructure of boron steel before hot stamping and (b) microstructure of boron steel after hot stamping [21]

Thus the final resulting phases and their relative amounts in the final microstructure of hot stamped components are extremely important. It is the presence of those phases and their relative distribution, which determines the final mechanical properties of those parts. Now the final resulting phase distribution in a hot stamped component is directly determined by the thermal and mechanical history that the part undergoes during the hot stamping process. Controlling the hot stamping process parameters regulates the thermal and mechanical history of the hot stamped parts, which in turn controls the resultant phase distribution in the final microstructure of those parts.

Hence in order to obtain the desired final mechanical properties in the hot stamped parts, it is imperative to understand the functional dependencies between those processing parameters and the final phase distribution which results in the microstructure of those parts. Finally in order to put that knowledge to practical use, it is necessary to not just understand those functional relationships but also to develop a model which is able to quantify them. Developing such a model will help the industry to easily optimize the various hot stamping processing parameters so as to produce parts with desires mechanical properties, without needing to resort to extensive experimental investigations.

1.2 Ultra high strength steel parts in body-in-white (BIW)

Hot Stamping process was developed and patented by a Swedish firm (Plannja) in 1977 and was used for first time in manufacturing an automobile component in 1984 by Saab automobiles for the car Saab 9000 [10]. Hot Stamping is an innovative, non-isothermal forming process in which both forming and quenching occur simultaneously in a single step. This forming process results in the final hot stamped parts achieving very high tensile strength and that high tensile strength results in minimal springback after forming. Thus with the hot stamping process it is possible to manufacture automobile structural and safety components with complex geometries and very high final tensile strengths.

The number of hot stamped parts produced for the automotive industry increased from about 3 million parts/year in 1987 to over 107 million part/year in 2007 [11]. Since then the global production of hot stamped parts has been increasing at a steady pace in order to satisfy the ever increasing demand from the automotive industry. The hot stamped parts currently find application in cars as passive passenger safety and structural components like: A pillar, B pillar, rocker panel, front and rear bumper, side impact beam, tunnel, roof rail inner, subplate etc. Figure 1.2 shows the different structural and safety components in body-in-white of the modern automobile which are made using ultra high strength steel.

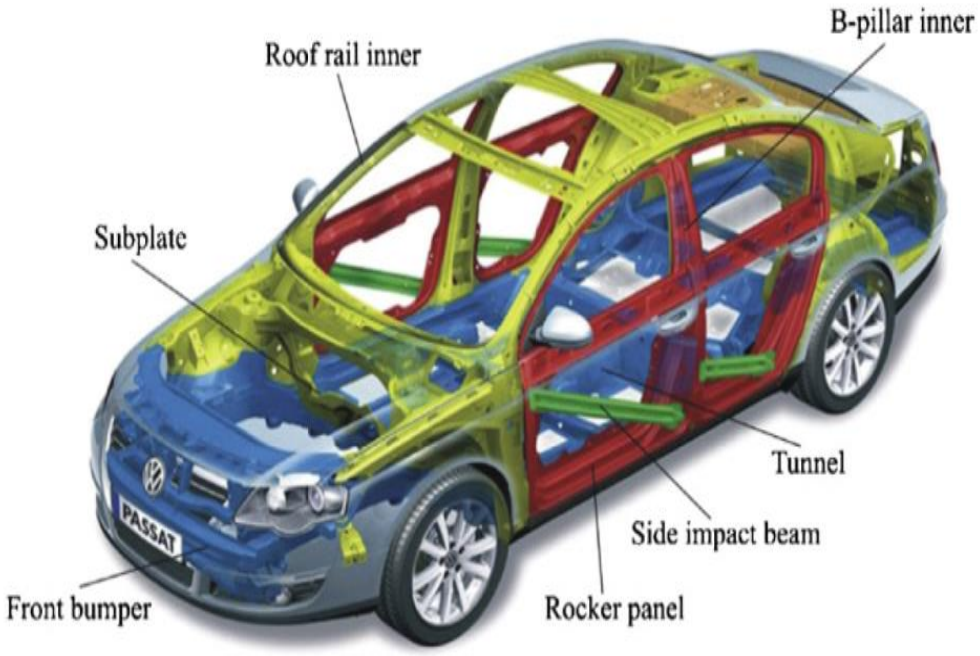

Figure 1.2: Hot Stamped parts in a typical automobile [1]

Volkswagen claims it was able to reduce the weight of its Volkswagen Passat B6 model by approximately 25kgs by using the hot stamped ultra high strength steel components in the car compared to using conventional steels components [12]. More and more automobile firms are trying to increase the percentage of ultra high strength steel components in their cars, so that it can help in weight reduction of the vehicle while at the same time not compromising on its structural integrity.

1.3 Hot stamping: Introduction

Hot stamping is an ingenious manufacturing process used by the automotive industry to produce automobile components with complex geometries and high strength. Hot stamping helps in overcoming the commonly faced challenge of spring back in cold forming, while simultaneously allowing for the hardening operation. Based on various technical and financial reasons, there are two variants of the hot stamping process which differ from each other in process methodology. These two major process variants are namely: Direct hot stamping process and Indirect hot stamping process [1].

In the direct hot stamping process, the blank is first heated in the furnace at temperatures of 900-950°C for a period which is sufficient to complete the transformation of the entire microstructure to austenite. Typically this takes about five to ten minutes before the complete transformation to austenite is finished [13].

Next the austenitized blank is rapidly transferred from the furnace to a forming press through air, during which some amount of air cooling takes place. Finally in the press the blank is formed and at the same time it is also quenched because of the high pressure contact with room temperature tooling. Due to complete metallic contact inside the forming press, very high cooling rates are achieved in the part which help in suppressing ferrite formation and promoting martensitic formation in the final microstructure.

In order to prevent the occurrence of decarburization and scale formation during the austenitizing heat treatment, the blanks are usually pre-coated with a layer of protective coating. One of the most widely used protective coating layers in the industry is the Al-Si protective coating, which is produced by hot dip galvanizing process and is made up of 87% aluminum, 10% silicon and 3% iron [14]. Other Zn based coatings can also be used but they are prone to inducing liquid zinc metal embrittlement when used for direct hot stamping [1].The protective coatings not only helps in protecting the surface from decarburization and scaling but also help with reducing friction & die wear and tear.

In the indirect hot stamping process, the parts are almost completely pre-formed to their final shape by cold forming. After that they are transferred to the furnace for austenitization. When austenitization is finished they are transferred to a secondary forming press where they undergo quenching and final shape calibration. Indirect

hot stamping allows forming for some highly complex geometries, which still aren't possible by direct hot stamping method because of the cracking which occurs in such parts as a result of the fast cooling rates involved during direct hot stamping process [16].

The Al-Si protective coating used for blanks has a lower forming limit then the steel at room temperature and so the coating cracks during cold forming [16]. This prevents coated steel blanks from being used for indirect hot stamping and leaves the pre-formed parts exposed to the oxidizing atmosphere inside the furnace, which leads to high amount of scaling. Thus another reason behind pre-forming in indirect hot stamping is to minimize the abrasive wear on the die surface by minimizing the relative movement of the surface of the uncoated oxidized blank with respect to the surface of the die. With the part being pre-formed to almost 90-95% of the final shape, the relative movement between the surfaces of the blank and the die is minimized during indirect hot stamping [15]. Thus in indirect hot stamping it is mostly quenching and steel hardening that occurs in the final step, as most of the forming has already been finished during the cold forming.

Direct hot stamping process offers several advantages over the indirect hot stamping process including lower forming stresses at elevated temperatures, minimal springback and a greater forming accuracy. Further the indirect forming process also leads to the addition of an extra processing step in the production

chain and thereby increases the production time for a single part. Because of all these disadvantages the use of indirect hot stamping within the industry has declined and it is only used when absolutely necessary [16]. Hence currently, the direct hot stamping process is the most widely used process within the automotive industry for forming ultra high strength structural components for the cars. Because of that, direct hot stamping process methodology will be the focus of this research work from here onwards. The various steps involved in both the direct and indirect hot stamping process have been shown in Figure 1.3:

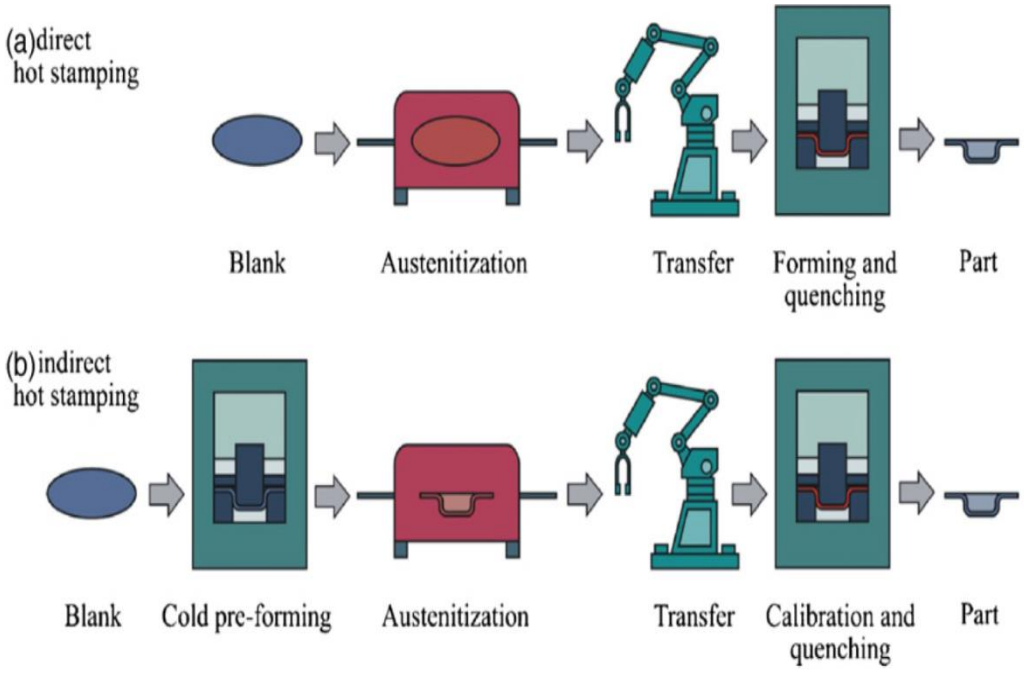

Figure 1.3: Hot stamping process chains: (a) Direct Hot Stamping (b) Indirect Hot Stamping [1]

1.4 Tailored hot stamping: Introduction

For the automotive industry, hot stamped parts with fully martensitic microstructure offer very high strength but limited ductility. Now for many applications in the automotive industry it is beneficial that only certain regions in a hot stamped part are fully hardened whereas other regions are required to have softer microstructure [17-19]. For example in an automobile passenger safety component such as B-pillar, which may undergo impact loading, it is desirable that there are certain regions in it which are softer and more ductile so that the component's overall energy absorption capacity is improved [17]. Figure 1.4 shows such a tailor hot stamped B-pillar with the desired mechanical property distribution for increased energy absorption:

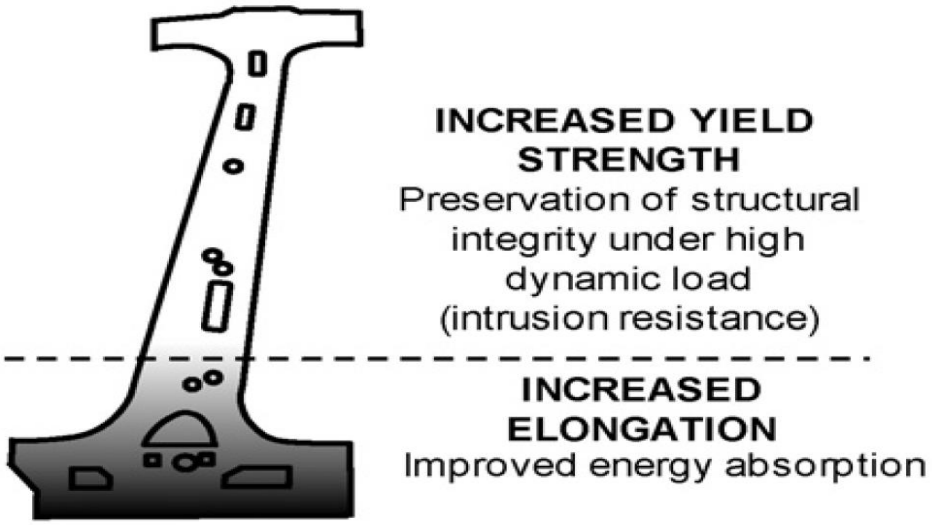

Figure 1.4: Tailor hot stamped B-pillar with tailored mechanical properties [18]

As can be seen in the Figure earlier, the top region of the B-pillar has high strength for excellent intrusion control whereas the lower region of B-pillar has increased ductility for greater energy absorption. Such components with “tailored” material properties in different regions have excellent crash performance and help in improving the crashworthiness of the vehicle significantly [18].

Munera et al. used a method called tailor welding in order to obtain such a tailoring of mechanical properties within a car component [19]. They tailor welded conventional hot rolled ultra high strength steel sheets with conventional low hardenability steel sheets before hot stamping. Thus the parts which were produced from such tailor welded blanks after the hot stamping process, had tailored mechanical properties which were functionally optimized at specific locations in the part. They created, tested and modelled the crash performance of such parts and found that parts with such tailored mechanical properties gave significant improvements in crash performance and weight reduction of the car [20]. These results and other similar results by various researchers showcased the importance of tailoring the mechanical properties within a component for improved crash performance and led to development of more efficient methods for tailoring the final mechanical properties in a hot stamped part involving differential cooling [17-20].

There are many different variations of the conventional direct hot stamping

process which produce parts with such tailored mechanical properties [17, 18, 31, 88-92, 93, 95, 96]. All these different variants use different process control strategies to vary the localized cooling rates during the hot stamping process. This is done in order to control the thermal history of a localized region, which in turn allows us to control the resultant phase distribution in those regions. All these different variants, which help in achieving such functionally optimized local mechanical properties in the final hot stamped parts, fall in the general category of the tailored hot stamping processes and will be further reviewed and critically analyzed in the next chapter (Chapter 2: Literature Review).

1.5 Aim and objectives

Thus tailored hot stamping is an important recent innovation in the hot stamping industry which is helping the automotive industry in maximizing the gains from using boron steel for manufacturing of automobile components. It improves upon the gains made in light weighting of the automobile by hot stamping process and helps in further improving the crashworthiness of the car. Tailored hot stamping process is at the cutting edge of manufacturing innovation, which is helping the automotive industry in meeting its dual objective of building lighter and safer cars for their customers. It is well known that the final mechanical properties of the part are a direct function of the relative distribution of martensite, bainite and ferrite phases in the final microstructure [1, 5, 6, 17, 88, 89]. Thus in order to fully realize

the complete potential of the tailored hot stamping process for the automotive industry, it is essential to develop a reliable model for predicting the final phase distribution in tailor hot stamped parts after their processing.

In the last decade, a few physical models have been developed for phase distribution prediction in boron steel after hot stamping process, but they have had limited success in solving this complex problem [17, 110-112, 114]. Since the final phase distribution within a tailor hot stamped component is a direct function of the complex interplay between the thermal and mechanical history of the component, it is imperative for a good model to take both of them into account while predicting the final phase distribution [17, 110, 114]. One of the main reasons for the limited success of most of these existing models was the fact that they took into account only the thermal history and not the mechanical history, while making the final phase distribution predictions [17, 110-112].

Thus this research work aims to develop a robust and reliable phase distribution prediction model for tailored hot stamping, which will be able to successfully take into account both the thermal history and the mechanical history of the formed part while making predictions about the final phase distribution. For achieving that objective, an Artificial Neural Network (ANN) based modelling approach has been investigated in this research. Artificial Neural Network (ANN) based modelling has the potential to take into account both the thermal and mechanical

history while making the final phase distribution predictions and has the capability to handle the kind of complicated thermal paths which arise during tailored hot stamping. This approach offers a completely new way of addressing this complex scientific & industrial challenge and hence this research work will be focussed on developing a novel state-of-the-art Artificial Neural Network (ANN) based phase distribution prediction model for tailored hot stamping process.

Developing such a model will allow us to robustly quantify the functional relationships between the thermal and mechanical history of the part and the final resulting phase distribution in it after tailored hot stamping process. Moreover in future for industrial *computer aided engineering (CAE)* applications, such an ANN based model can be coupled with data from thermo-mechanical Finite Element simulation and can be used for optimizing the tailored hot stamping process parameters. This will allow for tailored hot stamping process to produce automotive structural and safety components with the greatest potential for improvements in light weighting and crash worthiness.

1.5.1 Structure of Thesis

This thesis has been divided into a total of 7 chapters and the structure and focus of each chapter in this thesis is as given below:

Chapter 1: Introduction – This chapter gives an overview of the general concepts and topics related to this research work. This research work is highly

interdisciplinary in nature and it lies at the intersection of manufacturing, modelling and metallurgy. As a result of that various basic terminologies from these different fields have been introduced in this chapter, while at the same time giving a basic introduction to the motivation behind the work.

Chapter 2: Literature Review – This chapter contains the state of the art literature review for this research. It contains in depth technical reviews of the manufacturing, metallurgical and modelling aspects of this work, while at the same time introducing ANN based modelling and reviewing its applications to other materials processing/manufacturing problems in literature. Also this chapter discusses in detail the motivation behind this research arising from the literature review and states the significance and novelty of the work done for this research.

Chapter 3: Experimental Details – This chapter covers the experimental work done for physically simulating the tailored hot stamping process using Gleeble thermo-mechanical simulator. It also discusses the nanoindentation based surface scanning technique used for phase quantification and the metallography procedure used for secondary qualitative analysis of the phase distributions in the Gleeble test samples. This chapter is primarily focussed on describing in detail the experimental procedure followed and the data generated from the experimental work is discussed in the next chapter.

Chapter 4: Development of the ANN dataset – This chapter presents the data

generated from the experimental work and covers in detail the pre-processing done on that data for developing the final ANN dataset, which was then used for training and validating the final ANN model.

Chapter 5: ANN Model Development – This chapter gives the technical background for Artificial Neural Network (ANN) based modelling and then describes in detail the steps followed for developing the final ANN model for phase distribution prediction during tailored hot stamping. It covers the complete model development process right from model learning, model parameters tuning to quantifying the uncertainties in the final model predictions.

Chapter 6: Model Analysis and Discussion – In this chapter the prediction performance of the final ANN model is rigorously analyzed and discussed. The final ANN model is validated by comparing its predictions with completely new data obtained from separate independent Gleeble tests. This independent validation of the final ANN model on completely new data establishes its effectiveness as a robust, reliable model which can be used for engineering decision making. Also potential applications of the final ANN model are demonstrated to highlight the capabilities of the model for future industrial application

Chapter 7: Conclusions and Future work – In the final chapter, a concluding summary for this research work is presented along with suggestion for further work in this field.

Chapter 2

Literature Review

2.1 Overview

In this chapter, a state of the art literature review is presented for the current research work from manufacturing, metallurgical and modelling perspective. This chapter begins by thoroughly reviewing the different manufacturing aspects of the hot stamping process, which is then followed by an analysis of the metallurgy of boron steel. After that the metallurgical effects of the different process parameters on the phase distribution in final microstructure are reviewed, before moving on to a critical and thorough examination of different models that have so far been used for phase distribution prediction in boron steel after its processing. Following that Artificial Neural Network (ANN) based modelling is reviewed and its past applications for solving different problems in metallurgy/material science are discussed. Finally, since scanned surface instrumented nanoindentation technique has been used for phase quantification in this research work, a technical background on nanoindentation is provided. The chapter ends by providing the final summary of the literature review and highlighting the existing gaps in this research area, which the current work is expected to address.

2.2 Hot stamping: A manufacturing perspective

The manufacturing of high strength boron steel automobile components with desired distribution of mechanical properties requires a deep knowledge of the different facets of the hot stamping process. That knowledge and understanding allows for production of automobile components with desired levels of reliability and required mechanical properties distribution. The final product produced from a hot stamping process is a result of complex interplay between the mechanical, thermal and microstructural aspects of the manufacturing process. The hot stamping process can be divided into three main parts from a manufacturing process control perspective: Heating, Forming & Quenching and Post Processing.

2.2.1 Heating

The first step in the hot stamping process is to heat the blank to obtain a fully austenitic microstructure. Usually the blank is heated in the temperature range of 900 ºC to 950 ºC for approximately 5-10 minutes, so that a fully homogenous austenitic microstructure is obtained in the blank [22]. It is imperative to obtain a fully austenitic microstructure during the heating stage, in order to be able to control the phase distribution in the final microstructure when the austenite decomposes during cooling. The exact amount of austenitization time that a blank needs to get a fully homogenous austenitic microstructure is dependent on factors such as blank thickness and austenitization temperature [23]. As the blank

thickness increases, the amount of austenitization time required at a given fixed temperature also increases. The austenitization time required also increases with decrease in the austenitization temperature for a fixed blank thickness. The basic industrial objective is to obtain a fully homogenous austenitic microstructure in the minimum possible time and at minimum energy cost, so as to increase the production rate and the cost efficiency.

There are different heating systems which can be used for the austenitization process. The heating of the blank can be done using roller hearth furnaces, induction heating and conduction heating [1]. Figure 2.1 shows the system schematic of all the three different heating systems. Each heating system has its own advantages and disadvantages. At present the roller hearth furnace heating system is the one which is most widely used in the industry and most of the hot stamping lines across the world have a roller hearth furnace installed on them [1]. For the other heating systems, they are still mostly used at laboratory scale and for them research and development is still going on so that they are able to meet all the necessary conditions required for widespread industrial application.

In roller hearth furnaces the heating is done by radiation and convective flow of heat, which is generated using gas or electricity inside the furnace [24]. The blanks are brought in and heated inside the furnace while moving along on rollers. The speed of the rollers and the temperature difference between different chambers

inside the furnace controls the heating rate of the blanks. Usually the established roller hearth furnaces tend to be 30-40 meters in length and thus require large amount of space and large capital investments [1]. Also since the heating happens by radiation and convection, the heating rate is slow and that increases the time required to be spent by the blank inside the furnace. Thus there is significant interest in developing new heating systems which would allow for the austenitization process to be completed faster and cheaper.

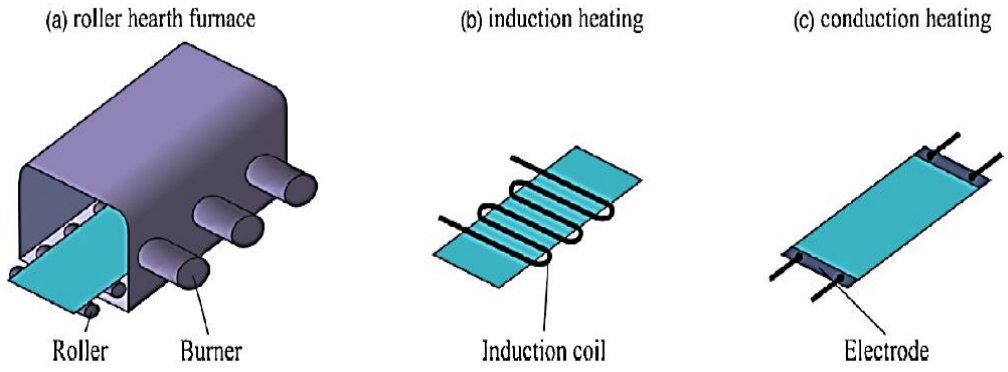

Figure 2.1: Heating Systems – (a) roller hearth furnace, (b) induction heating and (c) conduction heating [1]

An alternative heating system on which ongoing research is being carried out is the conduction heating system. In this heating system, two electrodes are connected to the blank and current is passed through the blank [25]. The blank heats up because of its high resistance and the amount of heat generated is proportional to the loss of energy. As this method uses the resistance of the blank to generate heat from electrical power, it is also called the resistance heating

method. A key consideration to be taken into account while deciding about the application of this heating method is its efficiency, which is in turn dependent on the resistance characteristic of the part. Usually longer parts have higher resistance as compared to shorter parts and hence this heating method is generally suiTable for parts with favorable length/diameter ratio [26]. This method offers several advantages such as very high heating rates, minimal space requirement and lower cycle times. However there is a major challenge that this method needs to overcome before it can be successfully applied for widespread industrial use and that challenge is to achieve a homogenous temperature distribution in blanks with complex geometries during conduction heating [27].

Another heating system, which is currently being investigated, is the induction system which can be used for any material which is electrically conducting or semi-conducting. Induction heating is a well-established technique and is widely used for various applications like melting, tempering and heating of metals for bulk metal forming [29]. Induction heating system mainly comprises of a high frequency generator and an induction coil. When the sheet metal enters the induction coil, eddy currents are generated within the sheet metal and this eddy current then is converted into heat. The amount of eddy currents that are generated in the material depends on the operating frequency, electrical conductivity and the magnetic permeability of the material [28]. There are other factors such as the geometry of inductor and distance between the inductor and the sheet metal which

also affect the efficiency of the induction heating process. Kolleck et. al [29] have proposed a two-step induction heating device for austenitization of uncoated boron steel sheet blanks, which significantly reduced the heating time while giving similar results as obtained by traditional heating methods. Further investigations are required to find the suitability of this heating method for austenitization of the widely used Al-Si coated blanks. For the hot stamping purpose, induction heating system continues to be used mainly at the laboratory scale.

2.2.2 Forming and quenching

After the austenitization process finishes in the furnace, the blank is transferred from the furnace to the forming press. During this transfer the blank is exposed to air and thus air cooling takes place. There is a drop in the temperature of the blank and so usually the aim is to transfer the blank from furnace to the forming press as soon as possible. This is required as the forming process should be finished before the start of the austenitic decomposition. Furthermore, the higher the deformation temperatures, the lower are the loads required to form the sheet metal into its final shape.

Once the blank is formed at high temperatures inside the press, then quenching takes place inside the closed tooling. Due to full metallic contact between the formed blank and the tooling system, very high cooling rates are achieved [30].

All the heat of the blank is dissipated through conduction into the tooling system which is in contact with the formed blank. Repeated stamping leads to the increase in the tooling temperature and thus ducts are used in the tooling system to pass a coolant and take the heat out of the tooling system to maintain its temperature [30, 32]. Water is one of the most common coolants which is used during hot stamping for maintaining the tooling temperature [30, 32]. The quenching process inside the tooling system is one of the most important part of the hot stamping process as it directly controls the final mechanical properties of the part.

The thermal history of the formed part is dependent on the heat flow from the formed part to the tooling system and from tooling system to the coolant. For optimum heat transfer from the part to the tooling system, there shouldn't be any scaling or gap on the contact surface. Other important factors which govern the heat flow between part and the tooling system are the thermal conductivity of the tool material and the design of the cooling ducts. Design of cooling ducts includes the size, location and the distribution of the cooling ducts. Using lower temperature coolants in the ducts increases the heat flow rate from the tooling system to the coolant, and thus leads to achieving higher cooling rates inside the press for the formed parts [30]. Demands for higher efficiency and faster process cycle have led to development of tool steels with higher thermal conductivity and more efficient cooling systems [31, 32].

2.2.3 Post processing

Once the part has been formed and quenched in the hot stamping press, the next steps in the production process chain involve cutting and joining of the part. Due to the high mechanical strength achieved by the part during its forming, laser cutting is the most commonly used method for cutting/piercing. Using laser cutting offers advantages such as reduced limitations on the shape of the part to be trimmed and no wearing of the tool. The amount of time it takes for laser cutting is dependent on the complexity of the geometry of the final part and the speed and agility of the laser machine [33].

Other methods used for post-processing includes hard cutting and warm cutting [34, 35]. Hard cutting employs conventional mechanical blanking methods and it results in high wear of the blanking tool because of the high strength of the part. The final quality of the sheared surface and the dimension precision in the blanking method depends on process parameters such as punch speeds, blanking angles, punch-die clearances, tool cutting edge geometries and the mechanical properties of the material [34]. The warm cutting method involves cutting at higher temperatures during the quenching step itself and this leads to lesser cutting force being required and also a shorter process chain. Any of these discussed methods can be employed in the real world depending on various factors like geometrical complexity of the final part, costs and process efficiency.

Now due to low formability of the hot stamped parts, welding is the most commonly used joining method [1]. Thus good weldability is a necessary pre-condition for the hot stamped parts. Resistance spot welding is one of the most commonly used method amongst the different welding methods [36]. Both Al-Si coating and Zn based coatings work well with resistance spot welding and neither of those coatings affect the final weldability of the product. For Zn based coatings, the double pulse technology along with DC source gives the best spot welding results [37]. Other methods such as laser welding, stud welding and brazing can also be used for Zn based coatings [37].

2.3 Metallurgy of boron steel

The demand for better crash performance and greater fuel economy has led the automotive industry to focus on light weighting of automobiles. This focus has resulted in increased use of ultra high strength steel by the automotive industry to manufacture various automobile components. SuiTable heat treatment of low and medium carbon alloy steels can in principle lead them to achieving such ultra high strengths after processing. Such heat treatments would involve austenitization of the steel followed by its rapid quenching. However cooling rates in excess of 300°C/s are required during quenching, to achieve such high strengths for low and medium carbon steels [38]. Achieving such extreme cooling rates during thermo-mechanical processing is very challenging and hence such low and medium carbon

steels are not suiTable for the purpose. Different alloying elements such as vanadium, molybdenum, tungsten, chromium or manganese can be added to the steels to improve their hardenability [39]. However such alloying elements need to be used in large quantities in order to achieve desired properties in the steels and that results in either increased costs or poor manufacturability.

On the other hand, typically adding a very small amount of boron significantly improves the hardenability of the steel without adversely affecting its manufacturability and is a cost effective solution to the problem [40]. The critical cooling rate required for achieving ultra high strength in such boron steel is around 30 K/s, which is easily achievable during the normal processing. Furthermore the low carbon and low alloy content of the boron steel is great for the weldability of the final part. Thus boron ultra high strength steel is the most widely used steel in the automotive industry for the hot forming process. The typical chemical composition range of boron steel used within the automotive industry is as given in the following Table [38].

Table 2.1: Typical chemical composition range of boron steel used in automotive industry for hot stamping process(wt %) [38]

C	Mn	Si	Cr	Ti	B	Mo	Al
0.18-0.42	0.60-1.30	0.15-0.35	0.0-0.40	0.03-0.08	0.001-0.003	0.0-0.05	0.02-0.08

Each of the alloying elements added to the steel plays an important role in determining the final mechanical properties of the steel. These alloying elements govern the behavior of the steel both during its production and also during its processing. The principal metallurgical effects of some of the commonly used alloying elements on strength and ductility of the steel are detailed below [41, 42]:

- Carbon – Usually carbon as an alloying element helps in increasing the hardness and tensile strength of steel. Though at the same time the weldability and ductility of steel goes down with increasing carbon content of the steel. Different alloying elements are used in combination along with carbon to achieve the final desired properties in steels.

- Manganese – Manganese is present in most carbon and alloy steels. It also helps in increasing the strength and hardness by substitutional hardening. The effectiveness of manganese in improving the hardenability of steel is dependent on the carbon content of the steel. Again increasing manganese content leads to decrease in weldability and ductility but not as significantly as carbon.

- Silicon – During steel making, silicon plays the role of the primary deoxidizer. It stabilizes ferrite and retards volume change to martensite during tempering.

- Chromium - Chromium is widely used in steel for improving its corrosion and oxidation resistance. It also helps in increasing the hardenability of the steel and its wear resistance. Chromium is often used with a toughening element like nickel to produce steel with higher quality mechanical properties. Furthermore chromium leads to formation of sTable chromium carbides and helps in retarding softening during tempering of steels.

- Titanium – Titanium as an alloying element helps in improving the toughness characteristic of the steel by helping in controlling grain growth during austenitization by formation of TiC and TiN precipitates. It also helps in improving toughness by improving the characteristics of inclusions in the steel.

- Molybdenum – Molybdenum is a potent substitutional hardening element, which helps in increasing the strength and hardness of the steel. It also helps in minimizing temper embrittleness and delaying softening during tempering. Molybdenum also helps in improving the creep performance of low alloy steels at high temperatures.

- Aluminium - Aluminium is another deoxidizer which is added during steel making and also helps reduce porosity during casting. It is also quite effective in controlling grain growth in steels during austenitization by forming sTable precipitates.

All these different alloying elements discussed above play their respective roles in boron steel during its processing to varying degrees. However the single most important alloying element in boron steel, which has made it the most widely used steel in the automotive industry, is boron.

Boron is one of the most potent elements for increasing the hardenability of steel. Addition of just a small amount of boron significantly enhances the hardenability of low carbon, low alloy steel [43, 44]. Boron enhances the hardenability of steel by segregating to the austenite grain boundaries and hindering the nucleation of ferrite. One of the proposed explanation for the phenomenon is the solute boron atoms on the austenite grain boundary lower the surface energy of the austenite grain boundaries and thus makes those sites unfavorable for ferrite nucleation [45, 46]. As a result this leads to ferrite nucleation being delayed, which leaves more austenite available for transformation to martensite and thus leading to increased hardenability of the steel. The optimum boron content for maximizing the hardenability in steel is about 10-30 ppm [47]. It is believed that increasing the boron concentration above this range would lead to formation of $Fe_{23}(C,B)_6$ borocarbide precipitates on austenite grain boundaries, which can act as preferential nucleation sites for austenite to ferrite transformation. This would lead to increased ferrite nucleation during cooling and thus decrease the hardenability of the steel [48].

There are two different mechanisms by which boron atoms can segregate to the austenite grain boundaries in boron steel: 1. Equilibrium type segregation and 2. Non-Equilibrium type segregation [49]. Equilibrium type segregation takes place during isothermal holding and is particularly effective at holding temperatures lower than 700°C. Above those temperatures the severity of the equilibrium type segregation decreases significantly and also it is not sensitive to cooling rates experienced after holding temperatures. Non-equilibrium type segregation occurs during cooling from elevated temperatures and its severity increases with higher quench temperatures. Non-equilibrium segregation leads to formation of a boron depleted zones near segregated regions and the width of this zone is sensitive to the cooling rates. Thus at lower temperatures it is the equilibrium type segregation which is the dominant mechanism, whereas the non-equilibrium type segregation mechanism plays an important role in samples which are cooled from higher temperatures [50].

In the equilibrium type segregation, the atom concentration at the grain boundary at equilibrium level (C_e) is given by the following equation [50]:

$$C_e = A\, C_0\, e^{Q/RT} \qquad (2.1)$$

where Q is the binding energy between grain boundary and the solute atom, C_0 is the solute concentration in the matrix and A is constant related to vibrational entropy. Based on this model, as the temperature is increased the equilibrium

concentration of the segregated atom decreases exponentially. Conversely when the samples are cooled then the segregation level increases and gradually reach a new equilibrium level associated with the lower temperature.

According to the non-equilibrium segregation mechanism, the boron atoms are transported to the austenite grain boundaries during cooling by motion of excess vacancies towards grain boundary. In this mechanism, the amount of segregated atoms at the grain boundaries is determined by the number of vacancy-solute complexes annihilated at the interface during cooling. The severity of segregation which occurs by the non-equilibrium type mechanism is directly proportional to the quench temperature and inversely proportional to the cooling rate. High temperature deformation before quenching leads to increased concentration of vacancies and thus during subsequent cooling the non-equilibrium segregation process is intensified

In Figure 2.2, it is shown that how these two segregation mechanisms are dependent on the quench temperature. Curves A and B in Figure 2.2 above depict the dependence of equilibrium and non-equilibrium mechanisms as a function of quench temperature respectively. And the overall level of boron segregation, which is the resultant effect of both the mechanisms at a given temperature, is represented by curve C. As shown in the Figure, the non-equilibrium mechanism dominates at higher temperatures, whereas the equilibrium mechanism is dominant

at lower temperatures. Based on the thermal history that a blank of boron steel follows during the direct hot stamping process, the dominant mechanism by which boron segregation occurs during hot stamping is expected to be the non-equilibrium segregation mechanism [51].

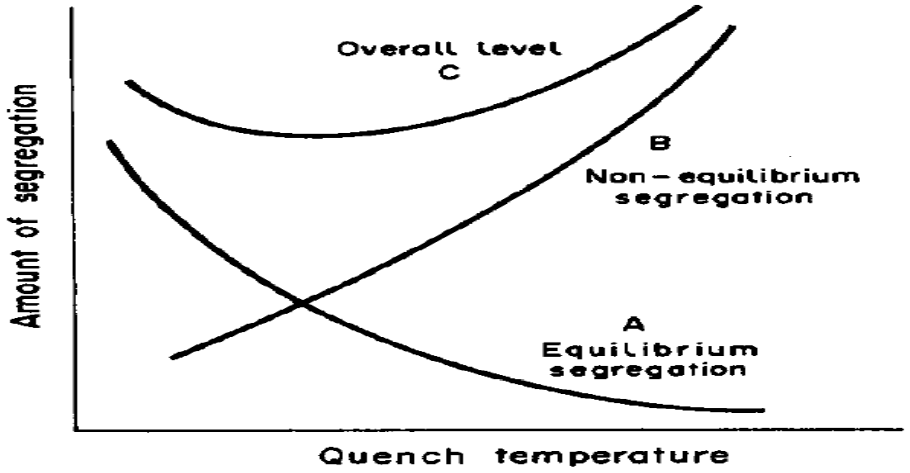

Figure 2.2: Dependence of the segregation mechanisms and overall segregation on the quench temperatures [50]

2.4 Microstructural evolution during hot stamping process

The as-received microstructure of the boron steel consists mainly of ferrite and pearlite. Due to the hypo-eutectoid nature of the boron steel, the amount of ferrite is significantly greater than the amount of pearlite in the initial microstructure [52]. The boron steel undergoes two major phase transformations during the hot stamping process. The first phase transformation takes place when the boron steel is heated inside the furnace. During this stage the steel blank is kept inside the

furnace and its temperature increases from the room temperature to the austenitization temperature. The austenitizing temperature is usually kept between 900-950 degrees Celsius to ensure that complete austenitization takes place in the microstructure. As the temperature of the blank crosses the Ac1 temperature, austenite grains nucleate and start to grow in the microstructure. Keeping the blank at the austenitizing temperature for approx. 5-10 minutes ensures that the entire microstructure gets converted in to austenite phase [22].

The second major phase transformation takes place during the cooling of the blank. As soon as the blank is taken out from the furnace and transferred to the forming press, the cooling of the blank begins. When the blank is formed into its final shape inside the hot stamping press, there is full metallic contact between the blank and tooling and it undergoes rapid quenching. During this period when the temperature of the blank drops from austenitization temperature to room temperature, the austenite phase decomposes into martensite, bainite and ferrite. This is the most critical phase transformation for boron steel as it largely determines the final phase distribution in microstructure of the hot stamped part.

The continuous cooling transformation (CCT) diagram of 22MnB5 boron steel is shown in Figure 2.3. As can be seen from the diagram, different cooling rates lead to different phases being produced in the final microstructure during austenite decomposition. A cooling rate of at least 30°C/s is required to achieve complete

martensitic transformation in the microstructure during the quenching step. This critical value of 30°C/s is only valid for boron steel which is not subjected to any kind of deformation. However during hot stamping, the sheet metal is subjected to deformation and this leads to shift in the CCT diagram to left, which increases the minimum required cooling rate for complete martensitic transformation [54].

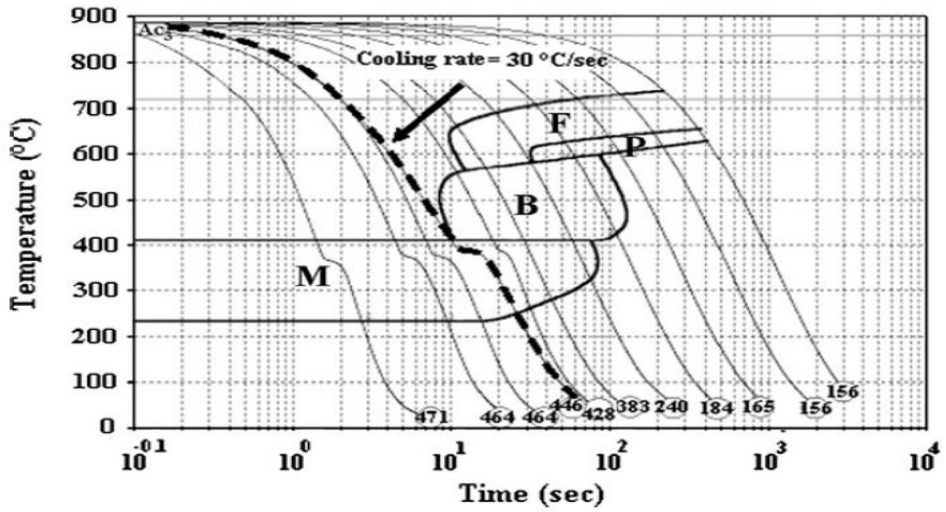

Figure 2.3: CCT diagram of boron steel [53]

2.5 Effect of process parameters on final phase distribution

As discussed in the earlier section the phase transformations which take place in the steel blank once it is taken out of the furnace after austenitization, that is what determines the final resulting phase distribution in the hot stamped part. There are several hot stamping process parameters which affect these phase transformations and thus play a key role in determining the final phase distribution [52, 55, 56].

Each of those hot stamping process parameters affects the final phase distribution to varying degrees. The three most important hot stamping process parameters which play the most significant role in determining the final phase distribution from a process control perspective are: (1) Cooling rate parameter, (2) Deformation amount parameter and (3) Temperature of deformation parameter. [17, 18, 30, 31, 52, 55, 66, 76, 84, 86, 88, 89, 110, 114]

2.5.1 Effect of cooling rate during hot stamping

Cooling rate is one of the most important factors which affect the evolution of the microstructure of boron steel during hot stamping after austenitization [57, 58]. The evolution of microstructure in undeformed boron steel as a function of the cooling rate can be tracked with the help of its CCT diagram. As can be seen from the CCT diagram of boron steel, very low cooling rates are required to obtain a ferritic-pearlitic microstructure. Typically for getting such microstructures cooling rates less than 6°C/s are needed. Cooling rates higher than that but lower than the critical cooling rate of 30°C/s lead to a pre-dominantly bainitic microstructure. Finally cooling rates greater than the critical 30°C/s lead to a heavily martensitic microstructure [59].

In the hot stamping process the blank does not follow a single uniform cooling rate during its processing. Indeed the thermal path followed by the blank during hot

stamping is complicated. After austenitization the blank is transferred from furnace to the forming press. Initially during transfer of the blank from furnace to the press, it undergoes air cooling. The cooling rate during this transfer period is low and varies between 10-20 °C/s depending on the temperature of the blank. No significant phase transformations takes place in this period because of the suppression of ferrite nucleation by boron atoms segregating to austenite grain boundaries [60]. Thus the microstructure is still largely austenitic, when the blank reaches the hot stamping press from furnace.

Once inside the forming press, the blank is formed and quenched at the same time. The deformation which occurs during forming significantly affects the CCT diagram of the boron steel [61]. The effect of deformation on the microstructural evolution in boron steel is discussed in detail in the next section. During forming the blank comes into full metallic contact with the die & punch and that leads to a sudden increase in the cooling rate as compared to the air cooling rates experienced by the blank during transfer from the furnace to the press. The exact nature of the thermal path followed by the blank inside the press is determined by this simultaneous forming and quenching step. It is during this part of the process that austenite starts to decompose into different daughter phase fractions.

Furthermore, inside the press the cooling rate followed by the blank is not uniform. Initially the temperature difference between the temperature of the

formed part and the temperature of the die & punch is greater and it leads to faster cooling rate. The cooling rate experienced by the formed part decreases as its own temperature decreases [62]. Thus the thermal path followed by the blank inside the forming press is complex and cannot be accurately represented by just a single uniform cooling rate.

The thermal paths which the blank follows inside the forming press can be controlled and varied. The different methods by which they can be controlled inside the press are discussed in detail in the forthcoming section on tailored hot stamping. The final resulting phase distribution in the part at the end of the process is heavily dependent on the thermal path followed by it inside the forming press and thus controlling that thermal path is the most important factor for controlling the final phase distribution [63, 64].

2.5.2 Effect of amount of deformation

Once the blank has been transferred from furnace to the forming press, there it is formed and quenched simultaneously. During transfer from the furnace to the press the temperature of the blank decreases by loss of heat to the surrounding air. Thus the temperature at which deformation actually occurs is dependent on the transfer times. Usually in the industry, the aim is to minimize the transfer time so that the deformation takes place when the blank is still in fully austenitic conditions [65].

In this temperature range the austenite phase is undercooled and has a higher Gibbs free energy than its daughter phases. Thus application of plastic deformation to undercooled austenite phase increases its free energy even more and this further increases the driving force for transformation of deformed austenite. This leads to lower starting time for each of the transformations and is captured by the shift of the CCT diagram to the left in response to the applied deformation [66]. This phenomenon of the CCT diagram of the boron steel shifting towards left in response to applied deformation during forming, is further intensified when the deformation occurs at lower temperatures. It has been reported in the work of Min et al [67] that the deformation of 22MnB5 boron steel at 650°C leads to deformation induced ferritic transformation even with application of strain values as small as 0.044. Also at such low deformation temperatures, the volume fraction of deformation induced ferrite was found to increase with increasing applied strain levels. Though the general trend of ferrite content increasing with increasing deformation has been reported in the literature [68, 69], the effect of deformation on the ferrite content is not independent of other hot stamping process parameters such as cooling rate, strain rate and deformation temperature. At the high deformation temperatures, cooling rates and strain rates experienced by the boron steel blank inside the forming press in the industry, the positive effect of deformation on ferrite formation is significantly suppressed and leads to low ferritic content in the final microstructure [70, 76].

The deformation of boron steel produces undercooled austenite with high Gibbs free energy which is highly unsTable. Because of the high deformation temperatures, cooling rates and strain rates experienced by the boron steel blank inside the press, the austenite does not get enough time to transform to ferrite and thus the microstructure still has got significant amount of untransformed austenite when it enters the bainitic region during cooling. The equilibrium bainite start temperature (Bs) for undeformed boron steel is about 575°C [69], but usually the pre-deformation of austenite phase leads to an increase in bainite start temperature [55, 71]. It has been reported by Jin et al. [72] that deformation of austenite above the Bs temperature leads to significant reduction in its incubation period and this is what leads to the rise of bainite start temperature. There are still no definitive conclusions available about the exact nature of the bainitic transformation in spite of several investigations [73, 74]. Two different models, based on diffusional transformation and displacive transformation mechanism respectively, have been proposed to explain bainitic transformation. Based on their work, Hsu et al [75] proposed that bainitic transformation is more diffusion driven in the temperature range from Bs to bainite nose temperature and closer to the Ms temperature it is more driven by displacive diffusionless mechanism. Others have proposed that bainite phase nucleation is assisted by carbon partitioning in austenite by diffusion and after that the bainitic phase grows by displacive/shear transformation. Most probably the mechanism of bainitic transformation is a mixture of diffusional and displacive transformations [76].

The effect of austenite deformation on bainite formation in the final microstructure is complicated. On one hand the hot pre-deformation of austenite leads to increased driving force for bainitic transformation because of increased stored free energy in deformed austenite. Hot pre-deformation also leads to increased dislocation density, subgrains and increased grain boundary area by grain refinement, all of which provides additional preferential sites for bainite nucleation. This significantly shortens the incubation period for bainite nucleation and pushes up the bainite start temperature [72]. Thus on one side the austenite deformation helps in accelerating the rate of bainite transformation. On the other hand it has been reported that the pre-deformation of austenite can lead to retardation of the growth of bainite phase and in certain cases it can even manage to stop the bainite transformation [77]. The dislocations generated during deformation of austenite can adversely affect the oriented growth of bainite and thus hinder the bainitic transformation by a phenomenon similar to the mechanical stabilization of austenite observed for the martensitic transformation. Although several authors have suggested that the exact mechanism of mechanical stabilization of austenite for bainitic transformation is different from that for martensitic transformation [78, 79]. Thus the final resultant effect of austenite pre-deformation on bainite content is determined by the opposing forces of the two phenomena described over here.

The effects of deformation on the final bainite content and other phases for

22MnB5 boron steel were investigated by Nikravesh et al. [76] through physical simulation of hot stamping process using Baehr 805 deformation dilatometer simulator. It was reported that in the range of cooling rates of 2-6 °C/s, the amount of bainite content available in the final microstructures of deformed and non-deformed samples was similar. But at cooling rates higher than this the bainite content in the deformed samples was greater than that in non-deformed samples. Thus at cooling rates higher than 6 °C/s, the positive effect of deformation on bainitic transformation was dominant and lead to a greater bainitic content in the final microstructure.

The effect of deformation on martensite start and finish temperatures and the final martensite content for 22MnB5 steels have been investigated in detail in previous works [52, 55, 76, 80]. Martensitic transformation is a military displacive transformation, which involves simultaneous coordinated movement of atoms [81]. Such kind of military transformation is hindered by defects like dislocations and grain boundaries present in the microstructure [82]. During the hot pre-deformation of austenite, the density of such defects in the microstructure increases significantly and this leads to stabilization of the austenite phase. This phenomenon is referred to as mechanical stabilization of austenite, which can retard or even impede the martensitic transformation [83]. Thus even greater driving force is required for martensitic transformation to occur and this leads to the lowering of martensite start temperature during hot pre-deformation of

austenite. This same mechanical stabilization of austenite phenomenon also leads to reduction in the final martensite content of the microstructure with increasing amount of deformation in 22MnB5 boron steel during hot stamping, with all other factors being the same [52].

As discussed in this section, the amount of hot pre-deformation has a significant effect on the phase transformations that happen in boron steel during hot stamping. Also this deformation amount parameter further interacts with the thermal path being followed by the blank inside the press to make matters even more complicated, when trying to predict the final resulting phase distribution after hot stamping. Thus any model trying to make predictions about the final resulting phase distribution in boron steel after hot stamping, needs to take into account both the effect of deformation and the effect of deformation's interaction with the thermal history while making those predictions.

2.5.3 Effect of temperature of deformation

The temperature of deformation is a process parameter which captures the starting point of interaction of the thermal history with the deformation amount parameter during the hot stamping of the blank. It plays a significant role in determining how exactly the deformation amount parameter interacts with the thermal history and what is the result of that interaction on the final phase distribution. The

temperature of deformation is determined by the amount of time taken to transfer the blank from furnace to the forming press. During this transfer time air cooling of the blanks take place and thus the deformation of the blank does not occur at the austenitization temperature but at lower temperatures. The usual temperature range in which the forming takes place during hot stamping is between 850-700 °C [52].

Lower deformation temperatures lead to the austenite phase getting significantly undercooled. This further increases the stored Gibbs free energy of the austenite phase and this increases the driving force for the unsTable austenite phase to decompose into its daughter phases. Naderi et al [52] reported that decreasing the temperature of deformation directly results in decreasing amount of martensite in the final microstructure. Flow stresses are higher at lower temperatures for boron steel and thus for same amount of strain and strain-rate, deformations at lower temperature lead to a greater increase in the stored free energy of the austenite phase [13]. This increase in stored free energy by deformations at lower temperatures supports the positive effect of deformation on bainitic transformations, especially in the cases where no ferrite has been formed in the microstructure before [84]. Also deformations at lower temperature increase the effect of plastic strain on the microstructure and results in greater dislocation density and subgrain structures. All this leads to greater mechanical stabilization of austenite when it is deformed at lower temperatures. Thus this increased mechanical stabilization and lower availability of austenite leads to less amount of

martensite being formed in the final microstructure of boron steel deformed at lower temperatures during hot stamping [86].

2.5.4 Other process parameters

Besides the process parameters described above, there are certain other process parameters in hot stamping which influence the final resulting phase distribution in the microstructure of boron steel during hot stamping to a lesser degree. These process parameters include the austenitization temperature, austenitization time, rate of deformation and quench duration. The effects of these process parameters on the final phase distribution of boron steel after hot stamping have been studied and reported in the literature [17, 52, 85, 86].

It has been reported that the hardenability of boron bearing steel decreases as the austenitization temperature increases above the 900-950°C temperature range [84]. Grain coarsening and greater boron segregation at higher austenitizing temperatures lead to the precipitation of borocarbides at the austenite grain boundaries, which lead to the decrease in the hardenability of the steel. Similarly increasing the austenitization time also leads to grain coarsening which adversely affects the hardenability of the boron steel. Also increasing both the austenitization temperature and austenitization time would lead to an increase in the energy costs associated with the hot stamping which is not desirable. It has been reported in

various works that the austenitization temperature range of 900-950°C and austenitization time of 4-5 minutes is the ideal combination for boron steel which ensures maximum hardenability and which also helps in preventing occurrence of any significant grain coarsening in the austenite phase [65, 85, 86].

The rate of deformation in hot stamping process is determined mainly by the speed of the punch. According to geometry of the die, different parts of the blank experience different strain rates during the hot stamping process. For similar thermal histories, increasing the strain rate has a negative effect on the ferrite transformation. Very low ferrite content is obtained in the final microstructure of boron steels deformed at strain rates of above $0.5s^{-1}$ in the usual hot stamping deformation temperature range [69]. In the low strain rate regions, the time taken for deformation to finish allows ferritic and bainitic transformations to occur in the microstructure. Thus at such low strain rates the dominant phases in the microstructure are ferrite and bainite and increase in the strain rate leads to lesser amount of time being available for diffusion based phase transformations to occur.

In high strain rate value regions, usually the dominant phase in the microstructure is bainite. At such high strain rates there is very little time available for ferritic transformations at high temperature and at the same time the effect of mechanical stabilization of austenite becomes more dominant with respect to martensitic transformations. Thus bainite ends up being the dominant phase in the

microstructure, with increasing strain rates leading to fall in the martensite phase fraction values in the high strain rate region. Overall the influence of strain rate on the final phase distribution of boron steel becomes quite less pronounced at high strain rate values above $0.5s^{-1}$ during the hot stamping process [52]. It is common that high punch speeds are used in the industry for hot stamping in order to reduce the processing times for individual blanks. This leads to high strain rate values in most parts of the blanks and thus this process parameter has a limited influence on the final phase distribution in the hot stamped parts.

Finally, quench duration in hot stamping process is determined by the amount of time spent by the formed part inside the stamping press before its removal. It has been reported in the literature that the formation of martensite could be adversely affected by shorter quench times, if the temperature of the part is higher than the martensite start temperature when it is removed from the stamping press [17]. Higher quench durations lead to formation of greater martensite during conventional hot stamping by faster and greater heat extraction through full metallic contact cooling between the formed part & the room temperature tooling.

2.5.5 Summary

As discussed in this section, the different hot stamping process parameters affect the evolution of the final microstructure in the boron steel during hot stamping

process. The complexity in predicting the final phase distribution arises from the fact that all of these individual process parameters come together during the hot stamping process and each of them has an impact on the phase transformations happening inside the microstructure. Additionally, all these various process parameters also interact with one another and those interactions too exert their influence on the phase transformations. Thus the final phase distribution in the microstructure of the hot stamped part at the end of the stamping process is a result of the complex interplay between all these different processing parameters.

2.6 Tailored hot stamping process variants

The parts produced by the conventional hot stamping process usually have high tensile strengths in the region of 1500-2000 MPa because of fully martensitic microstructures obtained at the end of the process. However in the recent years, it has been discovered that the crash performance of hot stamped parts can be significantly improved by *tailoring* the mechanical properties of the different regions within hot stamped parts [18-20, 88, 89]. Having regions of low strength and high ductility at strategic locations within the hot stamped parts, as demonstrated in Figure 1.4 in Chapter 1 earlier in this thesis, greatly helps in improving the stamped part's overall energy absorption performance. This improved energy absorption performance leads to better performance in crash tests and is especially of great importance for vehicle's structural members which are

used as passive passenger safety components.

There are different variations of hot stamping process which can be used for producing parts with tailored mechanical properties. Some of these methods are listed below along with their limitations:

1. **Partial heating:** The partial heating strategy involves just heating those regions of blanks above the austenitization temperature where high strength is required. Thus when the final part is formed in the press, complete martensitic structure develops only in those regions whereas in the other regions the microstructure is still similar to the as-received ferritic-pearlitic microstructure. Several strategies have been proposed for achieving such partial heating including using furnace with separated chambers and electrical resistance heating [90, 91]. However most of those methods are not easily transferrable to entire spectrum of hot stamped components and are also significantly expensive [88]. Moreover in the regions which are not heated above austenitization temperature during partial heating, the microstructure remains similar to the as-received condition and does not offer any chance to tailor the mechanical properties in those regions.

2. **Post tempering:** In this method fully martensitic microstructure is obtained by normal hot stamping and then the desired regions with lower strength are

obtained by tempering the martensite through localized heating after hot stamping [92]. Issues with this method include an additional processing step in the production chain, difficulties in isolating the regions of tempered martensite and large amount of time required for tempering until the desired properties are achieved.

3. **Differential cooling by using variable die materials:** This method involves varying the localized cooling rates in the blank during hot stamping by using materials with different thermal conductivity in different regions of tooling [31, 93]. As a result of that, there will be variable heat extraction rates by contact pressure in different regions of the blank when it is formed inside the press. One of the issues with this approach is that once the die has been manufactured, neither the location nor the properties of tailored region can be altered.

Besides these methods, tailored mechanical properties can also be obtained by using tailor welded blanks during hot stamping. Tailor welded blanks are produced by welding boron steel with another steel which has lower hardenability, before the hot stamping process. When such tailor welded blanks are hot stamped, complete martensitic structures are obtained in boron steel whereas the steel with lower hardenability exhibits softer microstructures [94]. The downside is that there is an additional processing step of welding involved, which drives up the cost and

the complexity of the process. Apart from all these methods, there is another method for tailoring of mechanical properties in the final parts produced by hot stamping. This method is highly industry relevant and is based on the idea of using differential heating within tooling for achieving the tailoring of mechanical properties and it is discussed in depth in the following section.

2.6.1 Heated tooling based tailoring of mechanical properties

The basic principle at the core of heated tooling based tailoring is the idea that the cooling behavior of two bodies in contact is most significantly governed by the difference in their respective temperatures. Thus using regions of heated and cooled tooling for forming inside the hot stamping press allows us to control the localized cooling rates inside the parts. By choosing the temperature for heated/cooled region of tooling, the localized cooling rates can be controlled to obtain the desired phase distribution in the final microstructure. And by controlling those localized phase distributions, the mechanical properties can be tailored in the hot stamped parts as desired. This method of tailoring the mechanical properties in the different regions of final hot stamped parts by varying the tooling temperatures in different regions, has also been referred to as tailored tempering in several papers in the literature [63, 88, 95].

Banik et al [96] investigated the resulting mechanical properties in boron steel

when it was quenched and formed using tools heated to different temperatures. It was reported that both strength and ductility of the boron steel can be significantly adjusted as required by simply varying the tool temperatures. Transition zones with widths in range of 15-50mm have been reported in tailor hot stamped parts produced by this method depending on blank thickness and heating & cooling layout in tooling [95]. The work done by George et al [17] also investigated the effect of tool temperatures and other process parameters on the resulting phase distribution and hardness in boron steel and showed how they can be used for tailoring the final mechanical properties.

There are several advantages of heated tooling based tailoring method over the other methods described in the previous section which have led to its widespread acceptance. One of the most important advantages is that there are no special requirements in the heating step as required for partial heating method and so the existing furnace technology and infrastructure can be used without any need for additional investment. Secondly there are no additional processing steps and thus it allows for low production cycle times. This method can be used with both direct and indirect hot stamping process for tailoring of the properties. Finally it allows for the mechanical properties to be tailored in a wide range just by adjusting the localized tooling temperature and is also quite flexible in terms of the size, shape and position of the soft ductile regions.

Thus as a result of all the aforementioned reasons, this method is one of the most popular and promising variant of hot stamping process for obtaining tailored properties in the final parts [88]. Hence this is the method for tailored hot stamping, which was chosen to be the focus of this current project. From now onwards tailored hot stamping in this thesis will always refer to this heated die/tooling based method for tailoring the final mechanical properties in the part, until explicitly mentioned otherwise. All the tailored hot stamping experimental physical simulation work done in this project was based on this particular method.

2.7 Models for phase distribution prediction

The phase transformations which occur in boron steel during forming and quenching inside the press determine the final phase distribution in the microstructure in different regions of the formed part. These localized phase distributions in the different regions of hot stamped parts determine the final mechanical properties of those regions. Thus predicting these phase distributions is a necessary condition for successful prediction of localized mechanical properties in a part after hot stamping.

Extensive experimental and theoretical investigations have been carried out on the phase transformations which occur in steels during cooling. The most commonly used method for predicting austenite decomposition during cooling is based on

utilizing Continuous Cooling curve Transformation (CCT) diagrams of the given steel. CCT diagrams are generated experimentally and their main advantage lies in their ease of use. However CCT diagrams are completely accurate only for the time temperature cycles which were used in the experimental investigations done for their generation. Any discrepancy between actual cooling curve and the curves used during their generation can lead to deviations from the microstructure predicted by CCT diagrams. Thus CCT diagrams are good as a rough qualitative guide but not suiTable for quantifying the exact phase distribution in the final microstructure of steel based on varying processing parameters.

On other hand many semi-empirical physical models based on fundamentals of thermodynamics and kinetics have been developed in order to model the austenite decomposition in steel during cooling and for prediction of the final phase distribution in the microstructure. The first model for kinetics of austenite decomposition based on nucleation and growth theory was proposed by Kolmogorov in late 1930's [97]. The most widely used models for austenite decomposition in steel are based on works of Johnson-Mehl [98] and Avarami [99] and their models are well suited for simulation of diffusion controlled isothermal austenite decomposition. For diffusionless transformation of austenite to martensite in steels, the model proposed by Koistinen-Marburger [100] is widely used in literature. Since then researchers have continued the investigations further in order to develop better models for austenite decomposition in different grades of

steels [101-103]. A detailed description of the main models used for simulation of austenite decomposition is given in the following sections.

2.7.1 – Johnson-Mehl-Avarami model (JMA)

The mathematical model developed by Johnson-Mehl-Avarami (JMA) is applicable only for diffusion controlled isothermal transformations during austenite decomposition. According to the model, the volume fraction X of austenite transformed at a constant temperature T in time t is given by the following equation given below:

$$X = 1- \exp (-kt^n) \quad (2.2)$$

Where k is the rate constant and n is time exponent. The rate constant k is a function of temperature and transformation mechanism, whereas the time exponent n is a constant in the temperature range when a unique transformation mechanism operates [103]. This same equation is used for modelling all diffusion mechanism based phase transformations by adjusting the parameters in the equation corresponding to the particular phase being modelled. The values for the parameters are obtained from the experimental data which is used to generate isothermal time-temperature-transformation (TTT) diagrams.

In order to simulate the austenite decomposition during continuous cooling,

usually the cooling curve is approximated by a series of very small isothermal time steps and then Scheil's additivity rule is applied for calculation of the new phase fraction formed [103]. Accordingly, the non-isothermal transformation kinetics are described as sum of series of small isothermal transformations and each time step produces such a transformation as would have occurred in the isothermal transformation at that temperature.

2.7.2 Kirkaldy and Venugopalan model (K-V Model)

Another quantitative microstructural evolution model developed by Kirkaldy and Venugopalan [104] has also become quite popular for modeling diffusion based phase transformations in austenite decomposition under continuous cooling. This model has been used by many authors to predict the microstructural evolution in HAZ (heat affected zone) during welding operations [105] and also for predicting TTT or CCT diagrams for steels [106]. One of the advantages of this model is that it is well suited for numerical implementation and also this model can be used for wide variety of steels whose total alloy content does not exceed 2-3 wt%. Furthermore using this model does not require any prior knowledge from the time-temperature-transformation diagrams as required by JMA model.

The mathematical framework of the model for diffusion controlled austenite decomposition during continuous cooling for a single phase is as follows:

$$\frac{dX}{dt} = f(G)f(C)f(T)f(X) \quad (2.3)$$

where X is the current volume fraction which has transformed from austenite and f signifies a general functional relationship. Both nucleation and following growth of the daughter phase are assumed to be described by this single equation. In the equation f(G) is the effect of ASTM austenite grain size, f(C) is the effect of steel composition, f(T) is the effect of temperature and f(X) is the effect of austenite phase fraction which has already transformed.

The effect of the ASTM grain size number is described by using the following equation:

$$f(G) = 2^{(G-1)/2} \quad (2.4)$$

where G is the ASTM austenite grain size number. The effect of the alloy composition of the steel f(C) is described by an equation of the following type:

$$f(C) = (aMn + bNi + cCr + dMo+eC+k)^{-1} \quad (2.5)$$

where a, b, c, d, e and k are constants which depend on the phase into which austenite is decomposing (either ferrite or pearlite or bainite). The temperature term f(T) which describes the effect of temperature on the rate of reaction is expressed as:

$$f(T) = (T_{cr}-T)^{n}e^{-Q/RT} \quad (2.6)$$

where T_{cr}-T represents the amount of supercooling for a given phase and depending on the phase T_{cr} is either Ae_3 (for ferrite), Ae_1 (for pearlite) or B_s (for bainite) and T is the current temperature. The exponent depends on the type of reaction and has different value for different phases, while Q is the activation energy for diffusion and R is the universal gas constant. Finally, the term f(X) which gives the effect of current fraction formed X on rate of reaction is given by:

$$f(X) = (X^{2(1-X)/3} * (1-X)^{2X/3})/Y \quad (2.7)$$

where X is the current normalized fraction formed. The factor Y has value 1 for ferrite and pearlite whereas for bainite reaction it is given by:

$$Y = e^{Cr\ X\wedge 2} \quad (2.8)$$

Where Cr is the bainite retardation co-efficient which is alloy dependent. Thus for each individual diffusion controlled phase transformation reaction, we will obtain an individual set of separate differential equations. Solving the equations for each phase in the K-V model at a given temperature and time will yield the amount of that phase fraction formed from austenite, for given steel with a fixed chemical composition. The differential equations described in the K-V model are solved using iterative numerical solution methods.

2.7.3 Koistinen and Marburger model

If any amount of austenite is left untransformed when the temperature falls below

the martensite start temperature and if the cooling rate is sufficiently high, then the remaining austenite will undergo diffusionless transformation to martensite. Since it is a diffusionless transformation, it is time independent and depends only on temperature. The martensite phase fraction below the martensite start temperature can be calculated using the empirical Koistinen-Marburger [100] relationship which is expressed as follows:

$$X_m = X_\gamma \left(1 - e^{-\alpha(Ms-T)}\right) \tag{2.9}$$

where X_m is the volume fraction of martensite formed and X_γ is the available amount of austenite for the reaction which is given by

$$X_\gamma = 1 - X_f - X_p - X_b \tag{2.10}$$

where X_f is ferrite fraction, X_p is the pearlite fraction and X_b is the bainite fraction formed at martensite start temperature. The factor α in the equation is a constant and (Ms-T) gives the amount of supercooling that has occurred below the martensite start temperature Ms.

All the semi-empirical physical models discussed in this section for austenite decomposition in steels have been used for phase distribution prediction in boron steel during computer based simulations of hot stamping process. These models have had limited success in the final phase distribution prediction task during hot stamping and their limitations are discussed in detail in the next section.

2.8 Phase distribution prediction during hot stamping

An accurate prediction of the final resulting phase distribution in different regions of the hot stamped parts is of great importance for successfully tailoring the final mechanical properties of the part as required. These in turn requires fully coupled thermo-mechanical-metallurgical models for making such predictions. Much work has been done for thermal and mechanical simulation of the hot stamping process using numerical modelling and good agreements between predicted and measured values have been reported in the literature [107-109]. Thus at present there is a heavy focus on developing good metallurgical models which can be coupled with the existing well established thermal and mechanical models for accurate phase distribution prediction after the hot stamping process.

In 2006, Akerstrom et al [110] modified the KV model to incorporate the effect of boron hardenability in the steel and coupled it with thermal and mechanical numerical modelling for predicting the final resulting phase distribution in the plane hardened stamped parts. The phase distribution predictions made were in agreement for the part of the blank which was air cooled but deteriorated for the part of the blank which was in full contact with the tooling. The percentage volume fraction of predicted phases were off by as much as 27% even considering that there was no deformation involved. The model's performance would have deteriorated even further in case of deformation because of its inability to take the

effect of deformation on the final phase distribution into consideration. Then in 2012 George et al [17] used the material model proposed by Akerstrom et al in the commercial FE code LS-Dyna to predict the phase distribution in different regions of tailor hot stamped parts. During the validation of their model by comparing its phase fraction predictions against actual values obtained from experiments, significant microstructural discrepancies were observed in the regions of high deformation within the formed parts. The authors explicitly attributed the observed discrepancies between the phases predicted by the model and the phases observed in the microstructure to the fact that the metallurgical model proposed by Akerstrom et al [110] did not account for the effect of deformation during final phase distribution prediction.

In 2007, Behrens et al [111] developed a model which used JMA equation for diffusion controlled transformation and the Koistinen-Marburger equation for diffusionless transformation and that model was implemented using commercial FE code LS-Dyna for simulating microstructural evolution in boron steel during hot stamping. However, this model also did not reflect the effect of deformation while making phase distribution prediction. In 2011, Bok et al [112] compared the performance of the original KV model, Akerstrom model [110] and Li modified KV model [113] for microhardness prediction in a hot stamped B-pillar. Bok et al used the phase fractions predicted by these different models during computer simulation of hot stamping to make the microhardness prediction. All the three

models performed poorly in the regions of high deformation within a B-pillar, with the average difference between predicted and measured microhardness values being 180 Hv (Vickers hardness) in the region with highest deformation. This poor performance was a direct result of the inaccurate phase distribution predictions by each of the three models investigated in this work, none of which took into consideration the effect of deformation on the final phase distribution.

All the models discussed so far have made phase distribution predictions only by taking into account the thermal history of the hot stamped part. As discussed in the earlier section, the amount of deformation has a significant impact on the phase transformations taking place inside the steel and thus directly impacts the final resulting phase distribution after hot stamping. As a direct result of that, all the models mentioned above ended up making poor predictions for the regions of hot stamped parts which have got significant amounts of deformation. This fact was acknowledged in most of the works and the deformation amount was suggested as a factor which needs to be researched for further improving the performance of phase distribution prediction models.

Finally in 2014, Tang et al [114] implemented a numerical model for phase distribution prediction which took into consideration the effect of deformation history while making the final predictions about phase distribution and Vickers hardness using the implicit FE code FORGE^{TM}. In their work, they experimentally

determined the change in the phase transformation kinetics due to applied deformation by measuring the shift in the TTT curves of 22MnB5 boron steel in response to applied stress. They used this modified TTT curves along with the JMA equation to predict the fractions of ferrite, bainite & pearlite, while they used the Koistinen-Marburger equation to predict the fraction of martensite in the final microstructure. They coupled this model with thermal and mechanical modelling and applied it to tailored hot stamping process for evaluating the model's performance. A two section die was used with one section of die heated to 450°C, while the other section of die still being at room temperature for the model validation. Taking into account the effect of deformation along with thermal history for phase distribution prediction, that led to good agreement with the observed microstructures for the cooled sections. However for the heated sections of the die, the model predictions still did not show good agreement with the observed microstructure for the regions with high deformation. Thus for heated dies, the model was still not able to completely capture the effect of deformation on the final phase distribution even though it did give better performance as compared to earlier models by taking into account the effect of deformation. In their work, the authors have not specified any reason for the poor performance of the model in the high deformation region under heated section of the die. They have just pointed to the limitation of the model and suggested that there is further room for improvement in model performance. A possible reason for it could be the complicated thermal path followed by the region under heated die. Following such

complicated thermal paths leads to very complex interactions between the thermal path and amount of deformation parameter and such complex interactions might not be captured completely by simple measurement of the shift in TTT diagrams. Thus there is a definite scope and need for improving the phase distribution prediction capabilities during tailored hot stamping process simulations.

An improved and more accurate phase distribution prediction model would greatly help in further optimizing the process parameters to better tailor the final mechanical properties in the tailor hot stamped parts. Such a model would directly lead to better designed automotive structural components, which would result in improved crash performances and lower weight for the cars. Thus this challenge of developing an accurate and robust phase distribution prediction model for tailored hot stamping process is an important industrial challenge with significant real life implications and thus was chosen to be addressed in this research.

2.9 Artificial Neural Networks in materials science

Besides the semi-empirical physical models discussed in the previous section for phase distribution predictions in steels, another approach based on Artificial Neural Networks (ANN) has been explored in the last decade in the field of material processing [115, 116, 122, 124]. Very promising results have been obtained from the models developed using ANN not only for phase distribution

prediction but also for other classes of problems in the field of materials processing and manufacturing [118, 119]. This approach is particularly suiTable for developing models for prediction in cases where the qualitative effects of all the relevant input parameters on the output are known but those effects have not yet been quantified by the existing models. The knowledge of qualitative effects of input parameters on output is an empirically observed proof of the existence of a functional relationship and ANN based models can be used to learn that functional relationship from experimental data. Once the ANN based model has successfully learnt those functional relationships from experimental data, then the ANN based model can be used for guiding engineering decisions.

The power of ANN based modelling lies in its capability to learn any kind of functional relationship present in the experimental data and not be limited to a particular class or set of functional relationships. This capability of ANN based models makes it a powerful tool for modeling materials processing, where from a fundamental theoretical perspective the complexity of developing such a model can be overwhelming and yet a quantification is required for engineering application. The basic mathematical principle behind an ANN model corresponds to learning from experience (past observations, data) and using the knowledge gained from that to make future predictions. A further in depth technical and mathematical background of ANN based modeling is given in the section 5.1 and section 5.2 of the Chapter 5 (ANN Model Development) of this thesis and the

reader is requested to refer to it for a better understanding of the fundamentals of ANN based modelling.

In the past decade, ANN based models have been successfully developed in material science for problems ranging from predicting phase distributions in hot rolled steels to making failure predictions in carbon fiber reinforced polymer composites [117, 118, 120-122]. Kusiak et al [122] used an ANN based model to predict the final microstructure phase fractions as well as ferrite grain size during the thermomechanical processing of C-Mn microalloyed steel and compared its performance with other existing classical and empirical models. The ANN based model was trained using data obtained from laboratory based physical simulation of the manufacturing process and it was able to successfully generalize to the actual industrial process. In their work, they concluded that: "the well-trained neural network model under laboratory conditions is able to predict the correct values of the output parameters of the industrial process" [122]. Similarly Khalaj et al [123] and Bhattacharya et al [124] have also reported excellent performance of neural network based models when applied to Vickers microhardness and microstructure prediction respectively during thermomechanical processing of steels. Thus artificial neural network (ANN) based models have previously shown promising results for phase distribution and final property prediction problems in steels after their thermomechanical processing and they offer great potential for addressing this complex scientific and industrial scientific challenge of phase

distribution prediction after tailored hot stamping process.

2.10 Instrumented Nanoindentation:

Now the microstructure produced in the boron steel after tailored hot stamping process is a complex mixture of martensite, bainite and ferrite phases. The relative distribution of these phases in various locations along a part depends on the thermal and the mechanical history of each localized region. One of the major challenges involved in developing a dependable and robust ANN model is to accurately and reliably quantify the final phase distribution present in a given localized region. Metallography is useful for the qualitative assessment of the microstructures but not suiTable for reliable phase distribution quantification of complex microstructures obtained in boron steel after hot stamping. The exact interpretation of microstructural images is subjective and hence the phase distribution quantification obtained through metallography does not have the necessary reliability or repeatability as required for ANN model development. It is common knowledge that each of the microstructural phases in steels has got different hardness characteristics [128]. This difference in the hardness levels of individual phases can be used to characterize and quantify their relative distribution in the final microstructure with a high degree of reliability using the state of the art cutting edge instrumented nanoindentation technique [129].

Usually measuring the hardness values for each individual phase in the boron steel microstructures after tailored hot stamping using conventional microhardness tests is difficult because of the small sizes involved for each individual phases. Conventional microhardness tests end up giving average hardness values of an entire region by taking an indent which is spread over multiple phases rather than giving the hardness values of each individual phase. That is where nanoindentation offers the potential to measure the hardness value for individual phases by making indents which are at maximum of the order of few microns. Because of the low loads and low depths involved, the scale of the size of the indent produced by nanoindentation is of a similar or a smaller order than the size of individual phases present in the microstructure. This allows us to measure the hardness value of each phase individually, rather than measuring the average hardness value of multiple phases. Application of cutting edge instrumented nanoindentation technique for phase quantification in steels is a very recently development, with its first use for boron steel phase quantification happening only in 2008 [129].

Since instrumented nanoindentation is such a new experimental technique, in the following sections a general technical background for the nanoindentation technique is presented before discussing the experimental details of scanned surface instrumented nanoindentation experiments done for phase quantification in the Gleeble test samples in the next chapter.

2.10.1 Types of indenters

There are different kinds of indenters which are used for conventional hardness testing. Standard indenters include spherical indenter, conical indenter, Vickers indenter and Berkhovich indenter [131]. There are also other indenters which are used for specialized testing when the standard geometry indenters are not able to fulfil the requirements. Figure 2.4 below gives the geometrical schematic for each of the standard indenter type along with their indentation parameters.

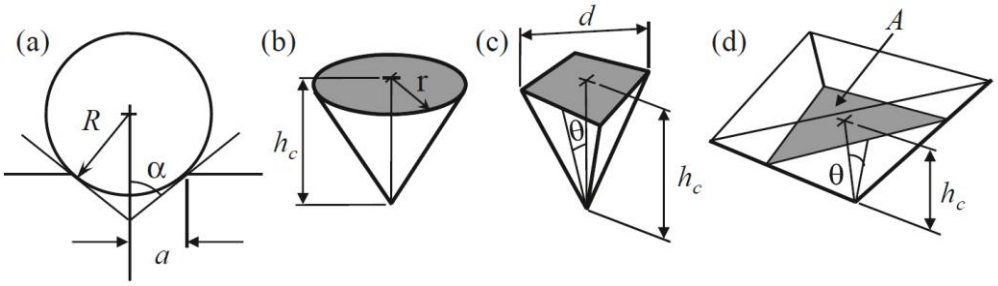

Figure 2.4: Different types of indenters: (a) Spherical Indenter (b) Conical Indenter (c) Vickers Indenter (d) Berkhovich Indenter [from 131]

The Berkhovich indenter is the most widely used indenter in instrumented nanoindentation testing as it has got several advantages over the other indenters [131]. Berkhovich indenter is not easily damaged, it can be easily manufactured and it induces plasticity at very low loads to give a meaningful measure of the hardness of material. Compared to four sided Vickers indenter, the three edges of the Berkhovich indenter can be easily constructed to meet at a single point and

give a sharper tip [131]. Spherical and conical indenters have been used very little for instrumented nanoindentation testing because of the difficulty involved in their manufacturability at such small scales. Diamond is the most commonly used material for nanoindenter tips because of its properties of hardness, thermal conductivity and chemical inertness. Besides diamond other hard materials like sapphire, quartz, tungsten carbide and any other hard metal or ceramic material can be used for manufacturing of the nanoindenter. Usually the tip radius for new Berkhovich indenter is <20nm and it increases to about 200nm with use [131].

2.10.2 Vickers hardness scale

Though Berkhovich indenter is the most widely used indenter for instrumented nanoindentation testing, the hardness value obtained by it is commonly reported in the Vickers hardness scale (HV) [5, 52, 129]. The reason for doing so is the historical widespread use of Vickers scale in the hardness testing. There is large amount of hardness data for different materials available in literature in Vickers scale and so reporting in Vickers scale allows for easy comparison with the available data. For Vickers test four sided pyramidal indenter the opposite faces are at an angle of 136° and thus the face semi-angle θ is 68°. The Vickers scale hardness value (HV) is calculated after the indentation by dividing the indentation load with actual contact surface area of the impression. The equation for calculating the Vickers hardness for a Vickers indenter is given by [131]:

$$HV = \left(\frac{2F}{d^2}\right) \sin\left(\frac{136^\circ}{2}\right) = 1.8544 \left(\frac{F}{d^2}\right) \quad (2.11)$$

where F is the indentation load and d is the length of the diagonal of residual impression. Traditionally the Vickers scale has units of kgf/mm^2 and thus for obtaining the hardness value in Vickers scale using the above equation, the value of F should be in kgf and diagonal d in mm.

Another scale for reporting hardness measurements in nanoindentation is the mean contact pressure hardness value (H), also known as Meyer hardness. For Vickers indenter is calculated using the projected area instead of actual contact area [131]. For Vickers indenter, with F being the indentation load and d being the length of the diagonal of residual impression, it is given by the following equation:

$$H = 2 \left(\frac{F}{d^2}\right) \quad (2.12)$$

Since Meyer hardness value is the mean contact pressure, it is usually reported in the units of N/m^2 = MPa and thus in the above equation the value of F should be in N and diagonal d in m. After doing the units conversion from MPa to kgf/mm^2, we get the following equation relating Vickers hardness (HV) to Meyer hardness (H) for the Vickers indenter:

$$HV = 0.0945\ H \quad (2.13)$$

with H having units of MPa and HV having units of kgf/mm^2.

2.10.3 Berkhovich indenter

The Berkhovich indenter is a three sided pyramidal indenter invented by E. S. Berkhovich in 1950 for studying microhardness by indentation. Initially the Berkhovich indenter was designed with a face semi-angle of 65.03° which gave the same contact surface area to depth ratio as a Vickers indenter based on its geometry. But since it is customary to use the mean contact pressure value for measuring hardness (H) in nanoindentation, it is the projected area which is more important than the actual contact area. Thus the Berkhovich indenters used for nanoindentation have a face semi-angle of 65.27°, which gives the same projected area to depth ratio as a Vickers indenter [131]. Since the hardness value obtained from the nanoindentation is the mean contact pressure hardness value (Meyer hardness), equation 3.5.2.3 can be used to directly convert that hardness value obtained using Berkhovich nanoindenter to Vickers hardness scale value.

2.10.4 Load displacement curve

In nanoindentation testing because of the very small size of the residual impression left on the material after indentation, it is extremely difficult to obtain accurate measurements of the indent size using optical techniques such as those used for conventional hardness tests. Thus in nanoindentation testing the depth of penetration into the specimen surface is recorded while applying load and that is

used along with the knowledge of the geometry of the indenter to calculate the size of contact area. The data obtained from nanoindentation tests is used to plot a graph from experimental readings of indenter load and depth of penetration. A schematic diagram of a typical load displacement curved obtained by a Berkhovich indenter is given in the Figure 2.5 where P is the indenter load and displacement h is the depth of penetration.

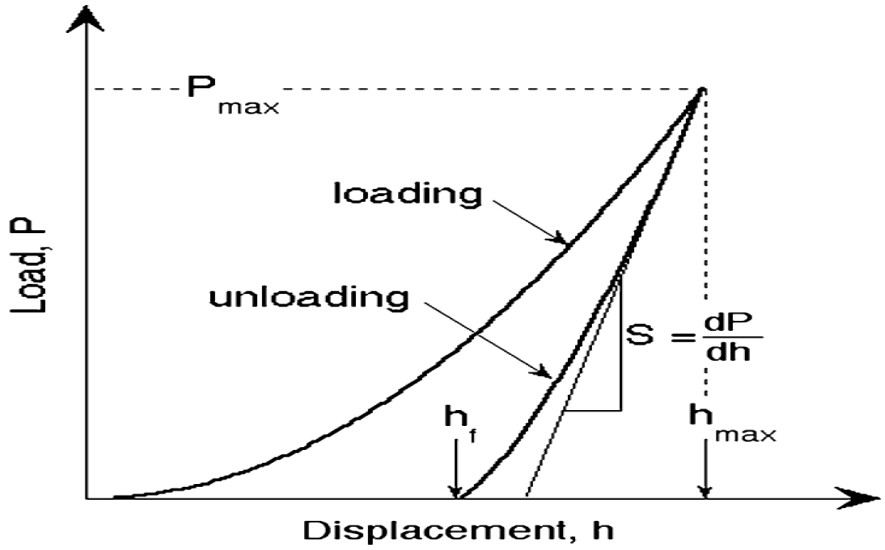

Figure 2.5: Schematic diagram of typical load displacement curve [from 131]

The three most important quantities to be recorded from load displacement curve includes the maximum load P_{max}, the maximum displacement h_{max} and the contact stiffness S which is basically the slope of the initial portion of the unloading curve. Using these quantities the hardness value and the elastic modulus value of the material can be calculated. If the maximum load on the indenter leads to plastic

deformation, then a residual impression is left on the surface. But because of the extremely low loads used in nanoindentation, the size of the indent is really small and hence it is not possible to accurately measure its size with conventional optical methods. The depth of penetration along with the knowledge of the geometry of the indenter allows us to indirectly calculate the projected area at full load and that in turn allows the mean contact pressure hardness value for the nanoindentation test to be calculated [131]. This hardness value measures the resistance of the material to combined elastic and plastic deformation at full load. The data obtained from instrumented nanoindentation testing can also be used to quantify the elastic modulus and other relevant mechanical properties besides hardness [130].

In the instrumented nanoindentation testing method, a large two dimensional array of nanoindents is taken on the surface and then the data obtained is analyzed to calculate the volume fractions of independent phases. This method of two dimensional nanoindentation mapping of the surface is especially relevant for microstructures where locating individual phases through normal optical microscopy is difficult as it completely eliminates the cumbersome task of finding the right phase and moving the indenter over to that phase. Also taking single point indents just allows us to characterize the phases present but does not give us any idea about the volume fraction of the phases present. Thus nanoindentation testing allows for extraction of the localized hardness values for each individual phase present and scanning the entire surface leads to quantification of volume

fraction of different phases present in the microstructure.

2.11 Summary

Tailored hot stamping is a complex process both from a manufacturing and metallurgical perspective. However, it is also the manufacturing process which offers the greatest potential to improve the crashworthiness of the car, while at the same time helping in reducing its overall weight. A major impediment to tailored hot stamping process achieving its full potential is a lack of a reliable phase distribution prediction model for the parts produced by this process. A lack of such reliable phase distribution prediction model means that the engineers cannot design the best possible tailored component guided by intelligent CAE and thus cannot utilize the process in most efficient manner to achieve desired outcomes.

The main reason for the lack of such a reliable phase distribution model is the complexity of phase transformations which occur inside the boron steel during its processing by tailored hot stamping process. The phase transformations during tailored hot stamping are directly influenced by both the thermal and mechanical history of the part during the manufacturing process. At the same time, both thermal and mechanical histories of the part also interact with one another and affects the final phase distribution. Also each of the individual phase transformations, which occur during cooling of hot pre-deformed austenite inside

the part during the process, are not independent of one another. The amount of austenite available for being converted into daughter phases during cooling in hot stamping is fixed and thus increase in the volume fraction of one phase will directly result in the decrease of other phases. Furthermore the mechanism and kinetics of each phase already formed in the microstructure also end up directly influencing the phase transformations that are going to follow.

2.11.1 Significance and Novelty of work

As a result of all these complexities, most of the existing models for phase distribution prediction in boron steel are as of yet unable to predict with a high degree of accuracy the final phase distribution after tailored hot stamping. Most of the metallurgical models developed so far for the phase distribution prediction in hot stamping process do not take into account the effect of deformation and that is one of the main reasons for their limited performance [17, 110-112]. Finally, the model developed by Tang et al. [114] which tried to account for the effect of deformation by measuring the shift in the TTT diagrams of the boron steel due to applied stress, it did not perform well in the high deformation regions under heated tooling. Thus for tailored hot stamping, all attempts so far at predicting the final phase distribution using the standard physical models for austenite decomposition in steels have had limited success.

Thus there is a pressing need for making accurate phase distribution predictions during tailored hot stamping, so that the process parameters can be optimized to achieve the desired mechanical property distribution in the final hot stamped parts. The ability of ANN based model to learn any complex mathematical functional relationships present in experimental data and its ability to use the learnt knowledge for making new accurate predictions makes it well suited for addressing this complex industrial problem of phase distribution prediction in boron steel during tailored hot stamping. Also the past excellent performance of ANN based models for other materials processing problems reported in the literature, supports its case for being a promising approach for solving this problem.

Based on its technical potential, the ANN based modeling method should be capable of taking into account both the thermal history and deformation history while making the final phase distribution predictions during tailored hot stamping. And by being able to account for the effect of deformation while making final predictions during tailored hot stamping, ANN based modelling should offer a distinctive advantage over most of the existing models. To the best of this author's knowledge no such Artificial Neural Network (ANN) based phase distribution prediction model has ever been developed before for processing of ultra high strength boron steel during tailored hot stamping process. Thus the effectiveness and suitability of the ANN based model in making reliable phase distribution

predictions during tailored hot stamping process needs to be researched and that therefore will be the central focus of this thesis.

2.11.2 Technical Roadmap for the research

Developing an ANN based phase distribution model for tailored hot stamping process is likely to be a highly challenging task given all the complexities involved in tailored hot stamping process, both from a manufacturing and metallurgical perspective. For developing the model, physical simulation will be needed to be carried out for this complex industrial process in order to build the dataset required for training the ANN model. Out of all the process parameters discussed, the process parameters which have the greatest influence on the final phase distribution from a process control perspective and which will be the main focus of the present research are: (1) Cooling rate parameter, (2) Deformation amount parameter and (3) Temperature of deformation parameter. The other process parameters discussed have relatively much smaller effect on the final phase distribution and decreasing marginal utility in their capability for influencing that final phase distribution. Because of the constraints on available experimental resources, these other minor factors were not investigated during thermo-mechanical physical simulation experiments and the limited available experimental resources were concentrated on fully capturing the impact of those aforementioned three main process parameters on the final phase distribution.

Another key requirement for developing a good ANN based model will be to accurately measure the resulting volume fractions of different phases in the microstructure of boron steel after tailored hot stamping process. This measured volume fraction of different phases in the final microstructure will form the output part of the training dataset and thus they need to be both accurate and reliable. Once the training dataset is developed, the ANN based model will be developed using an implementation of the backpropagation algorithm. It will be made to learn the functional relationships between the input thermal & mechanical history and the final resulting phase distribution from the available knowledge of those relationships present in the training dataset. Finally once the ANN model has been developed it will need to be validated by measuring its performance against new independent experimental data to establish its robustness and reliability. Also the uncertainty in model's final predictions will need to be thoroughly quantified before it becomes suiTable for engineering application.

In the next chapter, the Gleeble experimental work done for thermos-mechanical physical simulation of the tailored hot stamping process is documented in detail. The next chapter also details the use of instrumented nanoindentation technique for accurate phase distribution quantification in the final Gleeble test samples. The use of optical microscopy and metallography for secondary qualitative microstructural analysis of the test samples is also presented in the next chapter.

Chapter 3

Experimental Details

3.1 Overview

The experimental work done in this research was carried out in three distinct phases with the primary aim of developing an experimental dataset, which was needed for development and validation of the ANN based model. In the first phase, preliminary hot stamping experiments were carried out in an industrial scale modified extrusion press which had been repurposed to make it suiTable for hot stamping experiments. The main reason behind doing these preliminary hot stamping experiments was to study and measure the exact thermal conditions that a formed part undergoes during commercial hot stamping operations, so that the data obtained could be used for designing the next phase of experimental work.

During the second phase, in the absence of an instrumented hot forming press capable of doing tailored hot stamping, Gleeble thermomechanical simulator was used to carry out laboratory scale physical simulations of the tailored hot stamping process. For a good laboratory scale physical simulation, it is imperative that the thermomechanical conditions which the samples undergo during Gleeble tests are

as close as possible to the actual process. In order to ensure that, the measured thermal history data obtained from the preliminary hot stamping experiments was used along with the relevant data available from literature to design the final Gleeble tests carried out in the second phase of the experimental work.

Finally in the third phase, the resulting phase distributions in the microstructures of the Gleeble test samples were quantified using instrumented nanoindentation based surface scanning technique and metallography. The nanoindentation based surface scanning method helped with accurate and reliable numerical quantification of the relative amount of phases present in the microstructure, whereas metallography and optical microscopy helped with a secondary qualitative assessment of the final microstructures.

3.2 Phase one: Preliminary hot stamping experiments

Three successful hot stamping experiments were carried out in the modified hot stamping facility located in the WMG workshop, University of Warwick. The material used for the hot stamping experiments was the galvannealed Zn coated 22MnB5 boron steel sheets. The dimensions of the boron steel sheets used for hot stamping were 200mm (length) x 100mm (width) x 1.5mm (thickness). Since the transferring of steel sheets from furnace to the forming press was done manually, the transfer times involved were different during each of the three experiments

3.2.1 Hot stamping Press

The hot stamping experiments were done using the 500 tonne Enfeco Press located in the WMG workshop, University of Warwick. This 500 tonne press had been in regular use as an extrusion facility and had been modified by a series of commissioned works to convert it into a hot stamping facility [125]. Given below in Figure 3.1 is the image of the modified press used for experiments:

Figure 3.1: Modified 500 tonne Enfeco Press in the WMG Workshop area with which was used for hot Stamping experiments

Mechanical modifications were done to the press to allow for the mounting of the forming tools and further electrical modifications were done to support the change from extrusion to forming. Dedicated control system modifications were made to

create a new forming control screen and additional work was done so that it could carry out forming at press speeds similar to those followed in the industry.

3.2.2 Furnace and the tooling system

The boron steel blanks were pre-heated before forming using a Nabertherm N641 furnace with Eurotherm controller. The internal dimensions of the furnace used were 1000 x 1300 x 500 mm^3 and the furnace was capable of a maximum operating temperature of 1200 °C which is well within the required temperature range for processing of boron steel. The access to the furnace was through a counterbalanced manual "up-and-over" door and special protection gear was required to be worn while accessing the furnace

The geometry of the tool that was used was top hat and so finally top hat structures were produced from steel sheet after hot stamping process. Cooling channels were available in the tooling system but were not used during the experiments. The quenching during the hot forming was obtained through full metallic contact between the blank, die and punch. Hot work tool faces were made using the 2344 Cr-Mo alloyed hot working steel which can withstand the high temperatures and thermal stresses that the tooling encountered during hot stamping process. The tooling system had been designed to be used with 1.5mm thickness blanks. Spring loaded blank holders were included in design and were used during

the hot stamping process. Given below is the image of the tooling system used in the press for the hot stamping process along with its dimensional parameters:

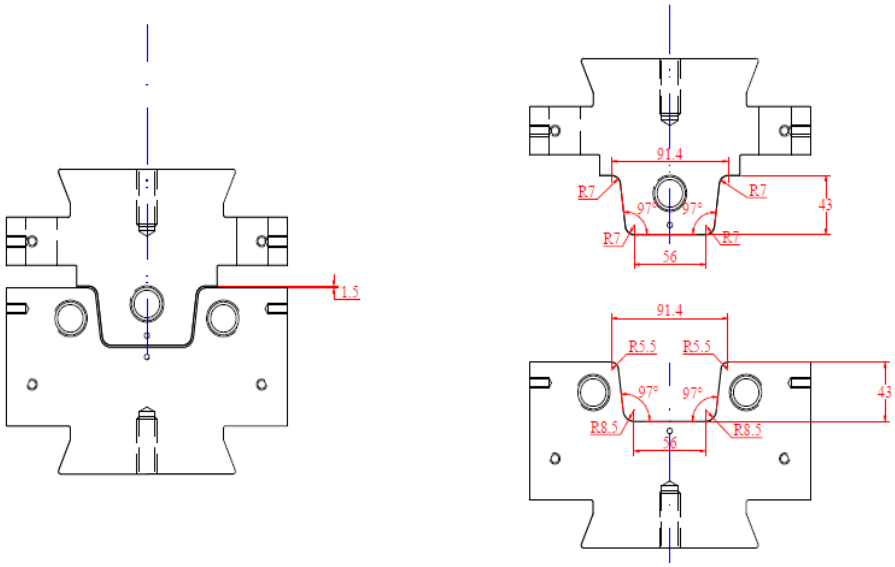

Figure 3.2: Top hat tooling system used in the press for hot stamping experiments

3.2.3 Experimental details

The steel blanks were austenitized at temperature of 910°C in the furnace for a minimum of 5 minutes in order to obtain a completely austenitic microstructure. After the blanks were austenitized they were manually transferred from the furnace to the hot forming press where they were formed and quenched simultaneously. Since the transfer was done manually there were some variations in the transfer time during each experiment and this led to variation in the final deformation temperature of the blanks. Furthermore after transferring the blank to

the press, the forming could not take place until the safety door of the press was closed and so the deformation temperatures were lower than the usual deformation temperatures in the industry. In order to understand the conditions which the blanks undergo during hot stamping, the entire thermal history of the blank was recorded using type K thermocouples welded to the centre of each of the steel blank using micro-welding machine.

3.2.4 Thermal history data from the hot stamping experiments

During hot stamping the most important phase transformations take place during cooling when the blank is removed from the furnace after the austenitization process. Thus the temperature history of the blanks once they are taken out of the furnace is required for designing the Gleeble tests. In the Figure 3.3, the temperature history data for all the three blanks after they were taken out of the furnace during the hot stamping experiments is shown.

As can be seen from the Figure the rate of air cooling between 900-800°C is approximately about 18-20°C/s. Then during the 800-700°C range the rate of air cooling drops to about 12-15°C/s. Finally in the temperature range of 700-650°C the air cooling rate falls down to about 9-10°C/s. After that when the forming happens inside the press, the cooling rate suddenly jumps up to almost 130-150°C/s because of quenching in press cooling due to the full metallic contact

between the room temperature tooling and the high temperature blank. The data obtained from these hot stamping experiments in the industrial scale press helped in designing the thermal routes to be followed by the samples during laboratory scale physical simulation of the tailored hot stamping process using Gleeble thermomechanical simulator.

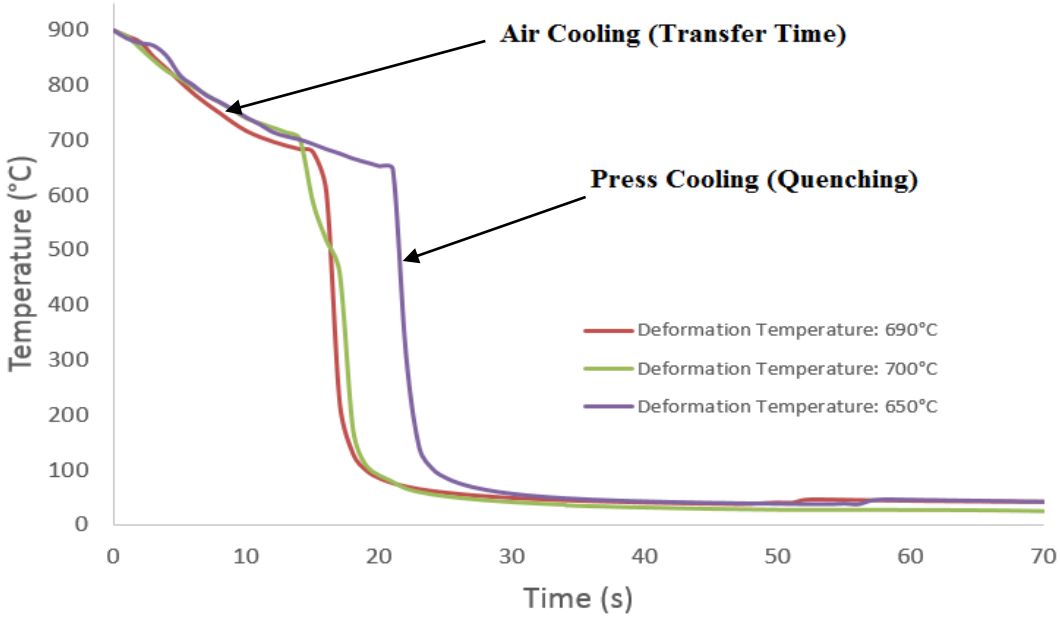

Figure 3.3: Thermal history of the three blanks recorded using K-type thermocouples during preliminary hot stamping experiments

3.3 Phase two: Gleeble experiments

The main focus of this PhD research was to develop an ANN based model for predicting final phase distribution during tailored hot stamping process. For developing such a model, the experimental thermal and mechanical history data

from tailored hot stamping process is required. However as the forming press available in the WMG workshop at University of Warwick did not have any heated hot stamping tooling, it was not possible to do any tailored hot stamping on it. Thus in order to obtain the relevant data required for development and validation of the final ANN based model, physical simulations of the thermomechanical conditions that a part undergoes during tailored hot stamping process were done using the Gleeble 3500 at University of Birmingham. Gleeble is a fully integrated digital closed loop thermal-mechanical testing system, which allows you to do laboratory scale physical simulation of the thermomechanical conditions experienced by a material during the manufacturing processes [126]. A representative image of the Gleeble system used for the experimental work to develop the ANN dataset is shown in the Figure 3.4 given below.

Figure 3.4: Gleeble 3500 Thermal-Mechanical system [from 126]

The main process parameters for tailored hot stamping that were investigated during the Gleeble testing included varying thermal histories (corresponding to different die-temperatures in tailored hot stamping), deformation temperatures and deformation amounts. These process parameters are of primary importance in determining the final relative distribution of different phases in the part after processing as discussed in section 2.4 of the literature review. These are the most influential process parameters which are amenable to optimization for obtaining the desired mechanical property distribution in the final tailor hot stamped part.

3.3.1 Gleeble experimental details

The material used for the Gleeble experiments was HQ1500 CR (commercial name) hot forming steel sheet with a thickness of 1.5mm. It is commercial grade uncoated ultra high strength boron steel developed by Tata Steel especially for hot stamping. The chemical composition of steel is presented in the Table given below:

Table 3.1: Avg. chemical composition of steel used for Gleeble tests in wt %

C	Mn	Cr	Si	Ti	N	B	Ca
0.22	**1.228**	**0.288**	**0.165**	**0.023**	**0.0051**	**0.0032**	**0.0016**

A total of 50 Gleeble tests were performed for physically simulating at laboratory scale the various thermal and mechanical conditions which occur in different

regions of a formed part during industrial tailored hot stamping. The samples for Gleeble testing were cut from the boron steel sheet with two different dimensions but similar geometry as shown in Figure 3.5. This particular dog bone shaped geometry, with holes at the end of the central region, was used because it helped in reducing the temperature gradient caused by electrical resistance heating in Gleeble. The localized temperature history of each sample during the entire Gleeble test was recorded by a thermocouple welded to the centre of the sample. The temperature measured by thermocouple was also fed back to Gleeble machine, so as to complete the digital feedback loop which allowed Gleeble to accurately control the thermal paths followed by the samples.

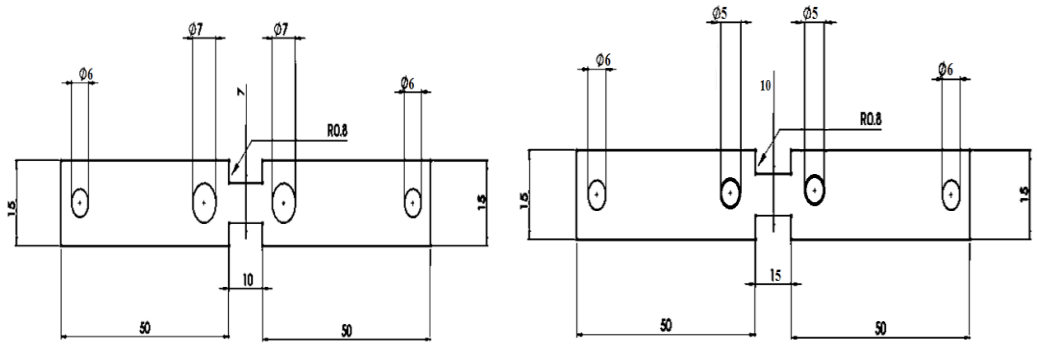

(a) (b)

Figure 3.5: Gleeble test samples with fixed geometry but two different dimensions: (a) Dimension 1 and (b) Dimension 2 (all units in mm)

Gleeble samples with two different dimensions but the same geometry were used to study if higher cooling rates could be achieved during the Gleeble testing by altering the dimensions while keeping the geometry constant. In the Gleeble

machine, cooling is done by pressurized air nozzle spraying air over the sample and hence the hypothesis was that reducing the volume of the central region would help in reducing the thermal mass to be cooled which in turn would lead to higher cooling rates being achieved. No significant differences were observed in the cooling rates achieved in the samples with different dimensions. Using samples with different dimensions did not affect the data being collected for the ANN model, as both the thermal and mechanical history data was collected from the localized region where thermocouples were welded onto the test samples. Hypothetically if the changes in dimensions would have affected the thermal and mechanical history of the samples during Gleeble testing in any way, those changes would have been recorded during localized data collection. Since the ANN model is only concerned with the functional relationship between thermomechanical history and the final resulting phase distribution, as long as the localized data is measured accurately the geometrical dimensions of the sample have got no bearing on the final ANN model.

During the Gleeble tests, all the samples were heated up to temperatures above 900°C from the room temperature at an average heating rate of about 10°C/s. The samples were kept above 900°C for a minimum of 5 minutes to simulate furnace heating during tailored hot stamping. This ensured that all the Gleeble test samples had a fully austenitic microstructure without any significant grain coarsening before the cooling simulation begun. The representative austenitization curve

followed by one of Gleeble test samples is presented in Figure 3.6 for reference.

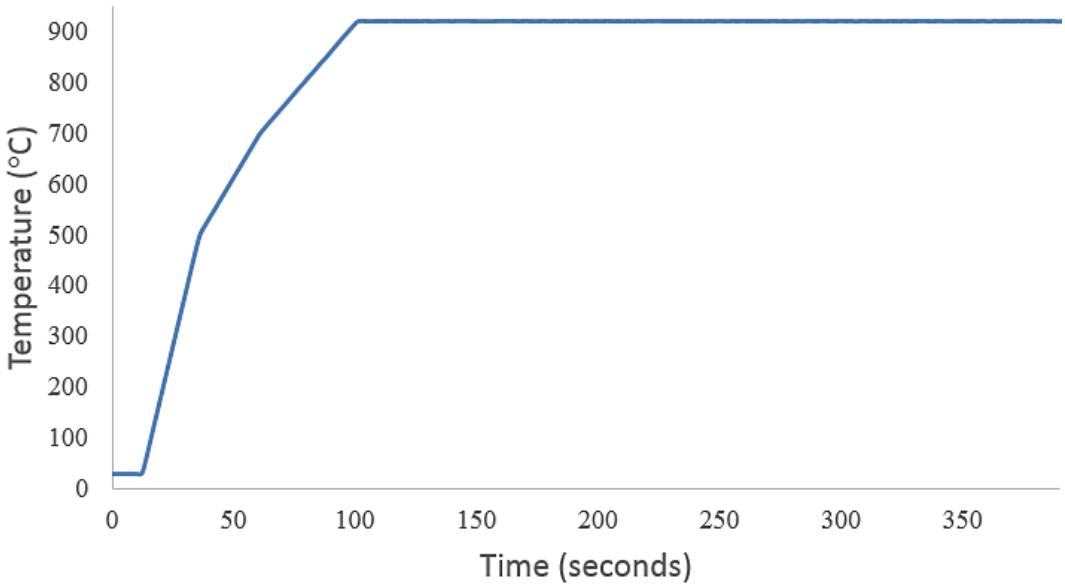

Figure 3.6: The austenitization curved followed by a Gleeble sample

The different thermal paths to be followed by the Gleeble samples after austenitization period were designed using the thermal history data available from preliminary hot stamping experiments in phase one (Figure 3.3) and the tailored hot stamping thermal history data available from literature [17, 114]. The main objective for designing these thermal paths was to physically simulate the tailored hot stamping thermal conditions as closely as possible. All the different thermal paths followed by the samples during the Gleeble tests are presented in Figure 3.7. For each sample initially after austenitization, until the deformation temperature is reached, the thermal paths simulated the air cooling which occurs while a blank is

being transferred from furnace to press. Then at the preset temperature of deformation, different samples underwent varying amount of isothermal tensile deformations. The final engineering strain values in range of 0 to 0.6 were recorded for different Gleeble samples in the localized region of thermocouple welding. The exact process followed for measuring these localized strain values (deformation amount) in the Gleeble test samples is described in section 4.3 of the next chapter. These tensile deformations were done to simulate the different strain values that occur in different regions of tailor hot stamped parts during forming. All the tensile deformations were done a fixed strain rate value of $1s^{-1}$ and this representative strain rate value was chosen based on discussion with the industrial sponsor regarding relevant strain rates for hot forming [G. Hensen, Principal Researcher, R&D TATA Steel Europe, personal communication, July 07, 2014].

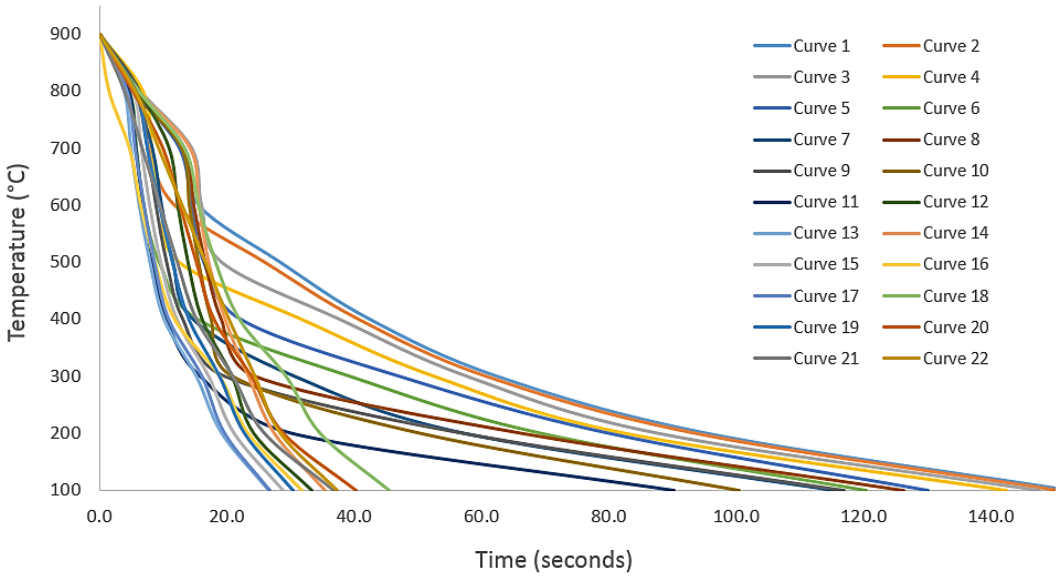

Fig. 3.7: Different thermal paths followed by Gleeble samples after austenitization

Table 3.2: Die temperature & deformation temperatures for thermal history curves

Name	Die Temperature (°C)	Deformation Temperature (°C)
Curve 1	550	700
Curve 2	550	800
Curve 3	450	700
Curve 4	450	800
Curve 5	400	720
Curve 6	400	830
Curve 7	350	770
Curve 8	300	700
Curve 9	300	800
Curve 10	250	730
Curve 11	250	840
Curve 12	200	750
Curve 13	200	850
Curve 14	Room Temperature	700
Curve 15	Room Temperature	800
Curve 16	Cooling rate 80°C/s	760
Curve 17	Cooling rate 80°C/s	840
Curve 18	Cooling rate 55°C/s	705
Curve 19	Cooling rate 55°C/s	815
Curve 20	Cooling rate 40°C/s	780
Curve 21	Cooling rate 40°C/s	860
Curve 22	Cooling rate 20°C/s	860

After the deformation is over, different Gleeble samples followed varying thermal paths as shown in Figure 3.7. Each thermal history curve shown in Figure 3.7 from curve 1 to curve 15 corresponds to different die temperature and different deformation temperature with a quench duration of 10 seconds for tailored hot stamping process. The thermal history curves from curve 16 to curve 22 in Figure 3.7 correspond to different constant cooling rates followed by the samples after deformation. These constant cooling rate curves try to simulate the different thermal history conditions which might occur in different regions of the formed part in conventional hot stamping process. For each thermal path in Figure 3.7, the corresponding details are given in Table 3.2.

Thus, together all the different thermal paths shown in Figure 3.7 correspond to various thermal conditions which are experienced in different regions of a final formed part after tailored and conventional hot stamping process. All possible efforts were made, within the constraints of available experimental resources, to physically simulate the thermal and mechanical conditions of the industrial tailored hot stamping process as closely as possible during the Gleeble testing.

3.4 Phase three (part I): Gleeble sample metallography

Following the Gleeble testing, each sample was cut at the point of the thermo-couple welding using a Buehler IsoMet 4000 linear precision saw. The cross-sectional area of the sample was used for metallographic analysis as that was the

location from where thermal history data had been collected using the thermocouple. All the samples were mounted in thermosetting resin using the Buehler SimpliMet hot mounting press, ground using abrasive paper and then finally polished to a mirror finish using a final stage 0.05 micron diamond suspension polishing liquid.

After that all the steel samples were etched using standard 2% Nital solution; a chemical etchant consisting of 2% nitric acid and 98% methanol [127]. Etching is a process which makes it possible to study the microstructure under optical microscopy by selectively corroding the different features of the microstructure based on their potentials. It is a controlled corrosion process and is based on the idea of differential electrolytic action occurring at structural variations in the microstructure caused by either physical or chemical heterogeneities. The differential electrolytic action leads to different features being rendered either anodic or cathodic depending on the etching conditions and leads to variation in the corrosion response of the features. This differential corrosion leads to metallographic contrast amongst different features under the microscope and makes it possible to observe those features. The 2% Nital solution is the most commonly used etchant for steels [127]. It helps in revealing ferritic and martensitic microstructure under optical microscopy by selectively attacking the grain boundaries in steel but is unable to distinguish between bainite and martensite with high reliability.

The etched Gleeble test samples were observed at 50x magnification under an optical microscope and for each sample multiple microstructural images were recorded at different locations along the cross-sectional surface. These microstructural images obtain through conventional metallography were mainly used for secondary qualitative assessment of the different phases present in the final microstructure in order to determine the accuracy of the phase distribution quantification done by state-of-art instrumented nanoindentation technique discussed in the next section. Two representative microstructural images obtained from the same Gleeble test sample taken from two different locations along the cross sectional surface are presented in Figure 3.8 given below. Both the microstructures can be seen to have a heavy martensitic content, which is in agreement with the measured martensite phase volume fraction of 94.4% obtained from instrumented nanoindentation technique for this Gleeble test sample.

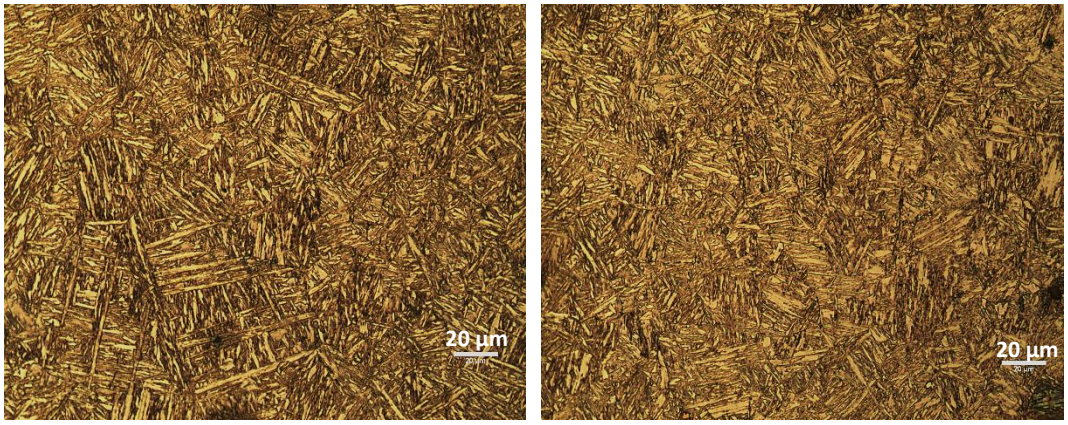

Figure 3.8: Two microstructural images obtained from two different locations on the cross-sectional surface of a Gleeble test sample

3.5 Phase three (Part II): Instrumented nanoindentation

The instrumented nanoindentation testing was carried out on the Micromaterials NanoTest Nanoindenter at University of Birmingham. All the Gleeble test samples in the thermosetting resin were glued to a special cylindrical mount using ethyl-2-cyanoacrylate adhesive and then placed inside the nanoindenter for testing. A picture of the Micromaterials NanoTest Nanoindenter at University of Birmingham is given below.

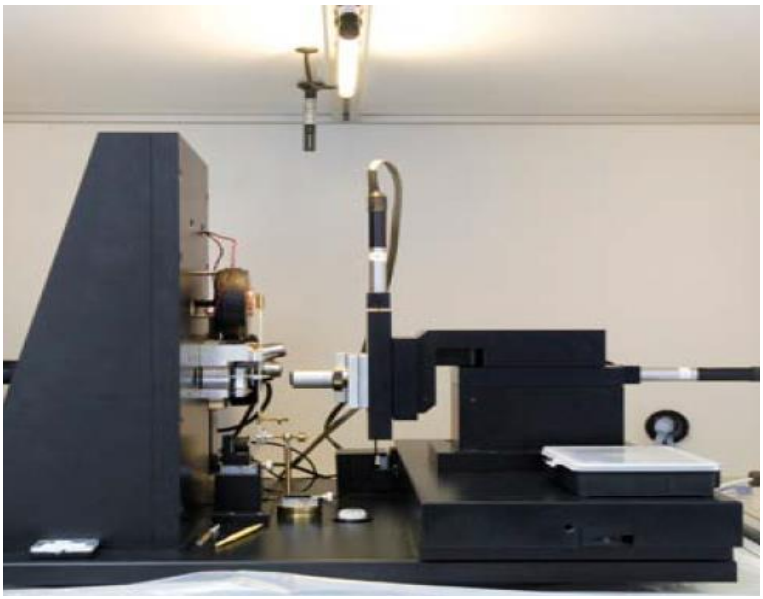

Figure 3.9: Micromaterials NanoTest Nanoindenter [132]

The peak load used for nanoindentation testing was fixed to be 0.8g and the dwell period at peak load was 20s [129]. An 18 x 18 array of nanoindents was taken on the cross-sectional area of each Gleeble test samples with a spacing of 150

micrometers in x-direction and spacing of 30 micrometers in y-direction as shown in Figure 3.10. The aim of the test was to get maximum possible number of nanoindents on the surface of the sample within the constraints of available time and available cross-sectional surface area of the samples. That was the main guiding force behind deciding the various parameters for the instrumented nanoindentation testing. A single test for 18 x 18 nanoindentation array on a sample took approximately 2 days to finish and this was repeated for all the 50 samples. The spacing between the indents was chosen so that it allowed for covering a majority portion of the cross-sectional surface area while at the same time ensuring that there is significant distance between neighboring indents.

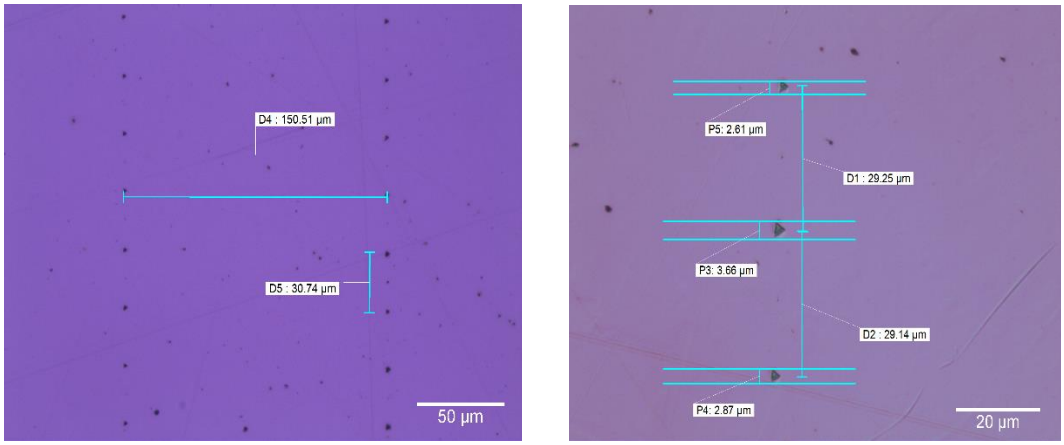

Figure 3.10: An array of nanoindents on the surface of a Gleeble test sample

Covering a majority portion of the cross sectional area of each sample allowed the indentation results to reflect as accurately as possible the phase distribution present in the localized region from where the thermal and mechanical history were

recorded. The dimensions of individual nanoindents were of the order of few microns as shown in Figure 3.10. As the Gleeble test samples were mounted in the epoxy resin mount, special care was taken to ensure that the indents were well inside the sample and hence not influenced by the boundary conditions. Once the nanoindentation testing was done, the data obtained for each sample was analyzed to get the volume fractions of different phases present in each sample. The process used for analyzing the nanoindentation data for phase fraction quantification is covered in detail in section 4.4 of the next chapter.

After the instrumented nanoindentation tests were finished for all the 50 samples, secondary testing was done for a selection of 8 randomly chosen samples for quantifying the uncertainty in phase fraction measurements obtained by this method. For all these 8 samples, a secondary 15 x 15 nanoindentation array with a spacing of 100 microns in x- direction and a spacing of 30 microns in y-direction was done with rest all parameters being same as during earlier tests. The results of both these primary and secondary nanoindentation tests are discussed in the next chapter and all the analysis done on the data obtained from them is presented in detail.

In the next chapter, the data generated from the experimental work discussed in this chapter is presented and all the preliminary processing done on the data to develop the final ANN dataset is discussed in detail.

Chapter 4

Development of the ANN Dataset

4.1 Overview

For the development of the ANN model an input dataset was required for training the model. The ANN training algorithm runs on the input dataset and learns the complex, multi-dimensional mathematical relationships existing between the input and output variables present in the dataset. The ANN model then uses that learnt knowledge from the training algorithm to make future predictions, when provided with completely new values for the input variables. The input variables for this ANN model consists of thermal history of the Gleeble samples, temperature of deformation and the amount of deformation that the sample underwent during Gleeble testing. The output variables for the ANN model consist of the martensite, bainite and ferrite phase fraction produced in the final microstructure based on the input thermal and mechanical history data of the sample.

All the experimental work detailed in the previous chapter was performed with the primary aim of generating the necessary data required for developing the ANN dataset, which can then be used for both training and validating the ANN model.

The Gleeble tests for physically simulating the tailored hot stamping process were done to generate the thermal and mechanical history data required for the input variables of the ANN dataset. The nanoindentation tests on the Gleeble test samples were done to generate the data for phase volume fraction quantification, as required for the output variables of the ANN dataset.

However all the raw thermal history data generated from the Gleeble tests had got noise present in it, the amount of deformation for each Gleeble sample at point of thermocouple welding had to be quantified and the raw hardness value data obtained from nanoindentation tests had to be processed to obtain the final phase fraction quantification for each sample. Thus a significant amount of further processing was required to be done on the raw experimental data before it became suiTable to be a part of the final ANN dataset. The focus of this chapter will be on explaining all the processing done on the raw experimental data and how that processed data was used for the development of the final ANN dataset.

4.2 Thermal history data processing

During the Gleeble testing, a thermocouple was welded to the centre of all the Gleeble test samples and the entire thermal history for the samples was recorded with the help of the thermocouple. For the tailored hot stamping process, all the phase transformations of interests begin once the blank is taken out of furnace after austenitization process at temperatures above 900°C. It is during this cooling

from the austenitization temperature to room temperature in the tailored hot stamping process, that austenite decomposes into different phases resulting in the final phase distribution. Thus during the physical simulation of the tailored hot stamping process in the Gleeble tests, the rate of thermal history data collection during cooling was kept at 100 data points per second. Hence during every second of cooling after austenitization, the thermocouple recorded 100 measurements of the temperature of the sample. Given in the Figure 4.1 below is a one second portion of time-temperature curve during cooling of one of the Gleeble samples, which was constructed using the original raw data collected by the thermocouple. The 100 datapoints in the Figure are the raw datapoints collected by the thermocouple, whereas the connecting line is just to display the time-flow and the order in which datapoints were recorded during the one second interval.

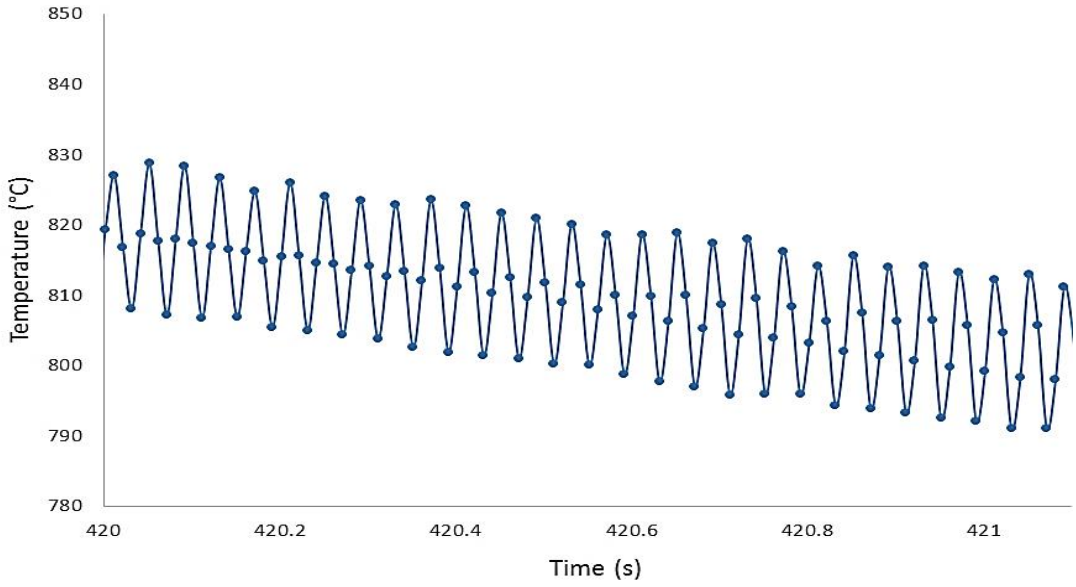

Figure 4.1: Raw thermal history data recorded from one of the Gleeble samples

As can be seen from the Figure there is noise present in the thermal history data recorded using the thermocouple during the Gleeble test. Thus the first step of processing the thermal history data involves removing this noise and getting a smoothed thermal history curve. Once we have obtained the smoothened thermal history curve from initial data processing, then the thermal history data corresponding to that curve can be parameterized to obtain the values required for the input variables to the final ANN model.

4.2.1 Smoothing of the thermal history curve

Because of the high data capture rate set during the cooling period of the Gleeble test, the data collected had a high density with respect to time (100 datapoints per second). For smoothing of such a highly dense data, locally weighted smoothing filter was selected [133]. Locally weighted smoothing involves replacing the value to be smoothed by a value predicted using a parametric function, which is fitted to only those observations that are in the neighborhood of the value to be smoothed. Thus in local smoothing the parametric function is used similarly to how it is used in normal global smoothing, but the only difference is that it is fitted locally in the neighborhood of the observation to be smoothed rather than going for a global fitting [133]. The main reason for selecting a localized smoothing over the global

fitting was the complicated nature of the thermal history curve obtained from thermocouple measurements. Global fitting would not have been able to successfully capture the complexities of the thermal path followed by the sample during the Gleeble tests trying to simulate the thermo-mechanical conditions of tailored hot stamping.

Now for the implementation of locally weighted smoothing in Matlab, there is a library function called *smooth* which has the option of using the '*lowess*' method [134]. The name *'lowess'* stands for 'locally weighted scatter plot smoothing' and it uses a linear polynomial as the parametric function for local fitting. The '*lowess'* method determines each smoothed value using a localized linear parametric fit on the neighbouring values present within a given span. Span is the percentage of total number of points present, which are to be used for locally weighted smoothing. The smoothing process is called weighted because the '*lowess'* function assigns a weight to each data point in the span, which is used to calculate the error contribution of that data point during localized parametric fitting. The '*lowess'* function uses the tricube function given below to compute the weight for each data point in the span:

$$w_i = (1 - \left|\frac{x - x_i}{d(x)}\right|^3)^3 \quad (4.1)$$

Where w_i is the calculated weight, x is the predictor value linked with the value to be smoothed, x_i is the neighbouring predictor point in the span for whose response

value the weight is being calculated and d(x) is the distance from x to the farthest predictor value within the span. Based on the characteristic of the tricube weight function the datapoint to be smoothed has the largest weight and hence the greatest influence on the parametric fit, whereas the influence of the point decreases as it moves further away in the span. The points outside span have no influence on the fitting as this is locally weighted smoothing.

For the smoothing of thermal history data, a span of 100 points was chosen so that it corresponds to the data rate capture of 100 per second. Thus in the code used in the Matlab, for each thermal history dataset the percentage corresponding to 100 datapoints (of total number of recorded datapoints using thermocouple for that sample) was calculated and that was input as the span in the '*lowess'* method for that sample. Using such a span in the 'lowess' method effectively leads to the application of locally weighted linear fitting to the data collected within a period of 1 second and smoothing of the value correspondingly. The thermal history data obtained from all the Gleeble tests were smoothed using the 'lowess' method and the same aforementioned span value was used for ever sample's thermal history data. In the Figure 4.2 given next, a time-temperature curve generated using both the smoothed thermal history data obtained after processing and the raw thermal history data for a 1 second period (for the same Gleeble test sample shown in Figure 4.1) is presented:

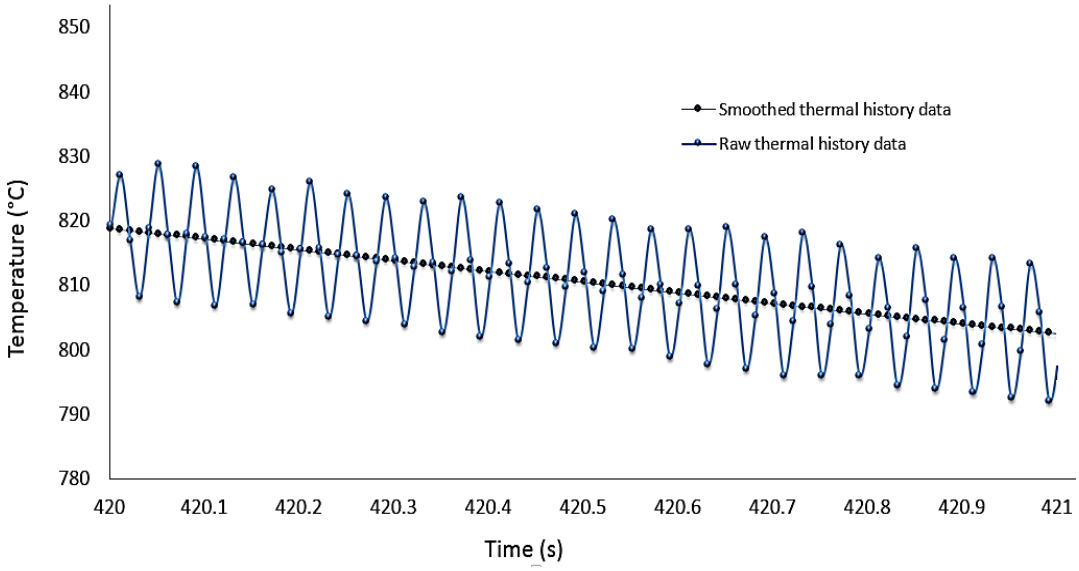

Figure 4.2: Raw thermal data vs smoothed thermal data obtained after processing

As can be seen from the Figure above the 'lowess' method appropriately removes all the noise/oscillations from the thermal history data and returns a nice smoothed thermal history data, which can then be used for generating the required input values for the final ANN dataset. Again the datapoints in the Figure are the actual raw and smoothed thermal history datapoints before and after processing, whereas the connecting line is just to display the time-flow and the order in which datapoints were recorded during the one second interval. However, as can be seen the smoothed thermal history data obtained after the processing is still discrete in nature. These discrete smoothed datapoints need further processing to generate the final values required for the input part of the ANN dataset.

4.2.2 Parametrization of the thermal history curve

For the tailored hot stamping process, all the important phase transformations which have the greatest influence on the final phase distribution in the microstructure take place during cooling after austenitization. The cooling of the blank starts as soon as it is taken out of the furnace and it is air-cooled to the deformation temperature during its transfer from furnace to the press. Once in the press, it undergoes both deformation and cooling simultaneously during the forming process. This thermal history that the part undergoes during tailored hot stamping was simulated in the Gleeble tests for different die temperatures and was recorded using the thermocouples. Thus in the thermal history recorded from the Gleeble tests, the time at 900°C, which corresponds to the blank being taken out of the furnace in the actual process, was assigned to be the beginning point (t=0s). All the following thermal history data was parameterized by converting it into the into the following input features: time to 800°C (s), time to 700°C (s), time to 600°C (s), time to 500°C(s), time to 400°C(s), time to 300°C(s), time to 200°C(s) and time to 100°C(s) all with respect to the beginning point of t=0 at 900°C.

This resolution of measuring time at 100°C intervals was selected as it was deemed to be sufficient to capture the complexities of the thermal paths of each Gleeble sample. As a result of the limited data being available from 50 Gleeble tests (because of external experimental resources constraint), any further resolution

(such as temperature intervals of 50°C or 20°C) would not have made any improvements for the final model but would have significantly increased the risk of overfitting in the final model.

In order to obtain precise value for each of the above mentioned input features, the thermal history data needs to be continuous so that the time at the exact required temperature could be calculated. Since the data available from thermocouple recording was discrete, *interpolation* was used to find the values between discrete datapoints. Because of the high frequency of data recording, the difference between two datapoints was just $1/100^{th}$ of a second during cooling. Linear interpolation is perfectly suited for such small intervals and hence was used to obtain the values for input features from the thermal history data in the Matlab. The Matlab function which was used for linear interpolation was 'interp1' [135]. The final values for input features obtained from thermal history data after all the processing are presented in the Table 4.1 below for one of the test samples:

Table 4.1: Thermal history data input variables for the ANN model

Time to 800°C (s)	Time to 700°C (s)	Time to 600°C (s)	Time to 500°C (s)	Time to 400°C (s)	Time to 300°C (s)	Time to 200°C (s)	Time to 100°C (s)
5.2	6.4	7.6	9.3	11.9	16.3	20.3	28.1

4.3 Measuring the deformation amount

In the Gleeble tests, electrical resistance heating was used for heating up the sample and for temperature control during cooling if required. The thermocouple welded to the centre of the sample measures the temperature at that point of welding and relays it back to the Gleeble machine as a part of the control loop mechanism. Because of the dog bone shaped geometry of the Gleeble test samples as shown in Figure 3.5, the cross-sectional area of the grips is greater than the cross-sectional area of the central region. This difference in the cross-sectional area leads to difference in the electrical resistance between the grips and the central region and this leads to differential heating between those two parts.

Since just the temperature measured at the point of thermocouple welding is part of the feedback control loop, the Gleeble tries to ensure that the temperature in that region follows the programmed thermal schedule. This leads to the grips being cooler than the central region and thus causing the heat to dissipate outwards from the central region. As a result of it there is a temperature gradient in the central region, with the point of thermocouple welding having the highest temperature and temperature falling on either side away from that region. Thus when high temperature tensile deformation was carried out during the Gleeble tests, it led to non-uniform elongation in the central region of the Gleeble test sample as shown in Figure 4.3 given below:

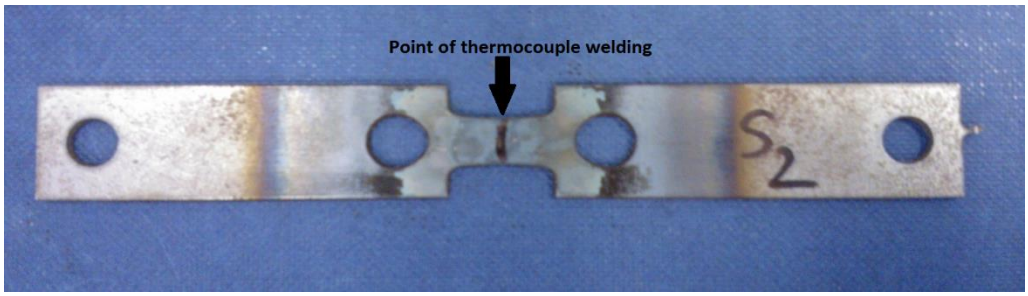

Figure 4.3: Sample with non-uniform elongation after high temperature tensile deformation during Gleeble testing

Because of this non-uniform elongation in the central region, it was difficult to quantify the exact amount of deformation present in the region of interest i.e the region of thermocouple welding. However, a reliable estimate of the amount of deformation present in the region of thermocouple welding for each sample is required as input for the ANN model. Thus, for each sample the width and thickness at the location of thermocouple welding was measured manually using *Vernier Caliper*. Then the engineering strain for the region was calculated by applying the principle of volume constancy relative to the original known volume of the undeformed sample for that region.

This method of strain measurement using numerical calculation yielded results with high precision. This high precision was just a result of the numerical method employed and not an actual reflection of the accuracy of the measurement. There was instrumental (Vernier Calipers) uncertainty present in all the different measurements used for estimating the final deformation amount, which lead to an

inherent uncertainty in the values for deformation amounts calculated using those measurements. Based on the uncertainty (instrumental) in measurements, the uncertainty in the calculated deformation amount for each sample was accounted for by classifying the calculated deformation amounts into a strain classes of 5% range rather than using the exact calculated values. Thus for each sample the final amount of deformation present in region of interest was quantified by classifying it into engineering strain classes such as 0-5%, 5-10%, 10-15%, 15-20% and so on.

4.4 Phase distribution quantification from nanoindentation data

For each Gleeble test sample, the cross-sectional area was scanned using an 18x18 grid of nanoindents and the hardness data obtained from the nanoindentation test was analyzed to get the phase distribution measurements of the sample. The hardness values obtained from nanoindentation testing were reported by the software in terms of contact pressure hardness values (GPa) and the equation 3.3 was used to convert them into vickers hardness values. Based on the previous works reported in literature for boron steel [5, 7, 52, 129], hardness values less than 200HV were classified as corresponding to ferrite, those between 200-400HV were classified as corresponding to bainite and those above 400HV as corresponding to martensite. The relative proportion of hardness values for each class, gives us the relative phase distribution of martensite, bainite and ferrite in the final microstructure. This was done for all the samples to obtain the relative

phase distribution in each of them after the Gleeble testing. These phase distribution values obtained from the instrumented nanoindentation testing formed the output part of the ANN dataset.

In order to measure the uncertainty in the phase distribution quantification obtained from nanoindentation testing, a secondary set of nanoindentation tests were done on a selection of 8 randomly chosen samples. The phase distribution values obtained from these secondary tests were compared with the original values to get an estimate of the variation observed in the phase fraction measurements obtained by nanoindentation testing. The absolute difference between the phase fraction values obtained from the primary and secondary tests were calculated for all the samples on which secondary testing was done. The average value of absolute difference in the phase volume fraction measurements between the original tests and the secondary tests was found to be 4.7%. The standard deviation for the absolute difference measurements was found to have a value of 3.5.

Now usually 95% of the values fall between mean $\pm$ (2 x standard deviation). This was used for calculating the upper limit of the value of absolute difference based on the measurements obtained from primary and secondary testing. This upper limit would capture the uncertainty present in phase fraction measurements obtained by nanoindentation testing and will provide us with a reliable range around the measured value in which the true value of the phase fraction is

expected to be present. The value of upper limit on absolute difference is given by:

$$Mean + (2 \text{ x } Standard\ Deviation) \tag{4.2}$$

$$= 4.7 + (2 \text{ x } 3.5)$$

$$= 11.7$$

Thus the absolute uncertainty in a phase fraction measurement obtained by nanoindentation testing is 11.7%. This means that it can be expected that 95% of time the absolute difference between the true value of the phase fraction and the value obtained from nanoindentation testing will be less than 11.7%. This uncertainty calculation gives us an idea about the reliability of the measurements obtained by nanoindentation testing and gives us the range in which the true value of the phase fraction can be expected to be found with 95% probability.

4.5 Data Normalization and final dataset

Once all the data had been collected and analyzed it was used to create the final ANN dataset with 50 datapoints corresponding to the 50 Gleeble tests performed. Out of these 50 datapoints, 40 datapoints were randomly chosen to form the input dataset used for training and development of the final ANN model. In order to speed up the training process, data normalization was used for the data corresponding to input variables. The idea behind it is that since the range for data in input variables can vary widely, that will affect the convergence of the learning

algorithm and make it more computationally expensive and time consuming. Using data normalization has also got other advantages for neural networks such as better error function surfaces and preventing the training algorithm from getting stuck at local minima during learning. This directly helps in improving the final performance of the neural network model and increasing its prediction accuracy [136]. The data normalization method applied to the input data used the mean and range of the variable for data normalization:

$$y_i = \frac{x_i - x_{mean}}{\max(x) - \min(x)} \tag{4.3}$$

Where x is the input variable, x_{mean} is the mean for the variable, x_i is the value of variable x that is to be normalized and y_i is the corresponding normalized value. Based on all the experimental work and pre-processing of the experimental data, a final ANN dataset was created which was used for development and validation of the final ANN model. All the input and output features of the ANN dataset along with their range of values are listed in Table given below:

Table 4.2: Input and output features of the final ANN dataset

Input 1	**Input 2**	**Input 3**	**Input 4**	**Input 5**	**Input 6**	**Input 7**	**Input 8**	**Input 9**	**Input 10**	**Output**
Time to 800° C (s)	Time to 700° C (s)	Time to 600° C (s)	Time to 500° C (s)	Time to 400° C (s)	Time to 300° C (s)	Time to 200° C (s)	Time to 100° C (s)	Deformation Amount (strain class)	Deformation Temperature (°C)	Martensite, Bainite & Ferrite phase fraction values (%)
Cooling process should finish within 170s after starting at 900°C (within the range of industry standard)								0-5% to 55-60%	850°C-700°C	0-100

In the next chapter, the ANN dataset developed in this chapter is used for the training and development of the final ANN model. The entire process followed for the development of the ANN model by using backpropagation algorithm for its training is discussed in detail. Also the measures taken for preventing the occurrence of overfitting in the final ANN model are described and the uncertainty in the predictions made by the ANN model is quantified.

Chapter 5

ANN Model Development

5.1 Overview

A reliable prediction of the final phase distribution in the microstructure of tailored hot stamped parts is really important from the manufacturing perspective. Having a model which is able to make such final phase distribution predictions accurately based on input processing parameters, will allow us to optimize those input processing parameters to obtain the desired mechanical properties distribution in the final hot stamped parts. But in order to make such reliable predictions a model is required which is able to account for the effect of deformation and its interactions with the thermal history, something which most of the existing models do not take into consideration [17, 110-112]. Artificial Neural Network (ANN) based modeling is well suited for such a problem where the final output is a function of multiple input variables and the model is required to capture not only the effect of each individual variables on the final output but also the effect of interactions between those input variables on the final output [119]. An ANN

based model is a complex mathematical model which can learn any kind of complex multivariate functional relationships between the input and output parameters from the available input dataset and in this chapter the entire process followed for the development of the ANN based model is documented in detail.

5.2 General ANN architecture and learning process

A multi-layered feed-forward Artificial Neural Network architecture has been used in this research. Each model consisted of an *input* layer, two *hidden* layers and an *output* layer. Both hidden and output layers in the ANN based model are made up of individual computational units called neurons. This complex system of interconnected neurons present in ordered layers makes up the ANN model [137]. A neural network with one input layer, two hidden layers and one output layer is shown in Figure 5.1 given below:

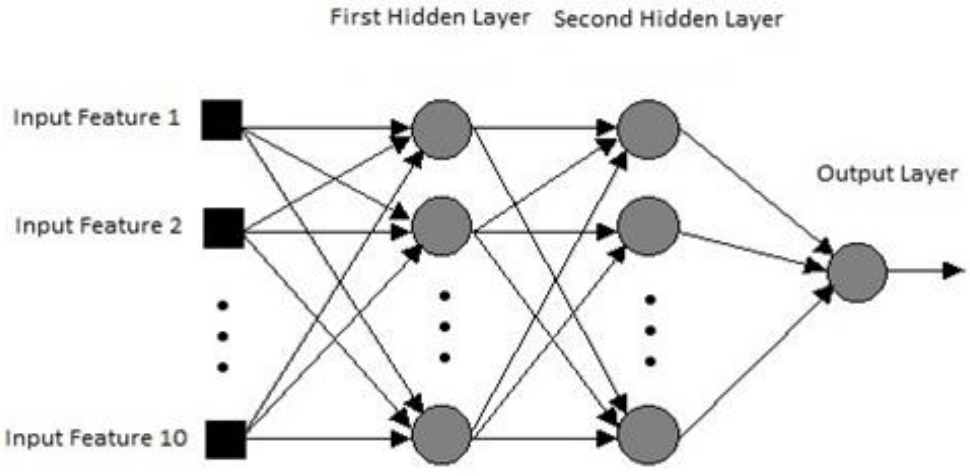

Figure 5.1: Network architecture of an ANN model

The input layer is made up of input features which take up the input parameter values required for making final prediction. Each neuron in the hidden layer and output layer has got a corresponding set of weights attached with it. For each neuron, all its inputs from previous layer are multiplied with the corresponding set of weights attached with that neuron and then the linear summation of those products is taken as the input for that neuron. Suppose a neuron has got a total of n inputs x_0, x_1, x_2 ….. x_n and a corresponding set of n weights w_0, w_1, w_2 ……. w_n. Then the input y for that neuron is given by the linear summation of corresponding product of weights and inputs from previous layer:

$$y = w_0x_0 + w_1x_1 + w_2x_2 + \ldots\ldots\ldots + w_nx_n \qquad (5.1)$$

The neurons which directly use this linear summation of the product of its inputs and weights to calculate their output are known as *linear* neurons. Neurons which use the *sigmoidal/logistic* function on their calculated input to generate their output are known as sigmoidal units [137]. The function used by the neuron on its input to generate the output is known as the *activation function* for that neuron. The basic mathematical form of sigmoidal function is as follows:

$$f(y) = \frac{1}{(1+\exp(-y))} \qquad (5.2)$$

Initially the set of weights for each neurons are randomly chosen and thus the output values predicted by the model do not match with the corresponding output

values present in training dataset. The output generated by the model is used to calculate the error in the prediction and then weights are iteratively updated so as to reduce this error. This process of iteratively updating the weights of the individual neurons in the neural network to reduce its prediction error, so that it starts to simulate the complex multivariate functional relationship present between input and output parameters in the training dataset, is what constitutes the process of *learning* during ANN based modeling.

For this project the neural network topology with one input layer, two hidden layers and one output layer was chosen as it has been shown theoretically that such a neural network can model any complex non-linear multivariate functional relationship with a fixed degree of accuracy [138]. This result applies to neural networks which use sigmoidal units in the hidden layers and linear units in the output layer and hence the activation function for the neurons in the hidden layer was selected to be sigmoidal and for the neurons in the output layer was selected to be linear for the final ANN model.

5.3 Backpropagation algorithm implementation

Backpropagation algorithm is one of the most widely used learning algorithms for the training of ANN models and was thus used for the development the final ANN model in this project [139]. Backpropagation algorithm uses advanced multivariate

calculus to learn the final values of weights through iterative updating in a multilayer neural network with a given set of neurons and interconnections. Backpropagation algorithm ensures that the total prediction error of the model effectively decreases during every weight update iteration and after sufficient number of iterations, model ends up learning the functional relationships present between the input and output variables in the training dataset.

The first step for the implementation of the backpropagation algorithm is to define the prediction error of the neural network based model. The sum of the squared errors is used to calculate the prediction error E between the output values predicted by the neural network and the target output values as given below.

$$E = \frac{1}{2} \Sigma_{d \epsilon D} \Sigma_{k \epsilon K} (t_{kd} - o_{kd})^2 \qquad (5.3)$$

Where D is the set of all training examples for training the neural network, K is the set of all output units in the output layer of the neural network, t_{kd} is the target value for the k^{th} unit in the output layer for training example d and o_{kd} is the output value predicted by the k^{th} output unit of the network for the same training example. Now as this prediction error E is a function of the value predicted by the model, it is a function of the weights of individual neurons which constitute the model. The learning problem for the backpropagation algorithm involves traversing through the *high dimensional hypothesis space* of this error function, which is defined by

all the possible weight values of all the neurons, so as to find a unique set of weights for each neuron in the neural network such that the prediction error is minimized.

The training rule used for updating the weights in the backpropagation algorithm is known as *gradient descent*. Gradient descent starts with random initialization of all the weights in the network and then updates them in small steps in each iteration using partial derivative of the error function with respect to individual weights. The partial derivatives of the error function with respect to individual weights are used to find the direction in the hypothesis space which would lead to the steepest decrease in the prediction error after each iteration. The gradient descent based weight update rule used in implementation of the backpropagation algorithm for the model is given below [140]:

$$w_{i+1} = w_i - \alpha \frac{\partial E}{\partial w_i} \tag{5.4}$$

Where w_{i+1} is the updated weight after i^{th} iteration, w_i is the existing value of the weight before i^{th} iteration update, α is the learning rate and $\partial E/\partial w_i$ is the partial derivative of the prediction error E with respect to weight w_i. The learning rate α determines the step size in the gradient descent search and for a sufficiently small value of α, the gradient descent weight update leads to decrease in the prediction error[140].

The most challenging part in the implementation of the backpropagation algorithm is to calculate the value of the partial derivatives of the error with respect to individual weights of neural network, so that those values can be used for updating the weights using the gradient descent rule after each iteration. Backpropagation algorithm uses multivariate calculus to calculate the values of required partial derivatives and the standard notations used in backpropagation algorithm calculation are given in the Table 5.1 below. The algorithm described below was employed for training the multi-layered feed forward neural network developed in this research work [137].

Table 5.1: Standard notation used in derivation of the backpropagation algorithm

Notation used	**Meaning of the symbol**
x_{ji}	Input from unit i in the previous layer to unit j in multi-layered neural network
w_{ji}	weight associated with the i^{th} input to unit j
net_j	$\Sigma w_{ji}x_{ji}$: The weighted sum of inputs for unit j
t_k	The target value for k^{th} unit in the output layer for a given training example
O_j	The output value computed by the j^{th} unit in any layer for a given training example
σ	Sigmoidal function as given by eq (5.2). Thus for a sigmoidal unit j we have $o_j = \sigma(net_j)$
Downstream(j)	The set of all units in the next layer whose input includes the output of unit j from the previous layer

Now for a neural network with d training examples and k output units in the output layer, the network prediction error E is given by:

$$E = \frac{1}{2} \Sigma_{d \epsilon D} \Sigma_{k \epsilon K} (t_k - o_k)^2 \quad (5.5)$$

For a fixed single training example d, the network prediction error E_d is given by following equation:

$$E_d = \frac{1}{2} \Sigma_{k \epsilon K} (t_k - o_k)^2 \quad (5.6)$$

Thus the overall performance error for the neural network over all the training examples can be written as:

$$E = \Sigma_{d \epsilon D} \left(\frac{1}{2} \Sigma_{k \epsilon K} (t_k - o_k)^2 \right) \quad (5.7)$$

$$= (E_1 + E_2 + \ldots\ldots\ldots + E_d)$$

Now for implementing gradient descent using backpropagation algorithm for learning the network weights we would need:

$$\frac{\partial E}{\partial w_{ji}} = \frac{\partial}{\partial w_{ji}} (E_1 + E_2 + \ldots\ldots\ldots + E_d) \quad (5.8)$$

$$= \frac{\partial E_1}{\partial w_{ji}} + \frac{\partial E_2}{\partial w_{ji}} + \cdots\ldots\ldots\ldots + \frac{\partial E_d}{\partial w_{ji}}$$

Thus for each individual training example the gradient of individual error with respect to network weights was calculated and then those individual training example gradients were summed up to obtain the overall gradient with respect to

network weights as given by the above equation. Now for calculating the error gradient with respect to a specific weight for an individual training example the following steps were followed. A weight w_{ji} in the any layer can affect the network output only through net_j and similarly net_j can affect the network output only through o_j. Therefore by applying the differentiation chain rule we get:

$$\frac{\partial E_d}{\partial w_{ji}} = \frac{\partial E_d}{\partial net_j}\frac{\partial net_j}{\partial w_{ji}} \tag{5.9}$$

$$= \frac{\partial E_d}{\partial o_j}\frac{\partial o_j}{\partial net_j}\frac{\partial net_j}{\partial w_{ji}}$$

Thus individual error gradient with respect to weight w_{ki} in the k^{th} linear neuron in the output layer was calculated as shown below:

$$\frac{\partial E_d}{\partial w_{ki}} = \frac{\partial E_d}{\partial o_k}\frac{\partial o_k}{\partial net_k}\frac{\partial net_k}{\partial w_{ki}} \tag{5.10}$$

Now for the linear neuron $\partial E_d/\partial o_k$ is given by:

$$\frac{\partial E_d}{\partial o_k} = \frac{\partial}{\partial o_k}\left[\frac{1}{2}\Sigma_{k\epsilon K}(t_k - o_k)^2\right] \tag{5.11}$$

$$= -(t_k - o_{k)}$$

Since for a linear neuron we have $o_k = net_k$, we get $\partial o_k/\partial net_k = 1$. And for that neuron as $net_k = \Sigma_i w_{ki}x_{ki}$ we get:

$$\frac{\partial net_k}{\partial w_{ki}} = \frac{\partial}{\partial w_{ki}}(w_{k0}x_{ko} + \ldots + w_{ki}x_{ki} \ldots . + w_{kn}x_{kn}) = x_{ki} \tag{5.12}$$

Thus the final value of the individual error gradient with respect to weight w_{ki} of the kth output unit in the final layer was obtained by combining equations 5.11 and 5.12 as given below in equation 5.13:

$$\frac{\partial E_d}{\partial w_{ki}} = \frac{\partial E_d}{\partial o_k} \frac{\partial o_k}{\partial net_k} \frac{\partial net_k}{\partial w_{ki}} \tag{5.13}$$

$$= -(t_k - o_k) \,.\, 1 \,.\, x_{ki}$$

$$= -(t_k - o_k)\, x_{ki}$$

The above equation was used to calculate the individual error gradients for all the weights in the final output layer during the implementation of the backpropagation algorithm and then those individual error gradients were summed up according to the equation 5.8 to obtain the final error gradients.

Now for a weight w_{ji} in the sigmoidal unit in the hidden layer, the individual error gradient was calculated as following:

$$\frac{\partial E_d}{\partial w_{ji}} = \frac{\partial E_d}{\partial net_j} \frac{\partial net_j}{\partial w_{ji}} \tag{5.14}$$

Again for a hidden sigmoidal neuron we have $net_j = \Sigma_i w_{ji} x_{ji}$ and thus we get:

$$\frac{\partial net_j}{\partial w_{ji}} = \frac{\partial}{\partial w_{ji}} \left(w_{j0} x_{jo} \,.\ldots + w_{ji} x_{ji} \,\ldots. + w_{jm} x_{jm} \right) = x_{ji} \tag{5.15}$$

As each neuron in the hidden layer is connected to all the neurons in the next layer, by application of the chain rule again we get following:

$$\frac{\partial E_d}{\partial net_j} = \Sigma_{l \in downstream(j)} \frac{\partial E_d}{\partial net_l} \frac{\partial net_l}{\partial net_j} \quad (5.16)$$

Now as $net_l = w_{l0}x_{lo} + w_{l1}x_{l1} + \ldots + w_{lj}x_{lj} \ldots + w_{ln}x_{ln}$ and since the neuron in the hidden layer is a sigmoidal unit we get:

$$\frac{\partial net_l}{\partial net_j} = \frac{\partial}{\partial net_j}\left(w_{l0}x_{lo} + w_{l1}x_{l1} + \ldots + w_{lj}x_{lj} \ldots + w_{ln}x_{ln}\right) \quad (5.17)$$

$$= w_{lj} \frac{\partial x_{lj}}{\partial net_j}$$

$$= w_{lj} \frac{\partial o_j}{\partial net_j}$$

$$= w_{lj} \frac{\partial \sigma(net_j)}{\partial net_j}$$

$$= w_{lj} o_j (1 - o_j)$$

Using the above result, equation 5.16 can be rewritten as:

$$\frac{\partial E_d}{\partial net_j} = \Sigma_{l \in downstream(j)} \frac{\partial E_d}{\partial net_l} w_{lj} o_j \left(1 - o_j\right) \quad (5.18)$$

$$= o_j \left(1 - o_j\right) \Sigma_{l \in downstream(j)} \frac{\partial E_d}{\partial net_l} w_{lj}$$

Now let the terms $\partial E_d/\partial net_j = \delta_j$ and $\partial E_d/\partial net_l = \delta_l$ and so we can write the above equation as:

$$\delta_j = o_j \left(1 - o_j\right) \Sigma_{l \in downstream(j)} \delta_l w_{lj} \quad (5.19)$$

This term δ was first calculated for all the neurons present in the output layer, while calculating the individual error gradients for the weights in the final layer. After that the values for δ obtained for the final layer, were used to calculate the δ values for the layer preceding it. In this way the δ values were propagated backwards from the final layer, until δ values had been calculated for all the neurons in the neural network. Once that was done, then equation was used to calculate the individual error gradients for the weights in the hidden layers. Finally after the individual error gradients had been calculated for all the training examples, their values were added up according to equation 5.8 to obtain the final error gradients for all the weights in hidden layer.

Once the error gradients had been calculated for all the weights both in hidden layers and output layer of the neural network, then they were used to update the weight values using the gradient descent rule in each iteration. This entire backpropagation algorithm was coded in Matlab and used for training the ANN model on the input dataset.

5.4 Numerical gradient calculation check

As seen from the last section, backpropagation algorithm is a very complicated algorithm involving advanced application of multivariate calculus. Even the smallest mistake during implementation of the backpropagation algorithm can

have a cascading effect and lead to a significant error in calculation of the final error gradients. Any mistake in the calculation of error gradient would be catastrophic and would lead to failure of the ANN model because there can be no learning from the training dataset without the correct values for error gradients. Thus it was of utmost importance to ensure that the gradients calculated by the backpropagation algorithm were accurate. In order to ensure this, a numerical error gradient calculation was done for all the weights in the neural network during the first iteration to cross check against the gradient values calculated by the backpropagation algorithm. The backpropagation algorithm was allowed to proceed to the next iteration only if the gradient values calculated by it matched with the gradient values calculated by the numerical method within a specific tolerance level.

The numerical error gradient calculation method for a given weight w_{ji} in the neural network involved calculating two new values for the given weight w_{ji} by adding and subtracting a fixed value Δ to its existing value, while keeping the values for all other weights in the network constant. The value for Δ in the numerical gradient calculation should be tending towards zero, so as to accurately estimate the error gradient for that weight. The value for Δ that was used in the implementation of the code was 10^{-5}. Next the sum of squared prediction errors E_1 and E_2 were calculated for two new networks, which had all the weight values

same as the old network except for the value of the weight w_{ji}. E_1 was calculated using the value $w_{ji}+\Delta$ and E_2 was calculated using the value $w_{ji}-\Delta$. The error gradient with respect to weight w_{ji} for the original neural network under consideration was then calculated by:

$$\frac{\partial E}{\partial w_{ji}} = \frac{E_1 - E_2}{2\Delta} \tag{5.20}$$

This gradient value obtained by the numerical method was cross checked with the value obtained by the backpropagation algorithm and the learning algorithm was allowed to proceed to the next iteration only if the absolute difference between those two values was less than the tolerance of 0.00001 i.e. effectively zero.

Similarly error gradients were calculated for all the weights in the neural network using the numerical method described above during the first iteration. Their values were checked against the values calculated by the backpropagation algorithm to ensure that the code was calculating the required gradients correctly and that everything was functioning as it was expected to. As this numerical gradient calculation method is computationally much more expensive relative to the backpropagation algorithm, once it had been verified that the backpropagation algorithm was indeed calculating the gradients accurately the numerical method check was discontinued.

5.5 Learning rate for the backpropagation algorithm

The learning rate α used during the gradient descent in backpropagation algorithm determines the step size of the change while updating the weight values after each iteration. Using higher value for the learning rate α leads to faster learning and the algorithm converging faster to the error minima in the hypothesis space. A risk associated with using high values of α is that the size of change in the weight values during update might be too big and would lead the prediction error for the network to increase instead of decreasing.

On the other hand, using very small values for the learning rate α would lead to slower rate of learning and thus lead to larger number of iterations being required for the network to get trained. Each iteration of backpropagation algorithm has a computational expense attached to it and thus increasing the number of iteration directly leads to an increase in the computational effort and time involved in learning. Thus during the implementation of the backpropagation algorithm in this research work, the value for the learning rate α was not kept constant but instead was kept dynamic so that it could evolve according to the requirement. The initial value fixed for the learning rate α was 0.03 and after that its value was decreased whenever the value of prediction error increased after the application of gradient descent during an iteration. The updated value of learning rate α during an iteration in case of increase in the prediction error was given by:

$$\alpha_{updated} = \frac{\alpha_{current}}{1.1} \quad (5.21)$$

5.6 Division of the ANN dataset

All the data obtained from experimental work was used to generate and validate the final ANN based phase distribution prediction model. The final ANN dataset created from the experimental data, as detailed in the previous chapter, consisted of a total of 50 datapoints corresponding to 50 Gleeble tests. Out of these total 50 datapoints, 40 datapoints were randomly chosen to constitute the input dataset as shown in Figure 5.2 given below. This input dataset was used for developing and training the ANN based model for the final phase distribution prediction in the tailor hot stamped parts based on their thermal and mechanical history.

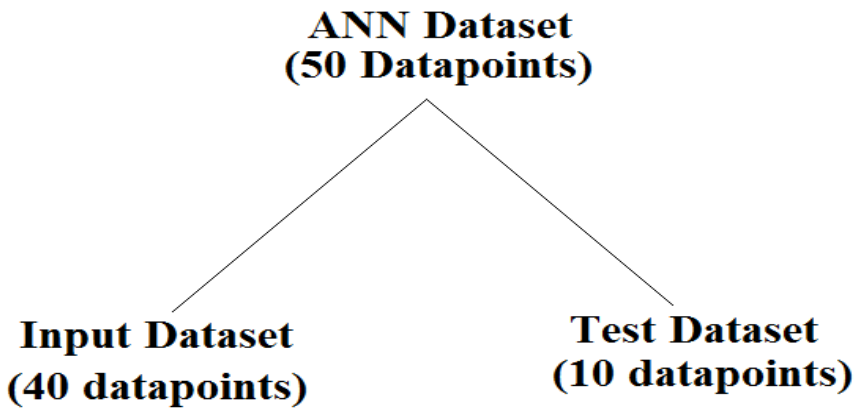

Figure 5.2: Division of the ANN dataset into input and test datasets

The remaining 10 randomly chosen datapoints from the original ANN dataset made up the test dataset and were used for validating the performance of final ANN model. The predictions made by the final ANN model were tested against the experimental values present in the test dataset to ensure that the predictions made by the model were reliable and matched what was observed in the physical world. These 10 datapoints constituted completely new data which the ANN model had never encountered before and thus the model's performance on this new data gives an idea about the generalization capability of the final ANN model. This evaluation of the ANN model's performance on the test dataset is equivalent to establishing the validity of any theoretical model by measuring its prediction against the data generated from experimental work. This exercise gave us a definitive estimate of the reliability of the predictions made by the final ANN model when presented with completely new input data.

5.7 Underfitting and overfitting

An important point to be considered while training the neural network using the backpropagation algorithm is the criteria for deciding the stopping point of the learning process and for choosing the final set of weights for the ANN model. If the training is stopped too early then it leads to poorly trained network, which did not get enough time to learn the mathematical relationships present within the

input dataset. Such a poorly trained network ends up *underfitting* the training examples and giving a relatively high prediction error even on the input dataset. The performance of such a network deteriorates even further when it is given completely new data and it generalizes quite poorly [119, 137].

On the other hand if the training is allowed to continue for too long, then it leads the neural network to adjust its weights too much and *overfit* the data in the input dataset. During overfitting the neural network starts tuning its weights to fit the minor variations in the input dataset, which might be a result of the noise in the data collection procedure rather than being representative of generalized data. An interesting outcome of overfitting is that the model will give good performance on the input dataset but generalize quite badly on any new data [119, 137].

For this project the aim is to develop a robust and reliable ANN based model which can perform well beyond the input dataset used for its development, so that the final model can be used for engineering application. The model needs to have good generalization capabilities on new independent data which it has not encountered before, so that the predictions made by it can be relied upon for engineering decision making. Thus the stopping criteria during the training of the ANN model and choosing the final set of weights for the ANN model are important factor from underfitting/overfitting perspective, which need to be taken into consideration for developing the final ANN based model.

5.8 Cross-validation

Cross validation is a statistical concept which helps in solving the dilemma of underfitting and overfitting during the training of the ANN model [137]. The idea behind the cross validation approach is to randomly divide the input dataset further into two separate and mutually exclusive parts called the training dataset and the cross validation dataset. The training dataset is only used for training the model while the cross validation dataset is used for investigating how the model performs when it encounters new data. Thus the model's performance on the cross validation dataset gives an idea about the generalized performance capability of the model beyond the training dataset and allows us to develop the optimal model during its training and development stage.

However as the data from the cross-validation set is used to determine the stopping criteria and to select the final weights for the ANN model during its training, the model's performance on the cross-validation set does not give us the true estimate of it generalization capability. The reason behind this is that the data in the cross-validation set has already been exposed to the model and optimal values for the stopping criteria and the final weights were chosen such that the model gives the best performance on the cross validation set. Thus it can be thought of as model being biased towards the cross validation set and giving a lower cross validation error compared to its true generalization error. That is why a completely separate

test dataset is maintained to measure the true generalization performance of the final ANN model when it encounters completely new and independent data.

This cross validation based approach described above, which involved the division of the input ANN dataset into training set and cross validation set, was used for selecting the final number of iterations to undergo while learning and for selecting the final set of weights during the development of the ANN model.

5.9 Number of iterations and choosing the final weights

Based on the cross-validation approach described in the previous section, the available input dataset of 40 datapoints was randomly divided into two part: 30 datapoints for the training dataset and 10 datapoints for the cross-validation dataset as shown in Figure 5.3 given below.

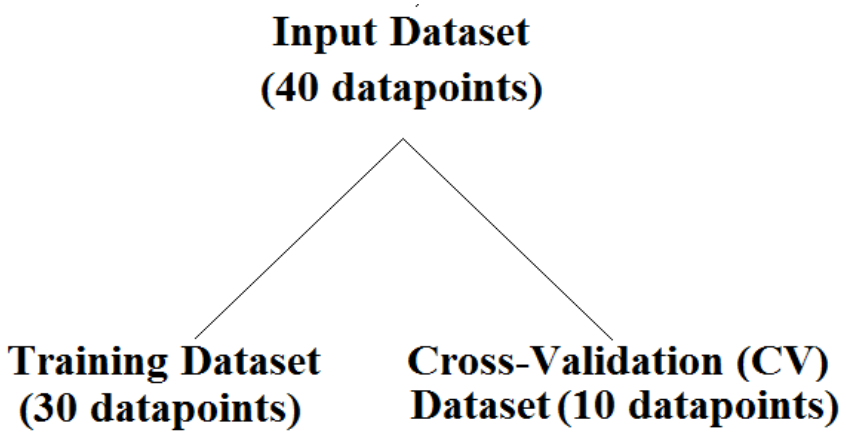

Figure 5.3: Division of the input dataset into training and cross-validation(CV) sets

As discussed earlier, the number of iterations during the learning process and choosing the final set of weights at the end of the learning process are important parameters which affect the model's final performance from underfitting/overfitting perspective. Even after model has done its fixed number of iterations on the training dataset, it's not necessary that the final set of weights obtained at the end of process have the best generalization capability. The reason behind it being that we do not know if the model has overfitted on the training dataset or not. That is where the cross-validation dataset comes into picture and helps in determining the optimal set of weights with the best generalization capability for the ANN based model.

Figure 5.4: RMS prediction error for training and cross-validation (CV) sets versus number of iterations for backpropagation algorithm

In this cross validation based approach, the model's root mean square (RMS) prediction error for phase volume fractions was calculated both on the training dataset and cross validation dataset during each iteration. After each iteration the latest copy of the neural network weights was saved only if the prediction error had decreased on the cross validation dataset during that iteration. In the Figure 5.4, a plot for RMS prediction error on training dataset and RMS prediction error on cross validation dataset versus the number of iterations is shown for backpropagation algorithm that terminates after a total of 10^5 iterations.

In the beginning of the training as the model starts to tune its weights from random initialization, the prediction error was observed to decrease both in the training dataset and the cross validation dataset. Proper implementation of the backpropagation algorithm ensures that the prediction error consistently decreases in the training dataset during learning. However after a certain point when the model had learnt as much as it could from the training dataset, it started to overfit on the training data to keep on further reducing its prediction error.

At this point, the model's performance on the cross validation dataset started to deteriorate and its prediction error on the cross validation dataset started to increase. However as the neural network weights were saved only when the prediction error decreased on the cross validation set, the final weights that were saved at the end of the learning process were the weights which gave the lowest

error on the cross validation set. These were the weights which gave the best generalization performance when presented with the new data from the cross validation set and thus constituted the set of weights which defined the optimal ANN model. This cross validation based approach was used for determining the final weights of the ANN model during every implementation of the backpropagation algorithm, so as to avoid the occurrence of overfitting during learning by the ANN model [137].

Now for number of iterations, on top of underfitting/overfitting concern, each iteration during learning has got a fixed computational expense associated with it. Thus each iteration during learning takes a fixed amount of time to execute and so it is not possible to allow the backpropagation algorithm to run infinitely. An upper limits needs to be set for the algorithm to terminate automatically, so that the learning process stops within a finite time period. The most important point that needs to be accounted for while fixing the upper limit on the number of iterations, is the fact that it should provide sufficient time for the neural network to learn all the functional relationships present in the available training data. This would ensure that the number of iterations is sufficient, so that the ANN model does not end up underfitting the training data.

Now in order to determine the optimal value for the upper limit on number of iterations in the backpropagation algorithm, three different randomly initialized

ANN model were trained using an upper limit of 10^5 iterations and their cross-validation error histories were recorded. All the ANN models used for the analysis had 20 sigmoidal neurons in each of their two hidden layers and three linear neuron in their output layer corresponding to each of the three phases. For each of the ANN models the weights were randomly initialized and the number of iterations which were required for the models to attain their cross-validation error minima were observed. The final RMS prediction error history for each individual model on the cross validation dataset is plotted against number of iterations as shown in the Figure 5.5 given below.

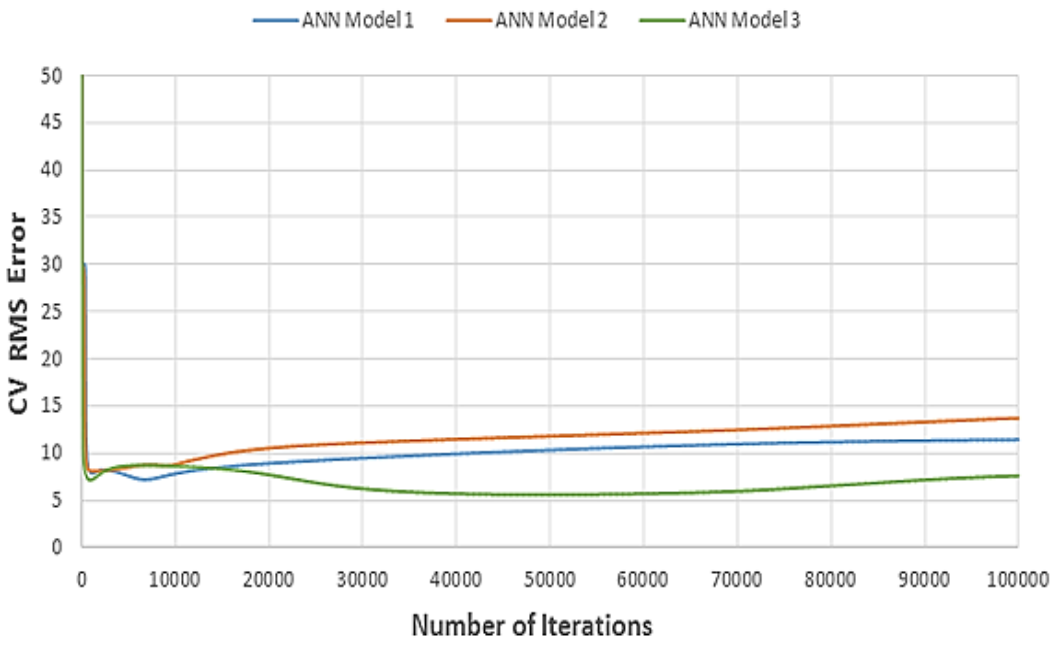

Figure 5.5: RMS prediction history on cross-validation (CV) dataset for 3 randomly initialized ANN models

As seen from the Figure, models 1 and 2 found the minima of their cross validation error quite early within 10,000 iterations during their training. However the cross validation history of model 3 follows an interesting path. Initially it also appears to find a minimum at quite early on in the training, after which the cross validation error starts to increase. Though after a couple of thousand iterations the cross validation error again starts to decrease and this time finds its true minimum somewhere near $50{,}000^{th}$ iteration. Thus if the upper limit on the number of iteration had been less than 50,000 then the neural network weights corresponding to the first minima of model 3 would have been accepted as the final weights for the model after the learning process. Those weights do not correspond to the best possible generalization performance for the model 3.

Now for 2 out of 3 test models their true cross validation minima was found before $10{,}000^{th}$ iteration, whereas for the 3^{rd} model its true cross validation minima was found somewhere near $50{,}000^{th}$ iteration. Thus for all the 3 models their learning process finished well within the upper limit of 10^5 iterations. Based on this performance of different ANN models and their cross validation error histories, the final upper limit on the number of iterations was selected to be 10^5 iterations for all the future implementation of the backpropagation algorithm for this research. From the available data, it was concluded that 10^5 iterations during the backpropagation algorithm implementation will provide the ANN models with sufficient time for learning all the available functional relationships present in the

training dataset and thus help in avoiding underfitting of the neural network model. Finally the set of weights during those 10^5 learning iterations, which give the best performance on the cross validation set will be selected as the weights for defining the final ANN model.

5.10 K-fold cross-validation

So far the division of the entire ANN dataset consisting of 50 datapoints, corresponding to the 50 Gleeble tests, was done as shown in Figure 5.6 below.

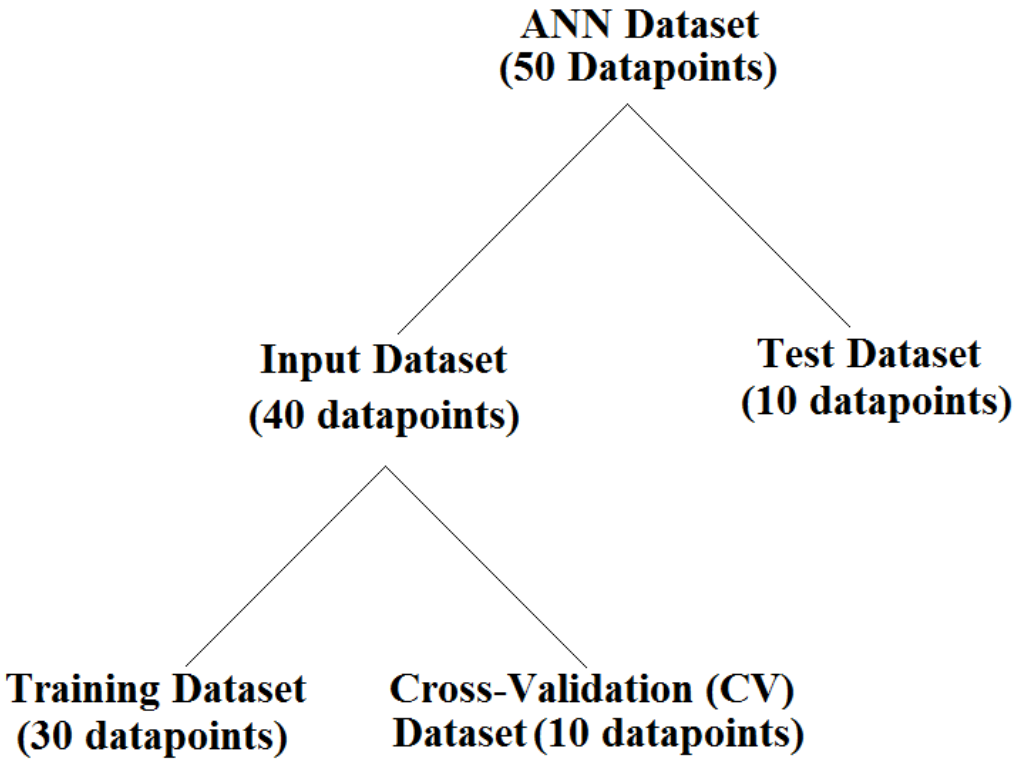

Figure 5.6: Complete division of the ANN dataset

Due to the limited availability of the experimental resources, the input dataset at hand for training and development the final ANN model was limited to a total of 40 datapoints. Thus it was imperative that the final ANN model made use of all the available data, so that it can maximize its learning and give a good generalization performance. When we divide the input dataset into training dataset and cross validation dataset, we lose the knowledge of the functional relationships present in the cross validation dataset. The datapoints in cross validation dataset are not used for training the ANN model and thus the ANN model cannot learn the functional relationships present in those datapoints. K fold cross validation is a variant of cross-validation technique which is especially useful when working with such small datasets and provides a way around this significant limitation [137].

In the K-fold cross validation method, the cross validation procedure is carried out K separate times; each time using a different and mutually exclusive cross validation set chosen randomly from the input data. Thus if there are a total of m training examples in the input dataset, then k different disjoint subsets of equal size m/k are randomly selected from the input dataset. Then every time one out of those k disjoint subset is used for cross validation, whereas all the remaining datasets are joined together to form the training dataset. Thus in this method each available datapoint is used for cross validation at least one time and then it is used for training the remaining k-1 times. At the end of this process we get k distinct models and each training example has been used during development of k-1

models. Then finally any new input data is fed into all the k models and the final prediction is the average of the predictions of individual models. As each example in the input dataset has been used for training at least k-1 models out of the k distinct models, the final mean prediction takes into account all the knowledge present in the entire input dataset and thus helps in maximizing the utilization of all the available limited data.

Thus for this research project the available input dataset of 40 datapoints was randomly divided into 4 different disjoint subsets, each consisting of 10 datapoint. Four distinct training and cross validation set combinations were generated using four fold cross validation technique as described above and each training and cross validation set combination was used for developing separate ANN models.

5.11 Network topology and random weight initialization

Another important feature of the ANN model which affects its final performance is the number of hidden layers used and the number of neurons present in each hidden layer of the model. The number of hidden layers and number of neurons present in each hidden layer of the ANN model constitute the topology of the model. For the ANN model developed in this research project, a network topology with two hidden layers was chosen as it has been shown mathematically that such a neural network with two hidden layers and one output layer can simulate any

kind of mathematical functional relationship present between the input and output variables in the training dataset [138]. Thus two hidden layers were selected as that would provide the ANN model with required representational capacity to simulate the complex functional relationship between the thermal and mechanical history of the sample and the final phase distribution which results from it.

Following this the next challenge faced in development of the ANN model was regarding deciding on the optimal number of sigmoidal neurons to be used in each of the two hidden layers. The number of neurons in each of the hidden layer of the ANN model can significantly affects its final performance. With a greater number of neurons in the hidden layer, the neural network can simulate more and more complicated multidimensional mathematical relationships. But on the other hand increasing the number of neurons in the hidden layer also leads to an increase in the complexity of the model and this in turn leads to higher computational expense being required for the training of the model. More importantly, increasing the number of neurons leads to an increase in the number of weights defining the model and this in turn leads to an increase in the dimensions of the hypothesis space in which we are searching for the error minima. Higher dimensional hypothesis space leads to a more complicated error surface, which increases the difficulty of finding an optimal error minima during the training of the model. Thus the number of neurons present in each hidden layer of the neural network significantly influence the difficulty of training the ANN model and also the final

generalization performance of the model [137].

Once the network topology has been fixed, the values of all the weights in the neural networks are randomly initialized before the learning process begins. Those initial values of the weights of the neural network mark the starting point in the hypothesis space from which neural network starts it search for finding the error minima during its training. Different random initialization means that each time the neural network starts from a different point in the hypothesis space and follows a different path during its training. It also means that after the training, neural networks initialized with different random weights might end up at a different points in the hypothesis space even though they were trained using the same data and had the same network topology. Thus the final generalization performance of the ANN model is a direct result of both the network topology and the random initialization of the weights of the model.

This particular characteristic of the ANN model makes it impossible to empirically determine the optimal neural network topology for a given training dataset. Because of the final performance being affected by both network topology and random initialization, it is not possible to isolate the effect of neural network topology on the final performance. Thus trying out different network topologies and comparing their final prediction performance can't be conclusive as there is no way to know whether the final model performance was a result of the particular

network topology or the random weight initializations.

For neural networks, the hypothesis space consists of multiple global and local minimas for the functional relationships that the ANN model is trying to simulate from the data. There is no way of knowing if the error minima obtained after the model training is a global minima or a local minima. The only way to compare the error minimas achieved by two different models after their training is by measuring the performance of the models on the test dataset. However considering that our test dataset is again just a sample from the entire population, even the performance of the models on the test dataset does not give us a conclusive evidence regarding whether the error minima achieved by one model is better than the other. Thus the best approach in this scenario is to develop multiple models using different random initializations and different network topologies and then use all of them to make prediction on any new input data. All the different models generated can be ensembled to form *'a committee of models'* and then each member of the committee contributes to making the final prediction [137].

For any new data, the input values are fed into each individual member of the committee and the final output of the committee is the mean of the output produced by individual members of the committee. Thus this was the approach which was used for the development of the final ANN model and hence the final ANN model was actually a committee formed from individual ANN models.

5.11.1 Number of neurons used in hidden layers

In order to form a committee of ANN models, multiple ANN models with different topology and different random initializations need to be generated. Since there are a total of ten input features as shown in Table 4.2, the minimum number of neurons to be present in each of the individual hidden layer was fixed to be ten to begin with [141]. After that the number of neurons to be present in individual layer were increased in steps of five. Thus the number of neurons present in each individual hidden layer of the feedforward neural network was varied from ten, fifteen to twenty. The maximum number of neurons present in an individual layer was capped at twenty by taking into consideration the computational expense involved along with the proposed rule of thumb of limiting the number of hidden layer neurons to less than double the number of input layer neurons for small datasets [142]. Even by using just three different values for number of neurons present in the two hidden layers, that gave rise to nine different possible neural network topologies which are listed in the Table 5.2 given below.

Each of these nine neural network topologies were trained on all the four different combinations of training & cross-validation dataset obtained through four fold cross validation as described in section 5.10 earlier. Finally for each neural network topology and a particular training & cross validation set combination, five different random initializations were done to account for the effect of different

starting points in the hypothesis space on the final model performance. Thus in the end a total of 180 different ANN models were generated using the input dataset.

Table 5.2: Different neural network topologies used in this research

Network topology	Number of Neurons in Hidden Layer 1	Number of Neurons in Hidden Layer 2
1	10	10
2	10	15
3	10	20
4	15	10
5	15	15
6	15	20
7	20	10
8	20	15
9	20	20

5.12 Final committee of models

All the 180 models generated were ensembled together in order to form the final committee of the models. This committee of the 180 models will be henceforth be

referred to as *'the final ANN model'*. It was this final ANN model which was used for model validation on the independent data in test dataset and for further exploring the functional relationships between the input thermal and mechanical history of the samples and the resulting phase distribution from it.

Any new input data was fed into all the 180 members of the committee and the final output of the committee is the mean of the individual outputs of the members of the committee. The committee also outputted the measured standard deviation in the predictions made by individual members of the committee and this standard deviation was a measure of the confidence with which the committee was making its final prediction for a given thermal and mechanical history input.

5.12.1 Development of the prediction uncertainty bars

For the predictions made by the final ANN model to be reliable, it is necessary to provide uncertainty bars for those predictions. The predictions made by the final ANN model are based on the knowledge that was present in the input dataset which was used for developing the model. Since the input dataset is a sample from the entire population of all possible points in the experimental space, it is not possible for the entire knowledge of the experimental space to be captured by the input dataset. The final ANN model learns this limited knowledge present in the input dataset and then uses that knowledge to make predictions for completely new

data. Since the predictions made by the final ANN model are based on the limited knowledge of the input dataset and not on the complete knowledge present in the entire experimental space, there is going to be an inherent uncertainty present in those predictions. The calculated uncertainty bars help us in quantifying that very inherent uncertainty in the model predictions and thus are of great importance from an engineering reliability and application standpoint.

Each member of the committee ends up at different error minimas in the hypothesis space corresponding to their topology, while they are trying to learn the same functional relationships from the limited knowledge present in the given input dataset. Based on the error minimas where they have finished at the end of their training, each member of the committee makes predictions that moderately vary from the predictions made by other members. Thus a measurement of the standard deviation in the predictions made by different members of the final committee is representative of the uncertainty in the prediction which can be made based of the limited knowledge present in the input dataset. Thus this standard deviation measurement in the predictions made by the committee members was used for developing the uncertainty bars for the predictions made by the final ANN model.

The standard deviation in the predicted value of each phase for a given input value by the committee members is measured and then the uncertainty bar for that phase

volume prediction is calculated using the formula below:

$$Uncertainty\ Bar = \pm 2 \text{ x } Measured\ standard\ deviation \quad (5.22)$$

The factor of two for measured standard deviation was selected as approximately 95% of observations always fall within two standard deviations from the mean. Hence each individual prediction made by the final ANN model will be of the following form:

$$Mean\ Phase\ Volume\ Prediction \pm 2 \text{ x } Standard\ Deviation \quad (5.23)$$

Here by multiplying the measured standard deviation in the prediction with a factor of two, it is expected that the uncertainty bars generated should be able to capture the true output value in their range with a probability of 95%. That is an extremely high probability value and gives us a high degree of reliability in the predictions made by the final ANN model.

In the next chapter the performance of the final ANN model, in making accurate phase distribution predictions based on the input thermal and mechanical history, will be critically analyzed and discussed. Initially, the ANN model's phase distribution prediction performance will be measured on the input dataset which was used for its training and development. Finally the ANN model's phase distribution prediction performance will be validated by comparing its predictions

against the independent experimental data present in the test dataset, which it has never encountered before. The work presented in the next chapter will give a clear idea regarding the reliability and robustness of the final ANN model developed in this chapter.

Chapter 6

Model Analysis and Discussion

6.1 Overview

After the final ANN model had been developed as detailed in the previous chapter, the model's prediction performance on the input dataset was measured and analyzed in detail. Furthermore, the ANN model was also validated by evaluating its performance on independent experimental data present in the test dataset, so that the robustness and reliability of model's future predictions could be measured. This validation of model's performance on completely new and independent experimental data was akin to testing the predictions made by a theoretical model against independent experimental data and that gave an estimate about the generalization capabilities of the model when faced with completely new data. This validation exercise helped in demonstrating the reliability and capability of the ANN model, which established the model's potential for future *computer-aided engineering* (CAE) applications and for further explorations for gaining deeper insights into the functional relationships between thermo-mechanical history and the final resulting phase distribution in boron steel.

6.1.1 A Note on error reporting

The error in the performance of any model, when compared against real world data, can be reported either in terms of *absolute* error or *relative* error. The *absolute* error gives the absolute difference between the predicted value and the *true* value, whereas the *relative* error reports the measured absolute error relative to the size of the prediction. Reporting error in terms of relative error is particularly useful when comparing the quality of two predictions with different units or when the range of predicted values is not fixed, but in most other cases error reporting can be done in terms of absolute error.

In this thesis, the final ANN model prediction error has been reported in terms of absolute error following the convention reported in the literature [143-149]. For this thesis, all the predictions made by the final ANN model have the same units of percentage phase fraction (%) and the range of predicted values is fixed from 0%-100%. For example, if the *true* value of measured phase fraction obtained from the experimental work is 10% and the predicted phase fraction value obtained from the final ANN model is 12% then the absolute error in the prediction is reported as being 2%. Over here the percentage (%) is the unit of the measurement and not the percentage reporting relative error. This convention has been followed throughout this thesis for reporting error and needs to be borne in mind by the reader to avoid any potential confusion.

6.1.2 Significance of prediction uncertainty bars

In this chapter, all the predictions made by the final ANN model have been reported along with their calculated uncertainty bars. The prediction uncertainty bars have been calculated using statistics in such a way that 95% of times the *true* measured value is expected to fall within the range calculated based on uncertainty bars. Another important reason behind using the proposed approach (section 5.12.1) for calculating the uncertainty bar is that it allows the final ANN model to generate customized uncertainty bars for each individual phase value predictions, rather than having a fixed rigid uncertainty bar for the entire model.

Since the final ANN model is making output predictions based on the knowledge that it has learnt from the input dataset, it will be able to make prediction with greater confidence if the new data is similar to the data which was used for its training and development. But at the same time if the final ANN model faces new data which is completely different, then the uncertainty in its prediction will increase. Using this particular approach allows us to capture the localized variations in the confidence of predictions made by the final ANN model in all the different possible regions of experimental space. This approach allows the final model to generate customized uncertainty bars for each prediction based on how confident it is about that prediction; with smaller uncertainty bars signifying the greater confidence of the final model for that particular prediction.

6.2 ANN model performance on input dataset

For measuring the ANN model performance, the thermal and mechanical history data of all the Gleeble samples present in the input dataset was fed into the model and the model's predictions were compared with the actual measured phase distribution values obtained from nanoindentation testing present in the input dataset. This performance measurement was done for all the 40 samples present in the input dataset. For the input data of each sample, three predictions were made by the ANN model corresponding to each of the three possible phases that are found in the final microstructure of boron steel tailor hot stamped parts namely: ferrite, bainite and martensite. Thus corresponding to 40 different samples present in input dataset, the final developed ANN model had made a total of 120 phase fraction value predictions.

6.2.1 Ferrite volume fraction predictions

The comparison of all the predicted ferrite phase fraction values along with the measured ferrite phase fraction values for all the 40 samples in the input dataset is shown in the Figure 6.1. All the measured ferrite phase fraction values have been arranged in ascending order and all the predicted ferrite phase fraction values are shown along with their respective calculated uncertainty bars (calculated as described in section 5.12.1) in the Figure 6.1:

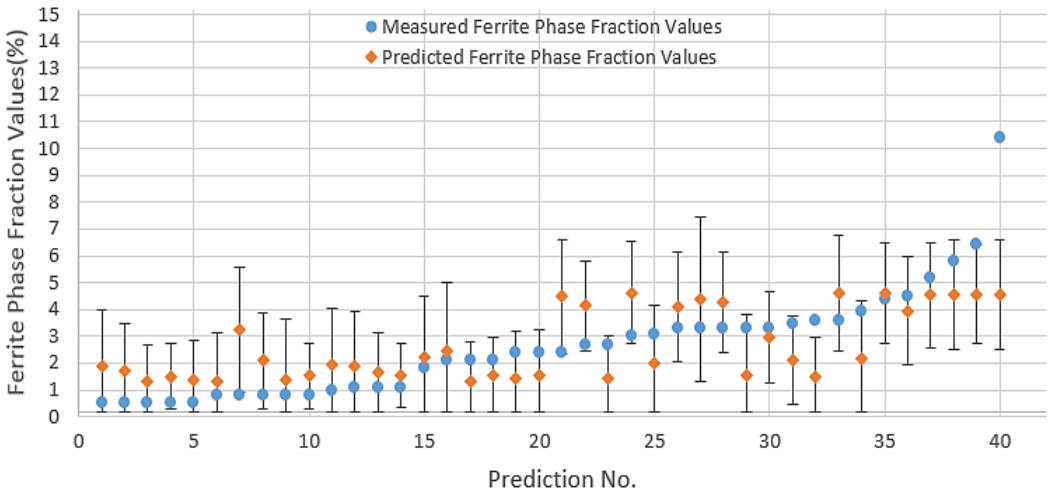

Figure 6.1: ANN model ferrite volume fraction predictions for input dataset

All the 40 ferrite phase fraction predictions made by the ANN model for each sample in the input dataset are presented along with the measured ferrite phase fraction values in the above Figure. The ferrite phase fraction predictions made by the ANN model based on the sample's thermal and mechanical history are in close agreement with the actual measured values obtained by nanoindentation testing. The mean absolute difference in ferrite volume fraction predictions made by the ANN model and the measured values is 1.2%.

In Figure 6.1 along with the individual ferrite predictions made by the ANN model, the uncertainty predictions made by the model are also presented. This uncertainty bars represent the inherent uncertainty present in the prediction made by the ANN model and have been calculated in such a way that 95% of time the true output value is expected to fall within the range defined by them. As can be

seen in Figure 6.1 for 38 predictions out of the total 40 ferrite fraction predictions made by the ANN model, the measured ferrite fraction value falls within the range defined by the uncertainty bar for a given prediction. Thus it can be seen that the uncertainty bars predicted by the model are quite robust and are able to capture the measured value 95% of time as expected.

Table 6.1: Measured and predicted ferrite phase volume fraction values when measured values fall outside the calculated uncertainty bars (input set)

Measured Ferrite Phase Volume Fraction	Predicted Ferrite Phase Volume Fraction	Absolute Difference between measured and predicted values
4%	1%	3%
10%	5%	5%

For the two instances where the uncertainty bars of the prediction made by the model are not able to capture the measured value, the absolute difference between the predicted and the measured values are given in the Table 6.1. As can be seen, in case of ferrite phase fraction prediction the absolute difference between the predicted and measured values is quite low. As discussed in the section 4.4 in chapter 4, the uncertainty in the phase volume fraction measurements obtained by nanoindentation testing method is about 12%. Since the absolute difference between the measured and the predicted values was less than that, no further investigation was done.

6.2.2 Bainite volume fraction predictions

Similarly the predictions made by the ANN model for the bainite content in the final microstructure of the 40 samples present in the input dataset are given in Figure 6.2 below, along with the measured values which are arranged in ascending order. The bainite phase fraction predictions were made by using the thermal and mechanical history of the sample as input to the ANN model.

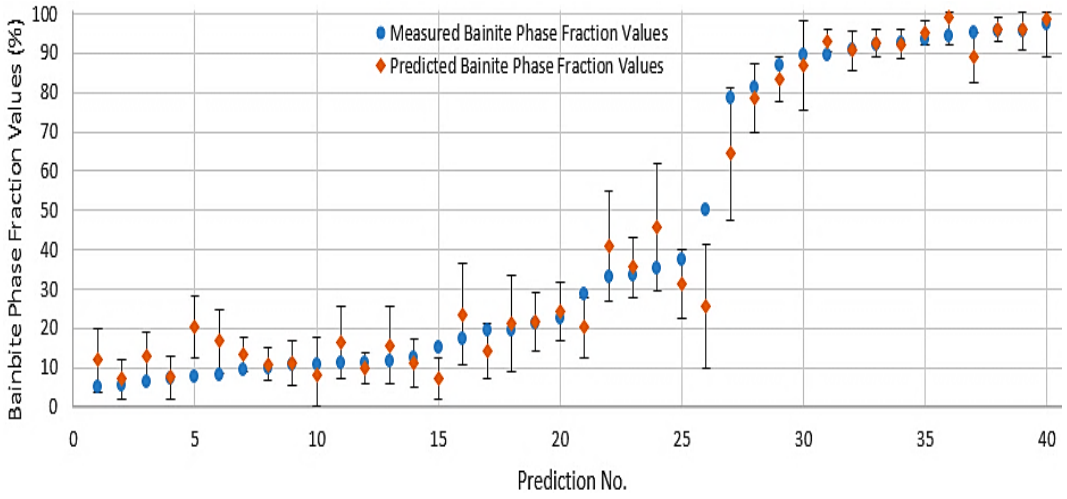

Figure 6.2: ANN model bainite volume fraction predictions for input dataset

As can be observed from the Figure 6.2, for most of the predictions there is a excellent agreement between the bainite volume fractions predicted by the ANN model and the measured values obtained from the nanoindentation testing. The average absolute difference between the ANN model bainite volume fraction predictions and the measured values for the samples in the input dataset is 5%.

For 37 out of 40 predictions made by the ANN model, the measured values of the bainite phase fractions in the microstructure falls within the range defined by the uncertainty bars predicted by the ANN model. The three measured bainite phase fraction values, which the calculated uncertainty bars were unable to capture are presented in the Table 6.2 given below:

Table 6.2: Measured and predicted bainite phase volume fraction values when measured values fall outside the calculated uncertainty bars (input set)

Measured Bainite Phase Volume Fraction	Predicted Bainite Phase Volume Fraction	Absolute Difference between measured and predicted values
15%	7%	8%
8%	20%	12%
50%	25%	25%

The absolute difference for only one out of the three samples presented in that Table is greater than 12%, which is the inherent uncertainty present in phase fraction measurements obtained from nanoindentation testing as discussed in section 4.4 of Chapter 4. For this one case the absolute difference between the measured bainite volume fraction value and the predicted bainite volume fraction value is 25%. This is a significant amount of difference where the ANN model ends up under predicting the bainite content of the final microstructure by almost 25%. Thus further investigations were done using the microstructural images of that sample obtained from metallography and microstructural analysis.

In order to get a better idea about the phase distribution in that particular sample, three microstructural images obtained from that sample are given in the Figure 6.3. All the three images were taken from different locations along the sample and thus give us a reliable qualitative insight into the different phases present in the final microstructure of that particular sample.

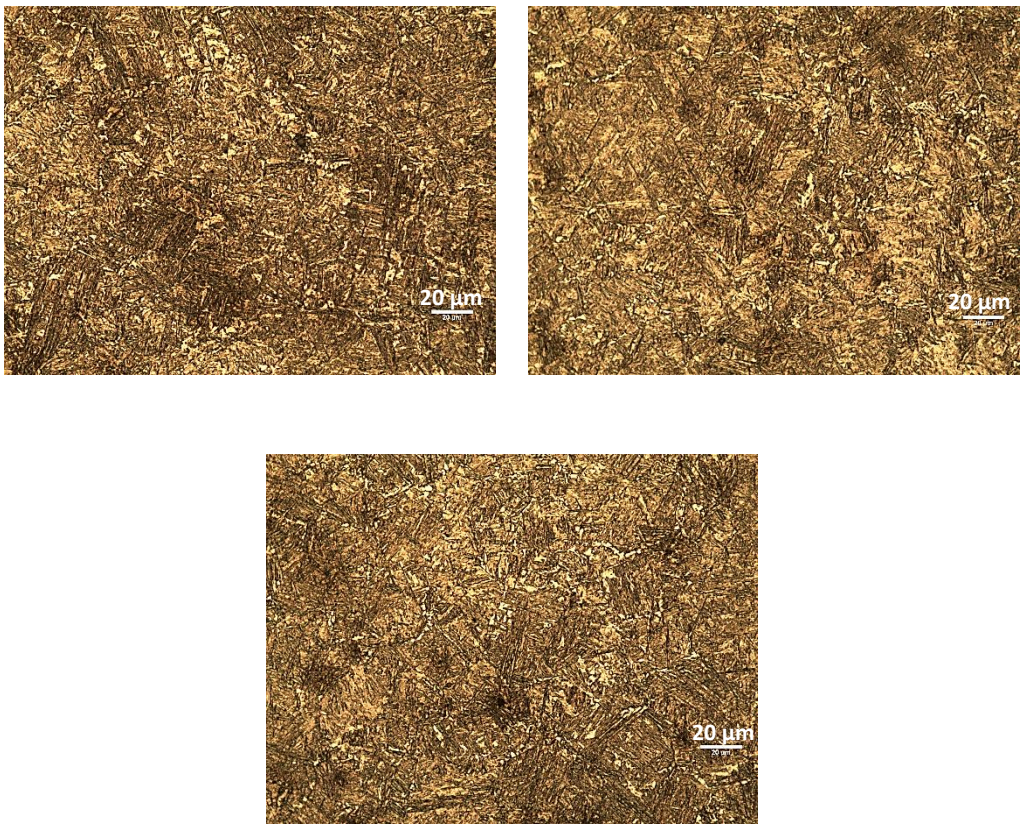

Figure 6.3: Microstructure images of the sample for which predicted and measured bainite volume fraction differ by 25% (input set)

In the microstructures, it can be observed that the amount of acicular lath martensite is present in significantly greater amount and thus the microstructure

can be classified as martensitic along with some volume fraction of bainite present in it. Now the measured value of bainite phase fraction obtained from nanoindentation testing is about 50% with an uncertainty of 12%. Thus according to the nanoindentation testing there is a 5% probability of the bainite content of the microstructure being less than 38%. As can be seen from these microstructures obtained from metallographic analysis, the martensite content of the microstructure is definitely greater than 50%. Thus based on these micrographs it can be concluded that this bainite phase volume fraction prediction made by the ANN model is a reasonable prediction and approximately reflects the apparent distribution observed in sample microstructure using microscopy.

6.2.3 Martensite volume fraction prediction

Finally the martensite phase volume fraction predictions made by the ANN model for the 40 samples in the input dataset are compared with the measured phase volume fraction values obtained from nanoindentation testing in Figure 6.4 given next. As in earlier figures, all the measured martensite phase fraction values are presented in an ascending order and the calculated uncertainty bars for each prediction from the ANN model are presented in the Figure.

As can be seen from the Figure, the martensite predictions made by the ANN model are in excellent agreement with the measured values for the samples in

input dataset. The average absolute difference between the martensite phase volume fraction predictions made by the ANN model and the measured values for the samples in the input dataset is 5%.

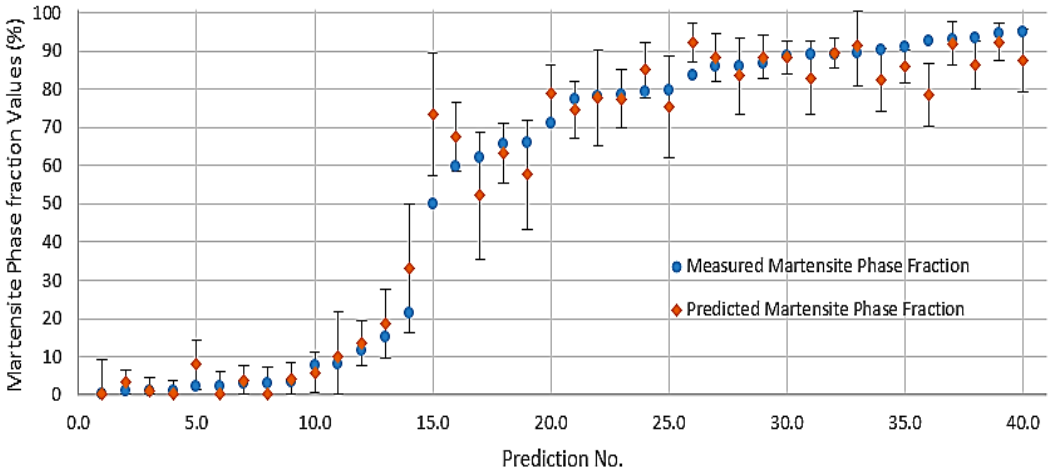

Figure 6.4: ANN model martensite volume fraction predictions for input dataset

Table 6.3: Measured and predicted martensite phase volume fraction values when measured values fall outside the calculated uncertainty bars (input set)

Measured Martensite Phase Volume Fraction	Predicted Martensite Phase Volume Fraction	Absolute Difference between measured and predicted values
49%	73%	24%
83%	92%	9%
92%	78%	14%

Also as seen in the Figure, for martensite predictions 37 out of 40 measured martensite phase fraction values fall within the uncertainty bars predicted by the ANN model along with each martensite prediction. The remaining 3 measured

martensite phase fraction values which fall outside the range defined by the uncertainty bars, are presented in the Table 6.3 along with their corresponding predicted values and absolute differences. As can be seen in the Table 6.3, for 2 out of 3 observations the absolute difference between the martensite volume fractions predicted by the ANN model and the measured values is greater than 12% (uncertainty in phase fraction measurements obtained from nanoindentation testing). However, the first observation in Table 6.3 where the martensite content was over predicted by 24% corresponds to the same sample for which the ANN model had under predicted the bainite content by 25% in the earlier section. As observed in the micrographs obtained from that sample in Figure 6.3, the microstructure had a significantly high martensite content. Thus the over prediction of the martensite content by the ANN model for that particular sample is in line with what was observed in the microstructures of that sample.

For the last observation in the Table, where the absolute difference between predicted and measured martensite volume fraction values is 14%, further investigation was performed. In the Figure 6.5, three microstructural images of that sample obtained from three different locations along the sample are given. As can be seen in the micrographs, the microstructure consists mainly of needle like martensitic structure with very small amounts of bainite which supports the high martensite phase fraction value obtained from nano-indentation testing.

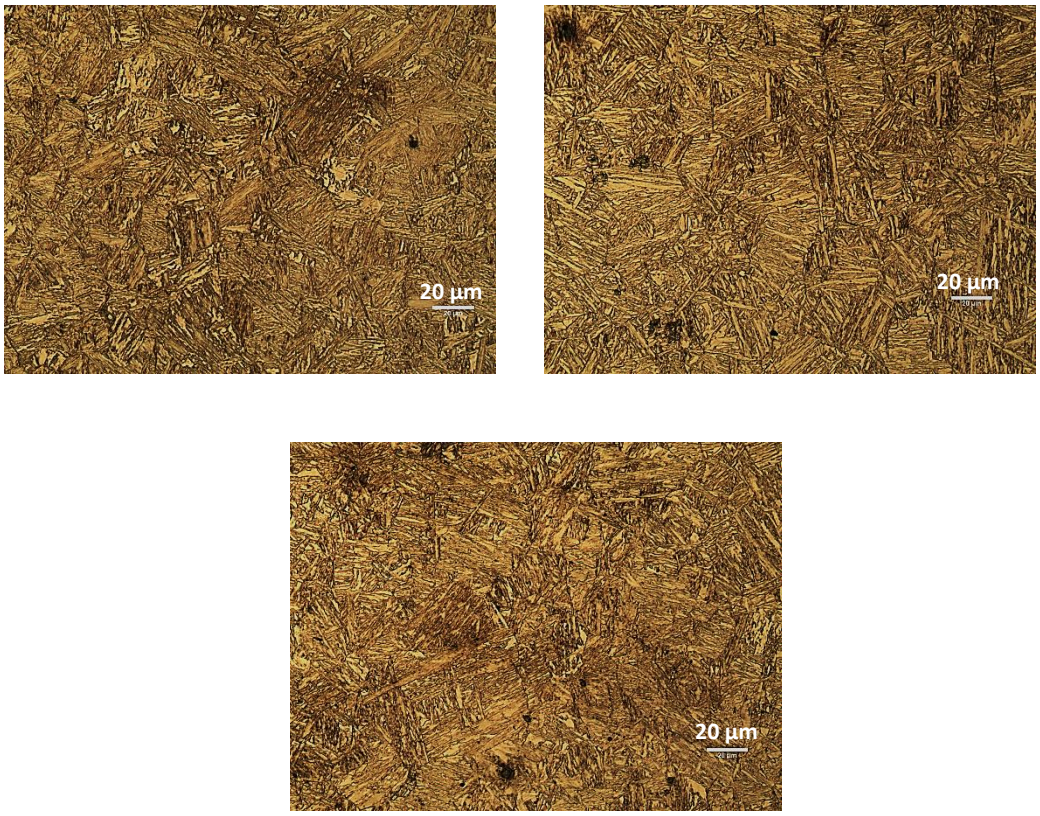

Figure 6.5: Microstructure images of the sample for which predicted and measured martensite volume fraction differ by 14% (input set)

The prediction made by the ANN model for the martensite content of this sample is 78%, which in spite of predicting a high martensite content does not completely capture the overwhelmingly dominant nature of the martensite in this microstructure. However even in such an extreme case, the significantly high martensite content prediction by the ANN model based on the sample's thermal and mechanical history is reflective of the robustness of the model and its success in capturing the underlying functional relationships between the input processing parameters and the phase distribution in the final microstructure.

6.2.4 RMS measurement on the input dataset

After the model's prediction performance had been investigated in detail for each of the individual phases, the Root Mean Square (RMS) error was calculated for measuring the ANN model's overall performance on the input dataset. The RMS error gives us an idea about the average error made by the ANN model while making a phase volume fraction prediction based on sample's thermal and mechanical history for the samples in the input dataset. The RMS error is calculated over all the predictions and is thus independent of the type of the phase that the model was trying to predict. In order to measure the RMS performance error, the individual differences between the predicted phase volume fractions and the measured values were calculated for all the 120 predictions made by the final ANN model (corresponding to 40 samples in the input dataset). After that the individual differences were squared and their mean was taken. Finally the square root of this mean was calculated to get the RMS prediction performance error of the model over the input dataset.

The RMS prediction error measured for the ANN model over the entire input dataset was calculated to be 5.4% phase volume fraction. Thus for the 120 phase volume fraction predictions made by the ANN model over the entire input dataset, the average error in the model prediction was found to be only 5.4%. This is an excellent performance by the model and any phase volume fraction prediction whose value differs from the measured volume fraction value by less than 5% can

be considered to be highly accurate. But since the RMS error calculation is an average, there will be phase volume fraction predictions which differ from the measured values by more than 5% and such predictions were relatively classified as being "*less accurate"* compared to the measured volume fraction values obtained from nanoindentation testing.

From a total of 120 predictions made by the ANN model, there were only 31 predictions which differed from the measured values by more than 5%. Thus only 26% of the total predictions (31 out of 120) made by the ANN model over the entire input dataset were classified as "less accurate" compared to the measured values, with a threshold of 5% absolute difference in volume fraction being considered as less accurate. The comparison between such predicted "less accurate" phase volume fraction values and the measured values in the input dataset is presented in the Figure 6.6. Thus in the Figure 6.6 only those 31 predictions, which are relatively speaking the least accurate predictions made by the model on the input dataset, have been presented.

As can be seen from the Figure 6.6, overall there is a good agreement even between those 31 relatively not so accurate predictions made by the ANN model and the measured values in the input dataset. There are only two predicted phase volume fractions which differ from the measured values by more than 20% and both of them have been highlighted in red as "predictions differing by the greatest

amount" in the Figure 6.6 given below. All the measured values presented in the graph in Figure 6.6 have been arranged in the ascending order.

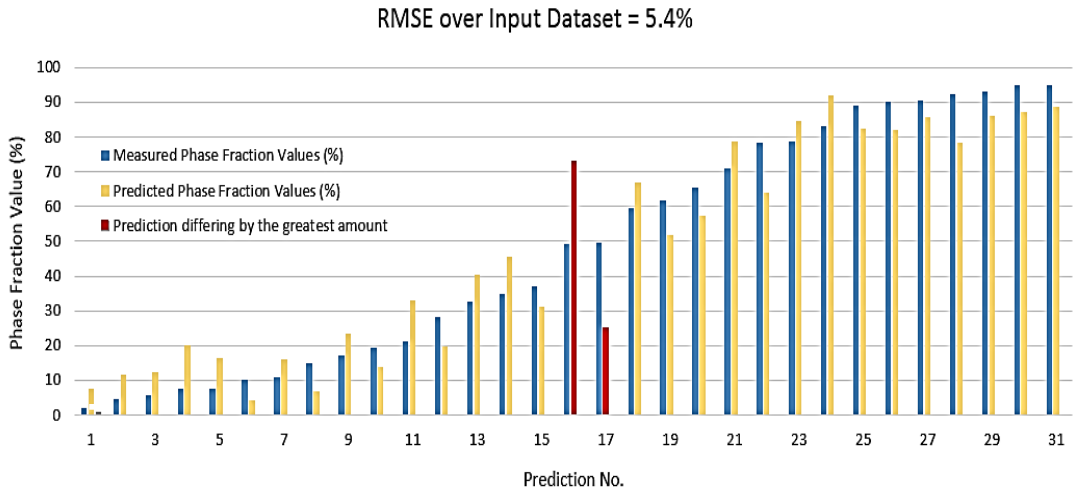

Figure 6.6: Predicted phase fraction values which differ from measured phase fraction values by more than 5% in input dataset

The two ANN model predictions which appear to have the greatest difference from the measured values in the Figure 6.6 (prediction no.16 and 17), correspond to the same sample for which the ANN model had under predicted the bainite content by 25% and over predicted the martensite content by 24% in the earlier section. As it was observed in the microstructural images obtained from that sample in Figure 6.3, the microstructure was indeed martensitic with some fraction of bainite present in it. And there is a 5% probability that the measured volume fraction values obtained from nanoindentation testing are off by more than 12%. Thus even those two predictions made by the ANN model reflect the general distribution

observed in the microstructure of that sample and are not wrong predictions.

Overall the ANN model performance over the input dataset was observed to be excellent and the predictions made by the ANN model to be robust and reliable. This encouraging performance of the ANN model over the input dataset is reflective of its capabilities and suggests that it has indeed managed to learn the functional relationships between the thermal and mechanical history of the sample and the final resulting phase distribution in the sample.

However a key point that needs to be borne in mind is that all the data in the input dataset was the same data which was used for training and developing the ANN model. A good analogy for explaining the significance of measuring the ANN model's performance on the input dataset would be the significance of measuring how well a line fits the datapoints in linear regression. Just as a good fit indicates that the predicted line successfully captures the linear nature of the relationship present in the data, so does the model's good performance on the input dataset indicate that it has successfully managed to capture the functional relationships present in the data. But this exercise does not give us any idea about how model will perform when it faces new data. Thus in order to measure the generalization capabilities of the model and its true robustness & reliability, a further validation of the model is required by measuring its performance on completely new independent data which it has never encountered before.

6.3 ANN model validation

Having established the excellent performance of the ANN model over the input dataset, the next step was to investigate how well the ANN model could perform using that learnt knowledge when faced with completely new input data. The best way to validate any model is to perform experiments and then compare the model's prediction with what was observed in the physical world through those experiments. This gives the best estimate about the trustworthiness of the model and helps in deciding how reliable the predictions made by model will be. Such a validation exercise is akin to developing a theoretical model and then measuring its predictions against experimental data in order to confirm whether the theoretical model is valid and whether it is able to accurately represent the physical phenomena that it is trying to model.

A similar exercise was carried out for the validation of the final ANN model. Data generated from 10 independent Gleeble experiments was used for validating the final ANN model. As discussed in section 5.6 in the last chapter, from the original ANN dataset a separate test dataset was created for this very purpose. The data in this test dataset came from 10 Gleeble tests and had never been exposed to the ANN model before. Thus data from these 10 Gleeble tests represents completely unknown data for the model and how well the ANN model performs on this test dataset will give us an estimate about the model's generalization capability.

6.4 ANN model's performance on test dataset

In order to measure the ANN model's performance on the test dataset, the thermal and mechanical history data from the samples in the test dataset was used as input for the ANN model. Based on that input, the ANN model predicted the final phase distribution in the microstructure for all those Gleeble test samples. The phase volume fraction values predicted by the ANN model for each of the samples were compared with the actual phase volume fraction values obtained from nanoindentation testing for the validation of the model.

6.4.1 Ferrite volume fraction prediction

The results for the ANN model's prediction for the ferrite volume fraction content in the final microstructure of all the 10 samples are presented in the Figure 6.7 given below along with their uncertainty bars and the measured values. The measured values have been arranged in an ascending order in the Figure 6.7.

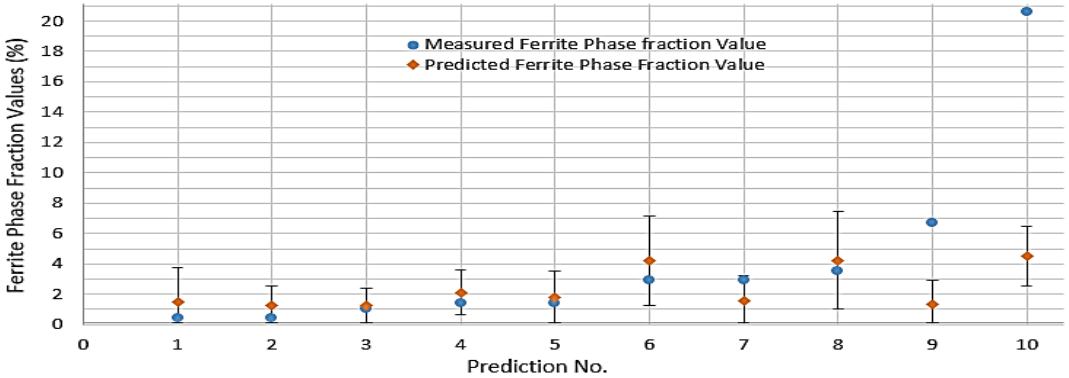

Figure 6.7: ANN model ferrite volume fraction predictions for test dataset

As can be seen from the Figure above, for 8 out of 10 samples there is excellent agreement between the ferrite value predicted by the ANN model and the measured value obtained from nanoindentation testing. The average absolute difference between the predicted and the measured ferrite volume fraction values for the samples in the test dataset is 3%. The two measured values which fall outside the uncertainty bars predicted by the model are presented in the Table below along with their predicted values and their absolute differences:

Table 6.4: Measured and predicted ferrite phase volume fraction values when measured values fall outside the calculated uncertainty bars (test set)

Measured Ferrite Phase Volume Fraction	Predicted Ferrite Phase Volume Fraction	Absolute Difference between measured and predicted values
7%	1%	6%
21%	4%	17%

The difference between the predicted value and the measured value for the second sample in the Table 6.4 is significant as it is greater than the 12% uncertainty, which is inherent in the phase volume fraction measurement obtained from nanoindentation testing (section 4.4). Thus in order to investigate this difference further, the microstructural images obtained from that particular sample were analyzed. Three microstructural images from different locations of that particular sample obtained using metallography are shown in Figure 6.8 given below.

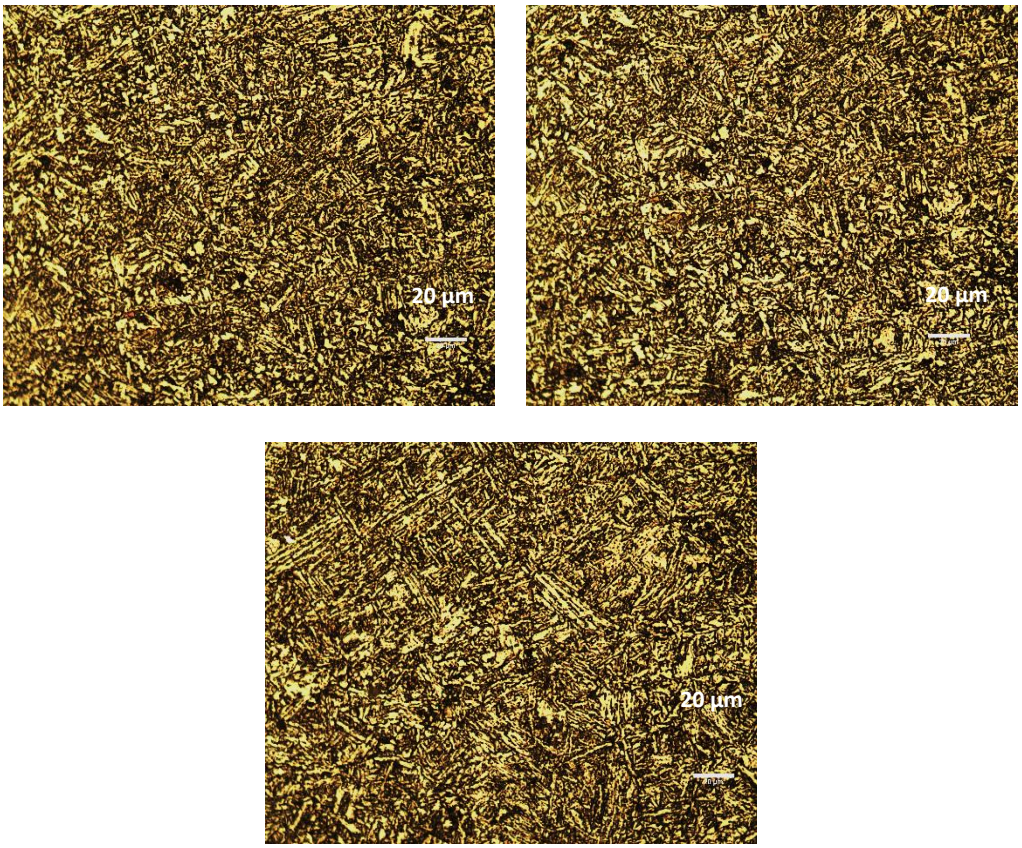

Figure 6.8: Microstructure images of the sample for which predicted and measured ferrite volume fraction differ by 17% (test set)

As can be seen from the microstructural images, the microstructure mainly consists of fine non-lamellar bainite with a small fraction of granular ferrite. From the images the percentage of the ferrite in the microstructure appears to be quite a bit lower than the 21% as obtained from nanoindentation testing. Thus the ferrite content prediction made by the ANN model for that sample, in spite of being on the lower side, manages to captures the low ferritic nature of the microstructure.

6.4.2 Bainite volume fraction prediction

The predictions for bainite phase volume fractions made by the ANN model for the samples in test data based on their thermal and mechanical history are given in Figure 6.9 below. Along with them are plotted the measured values of bainite fraction for each sample, which have been arranged in the ascending order in the Figure. As can be seen from the Figure the bainite phase fraction predictions made by the ANN model agree well with the measured values. The average absolute difference between the predicted and measured bainite volume fraction values for the samples in test dataset was found to be 7%.

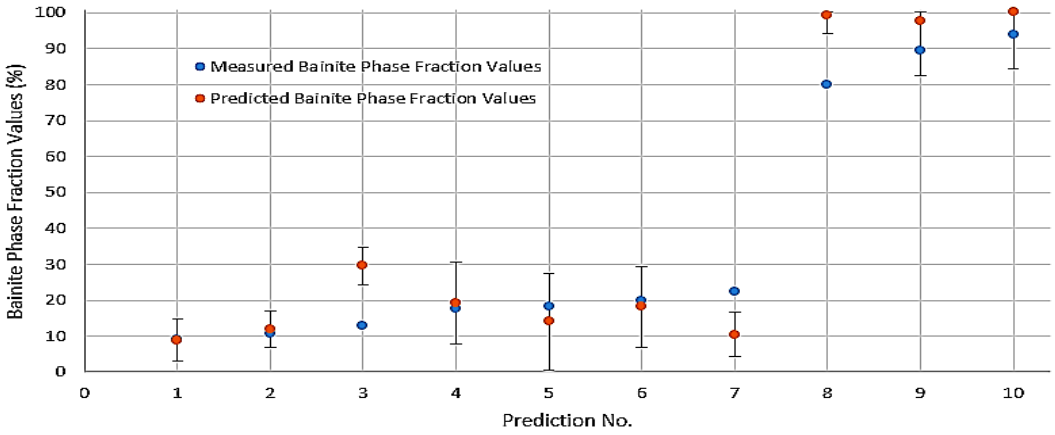

Figure 6.9: ANN model bainite volume fraction predictions for test dataset

For 7 out of the 10 samples, the measured bainite phase fraction values fall within the range defined by uncertainty bars for each predictions. The remaining 3 measured bainite volume fraction values which lie outside the uncertainty bars are given in the Table 6.5 below along with their predicted values.

Table 6.5: Measured and predicted bainite phase volume fraction values when measured values fall outside the calculated uncertainty bars (test set)

Measured Bainite Phase Volume Fraction	Predicted Bainite Phase Volume Fraction	Absolute Difference between measured and predicted values
12%	29%	17%
22%	10%	12%
79%	99%	20%

Now here for 2 out of 3 samples, absolute difference between the measured and predicted values is greater than 12% (inherent uncertainty in measurements obtained from nanoindentation testing – section 4.4). The sample for which the absolute difference between the measured and predicted bainite phase volume fraction values is 20%, it is the same sample for which the absolute difference for ferrite phase volume fraction prediction was found to be 17% in the earlier section. The microstructural images from that sample were presented and analyzed in Figure 6.8 earlier. From that it was established that the microstructure is mostly bainitic with some small fraction of ferrite in it. So although the ANN model over predicts the bainite content of microstructure from 79% to 99%, it successfully captures the dominant nature of bainite in the microstructure. Thus overall it is a reasonable prediction and does not differ significantly from what has been observed in the microstructural images from the sample.

The sample for which the model over predicts the bainite content by 17% was

further investigated to establish the validity of the prediction. Three microstructural images from that sample are presented in Figure 6.10 below.

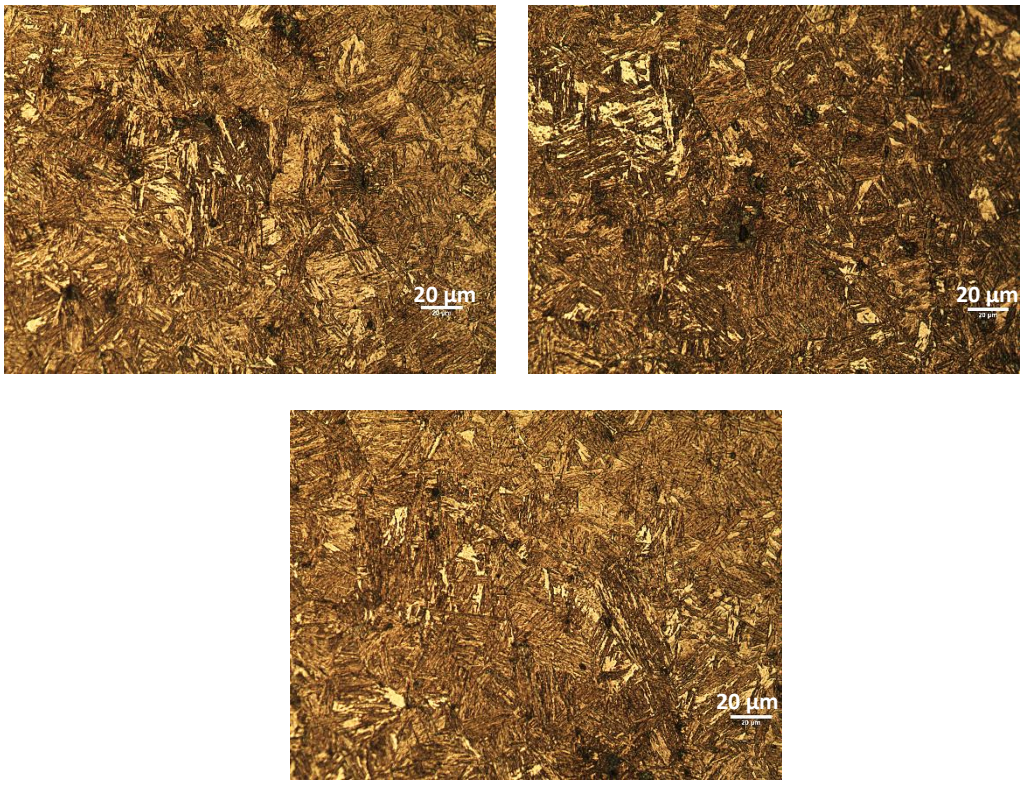

Figure 6.10: Microstructure images of the sample for which predicted and measured bainite volume fraction differ by 17% (test set)

As can be seen from the Figure the microstructure is mainly martensitic, though it has also got some bainite present in it. For the same sample the martensite content predicted by the ANN model was 69%. Thus in this case the ANN model does end up over predicting the final bainite content and not completely capturing the dominant martensitic nature of the microstructure. But still the phase distribution

prediction (69% martensite, 29% bainite) made by the ANN model was not completely off the mark and manages to capture the general trend in the distribution of phase in the microstructure.

6.4.3 Martensite volume fraction prediction

Finally the martensite phase fractions predicted by the ANN model for the samples in the test dataset were compared with the actual measured martensite phase fraction volume fraction values for those samples. The comparison between the measured and the predicted martensite values is shown in the Figure 6.11 below, in which all the measured martensite values have been placed in increasing order.

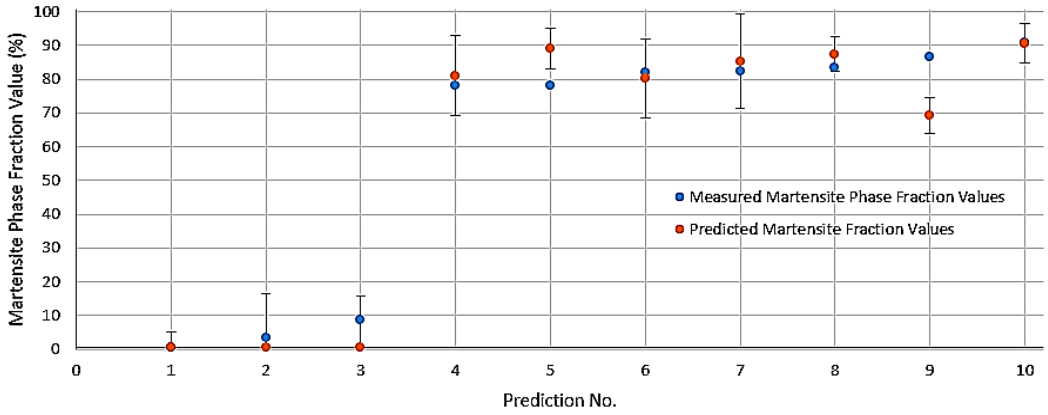

Figure 6.11: ANN model martensite volume fraction predictions for test dataset

It can be seen from the Figure that the martensite volume fraction values predicted by the ANN model match well with the observed values obtained from nanoindentation testing. The predictions made by the ANN model are generally

robust and the average absolute difference between the predicted and measured martensite volume fraction values is 6% for samples in test dataset. For martensite volume fraction predictions made by the model, 8 out of 10 measured values fall within the range defined by the uncertainty bars around the predicted values. The two samples for which the measured values lie outside that range, both the measured and predicted martensite volume fraction values along with their absolute difference have been presented in Table 6.6 below:

Table 6.6: Measured and predicted martensite phase volume fraction values when measured values fall outside the calculated uncertainty bars (test set)

Measured Martensite Phase Volume Fraction	Predicted Martensite Phase Volume Fraction	Absolute Difference between measured and predicted values
78%	89%	11%
86%	69%	17%

Now out of these two samples, for one sample the calculated average absolute difference between the predicted value and the measured value is 11%, which is less than 12% uncertainty that is expected in a phase fraction measurement obtained using nanoindentation testing (section 4.4). Thus no further investigation was done for that prediction. The other sample for which the ANN model under predicts the martensite content of the microstructure by 17%, it is the same sample for which the ANN model had previously over predicted the bainite content by 17% in the earlier section. The microstructural images from that sample have been

presented in Figure 6.10 and as can be seen it is a dominantly martensitic microstructure with some fraction of bainite in it. Thus for that sample the ANN model does end up under predicting the martensite volume fraction and over predicting the bainite volume fraction of the microstructure.

However the point to be borne in mind is that the degree of under prediction of martensite content and over prediction of bainite content as compared with the measured values is not severe. Both martensite and bainite volume fraction predictions are off by approximately 17% as compared with the measured values. The severity of that difference is further reduced, when the uncertainty bars for each of those predictions are taken into consideration. Overall for 9 out of 10 samples in the test dataset, the martensite content predicted by the ANN model is in good agreement with the measured values and for the one remaining sample the ANN model manages to reflect the general phase distribution trend in the microstructure of that particular sample.

6.4.4 RMS measurement on test dataset

In order to further validate the ANN model and get the overall picture of how well the final model performed on the samples in the test dataset, the Root Mean Square (RMS) prediction performance error of the model was calculated on the test dataset. For the RMS error calculations, all the 30 phase fraction predictions

made by the ANN model over the test dataset were used along with the measured phase fraction values present in the test dataset. The RMS performance prediction error for the model was calculated as described in the earlier section on RMS measurement for the input dataset.

The RMS prediction error measured for the ANN model over the entire test dataset was calculated to be 7.7% phase volume fraction. Thus for the 30 phase volume fraction predictions made by the ANN model over the entire test dataset, the average error in the model prediction was found to be 7.7%. This is again an excellent performance by the model and as before any phase volume fraction prediction whose value differs from the measured volume fraction value by less than 5% was considered to be highly accurate. Those phase volume fraction predictions which differed from the measured values by more than 5% were again relatively classified as being "*less accurate"*.

From a total of 30 predictions made by the ANN model for the test dataset, there were only 10 predictions which differed from the measured values by more than 5%. Thus only 33% of the total predictions (10 out of 30) made by the ANN model over the entire input dataset were classified as "less accurate" compared to the measured values, with a threshold of 5% absolute difference in volume fraction being considered as less accurate. The comparison between such predicted "less accurate" phase volume fraction values and the measured values in the input

dataset is presented in the Figure 6.12. Thus in the Figure 6.12 only those 10 predictions, which are relatively speaking the least accurate predictions made by the model on the test dataset, have been presented.

As can be seen from the Figure 6.12, overall there is a good agreement even between those 10 relatively not so accurate predictions made by the ANN model and the measured values in the test dataset. The two predicted phase volume fractions which differ from the measured values by the greatest amount have been highlighted in red as "predictions differing by the greatest amount" in the Figure 6.12 given below. All the measured values presented in the graph in Figure 6.12 have been arranged in the ascending order.

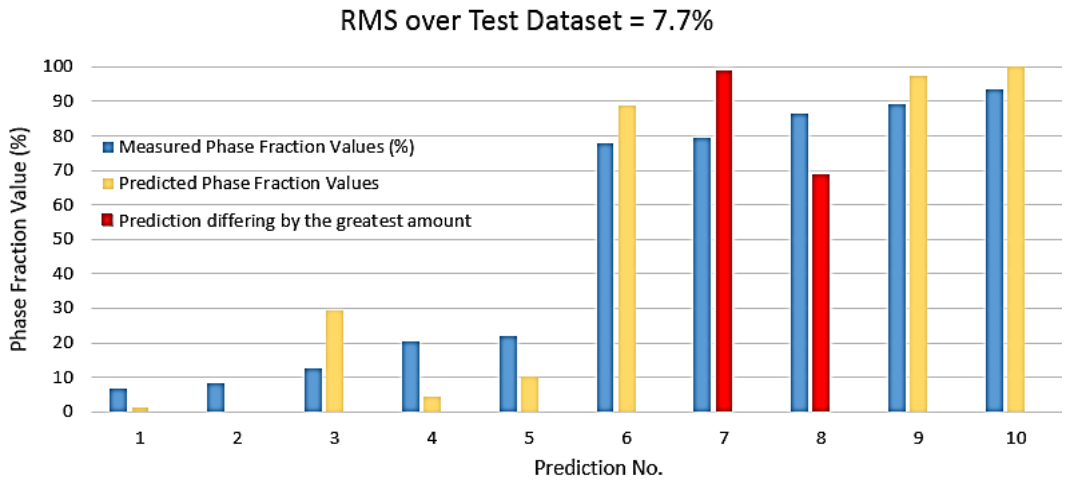

Figure 6.12: Predicted phase fraction values which differ from measured phase fraction values by more than 5% in the test dataset

The two predictions which vary the greatest from measured values have been marked using red in the Figure 6.12. Both these predictions correspond to the two

different samples; for one of which the model had over predicted the bainite content by 20% and for the other model had under predicted the martensite content by 17%. The microstructural images from both the samples are shown in Figure 6.8 and Figure 6.10 respectively. From the qualitative analysis of those microstructural images in the earlier section, both the predictions were found to reflect the general phase distribution trends in the microstructures of the corresponding samples and hence were deemed to be satisfactory.

The RMS prediction performance error for the ANN model was found to be 7.7% over the 30 predictions made by the model on the test dataset. Thus on average a prediction made by the ANN model when faced with completely new data can be expected to differ from the measured value by approximately 7.7%, irrespective of the phase that the model is predicting. This RMS error measurement of the ANN model is reflective of its robust performance in predicting final phase distribution even when faced with completely new and independent input data.

Based on the observation of the prediction performance of the ANN model on the samples in the test dataset, it can be concluded that the developed ANN model is reliable and generalizes well when predicting the final phase distribution in the microstructure of the sample based on its thermal and mechanical history. This good performance of the ANN model over the independent test dataset validated the ANN model and confirmed that the final model had indeed successfully learnt

the general functional relationships which govern the final phase distributions in the microstructures of tailor hot stamped parts based on the thermal and mechanical history experienced by them during their processing.

6.4.5 Concluding remarks on the performance of ANN model

In the earlier sections, the final ANN model's prediction performance was rigorously analyzed over both the input dataset and the test dataset. While the final ANN model gave an excellent performance over both the sets of data, the model's prediction performance deteriorated slightly over the test dataset as compared to its performance over the input dataset. The RMS prediction performance error calculated for the ANN model over the input dataset was 5.4% as compared to the 7.7% when measured over the test dataset. Similarly the ANN model was able to make 74% of *highly accurate* predictions for the input dataset (predicted phase volume fractions whose absolute values differed from measured phase volume fraction values by less than 5%) as compared to 67% *highly accurate* predictions over test dataset containing the new independent data for model validation. Both of these summary metrics point towards the slight deterioration of the final ANN model's performance when measured over the test dataset as compared to its performance over the input dataset.

This small amount of deterioration in the model's performance over test dataset was expected as the model was facing the data in the test dataset for the first time.

It was completely unknown data for the model, while the data in the input set was the same data which was used for training and developing the final ANN model. Thus the model had seen the data in the input set before and had used that data for its learning. So the final ANN model was expected to perform significantly better over the input dataset, especially compared to the unknown data in the test set.

However the excellent performance of the ANN model over test dataset and only a small actual deterioration in its performance against the expectation of a much greater deterioration, offered direct evidence of the robustness and reliability of the ANN model. It offered hard evidence of ANN model's actual generalization capabilities and confirmed that the ANN model had indeed learnt the general functional relationships between thermo-mechanical history and final resulting phase distributions in boron steel quite well. At the same time it demonstrated that the developed final ANN model had the potential to be used for *computer aided engineering* applications in tailored hot stamping in future for producing functionally optimized components for maximum weight reduction and .

6.5 Potential application of the ANN model: A case study

The final ANN model developed in this work was highly robust and reliable. Such a model has the potential to be used for design and development of tailor hot stamped components, which can significantly improve the final vehicle

performance. In tailored hot stamping, the die temperature determines the localized thermal history of different regions in the final hot stamped part. Gaining a better understanding of the effect of interaction of die temperature parameter with deformation amount parameter on the final phase distribution is of critical importance for manufacturing the desired fully optimized automotive components. Thus the developed ANN model was investigated further to study the effect of varying the die temperature at fixed deformation amounts on the final resulting phase distribution in the formed parts.

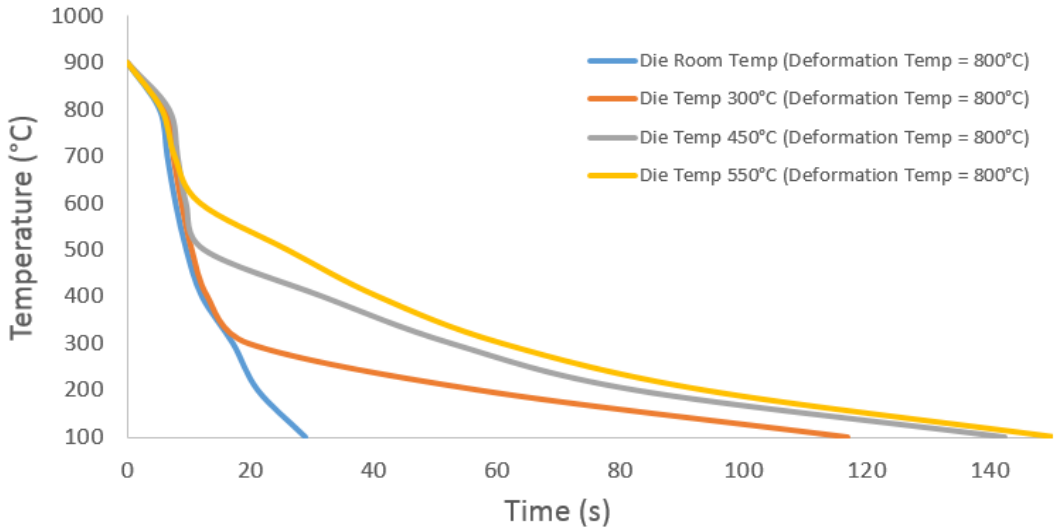

Figure 6.13: Input thermal histories corresponding to 4 different die temperatures

For the investigation, the developed ANN model was fed with the thermal histories corresponding to 4 different die temperatures for 3 different deformation amounts (low, medium and high) while keeping the deformation temperature fixed at 800°C. The thermal histories corresponding to the 4 different die temperatures

(with deformation temperature of 800°C), which were used as input for this investigation are shown in Figure 6.13. The final resulting phase volume fraction predictions made by the ANN model for those four input thermal histories and three different deformation amounts (low, medium and high) at fixed deformation temperature (800°C) are given in Figure 6.14, Figure 6.15 and Figure 6.16.

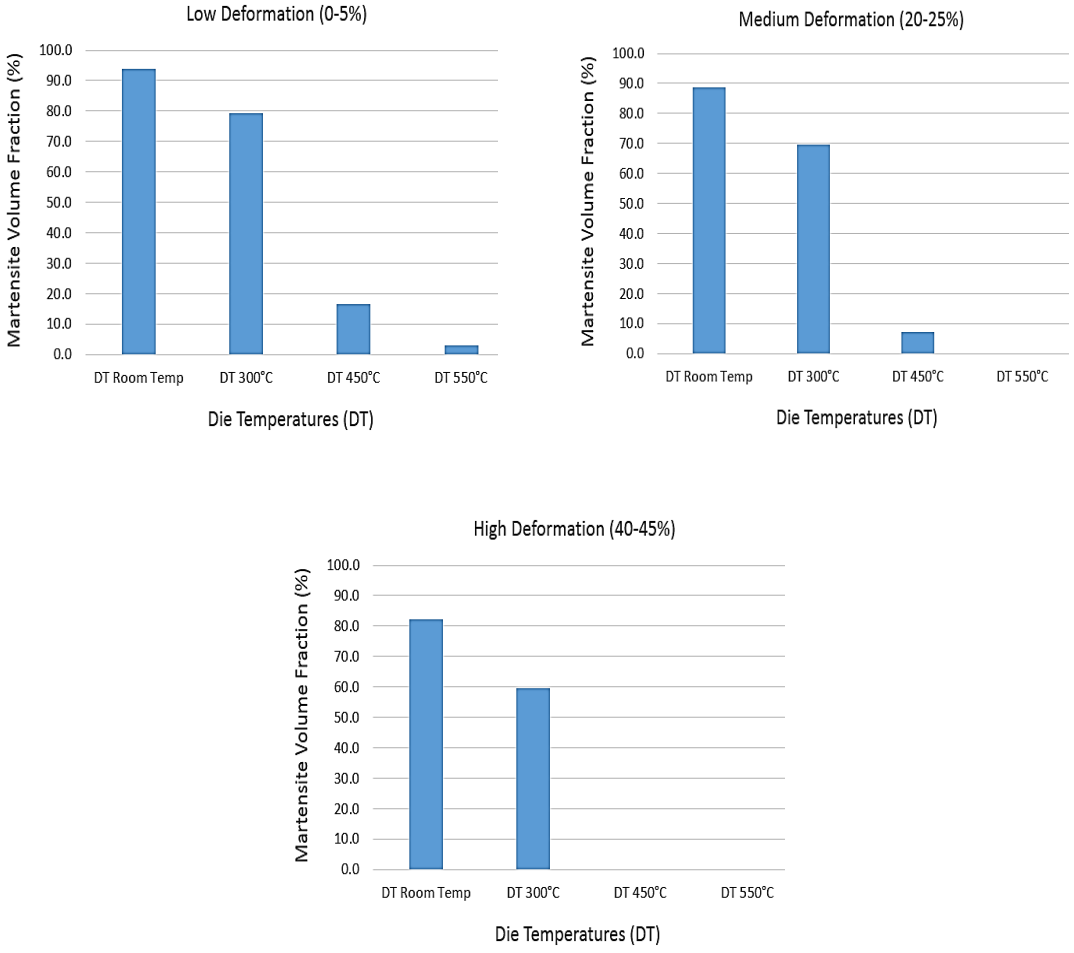

Figure 6.14: Martensite phase volume fractions (%) predicted by the ANN model for different die temperature–deformation amounts (Deformation temp of 800°C)

As can be seen in the Figure 6.14, the martensite content in the final microstructure decreases with increasing die temperatures irrespective of the amount of deformation. This is to be expected as higher die temperatures lead to slower cooling rates and that leads to a greater amount of time being spent by the boron steel in the bainitic region, which leads to lesser amount of austenite being available for martensitic transformations when it hits the martensite start temperature. For medium and high deformation amounts, almost negligible martensite can be expected to be formed at die temperatures of 450°C and 550°C. Also the rate of decrease in the martensite volume fraction with increasing die temperature is highest for medium and high deformation amounts. At low deformation amounts it is only the slow cooling rate which hinders the martensite formation in higher die temperatures, but at higher deformation amounts the mechanical stabilization of austenite effect combines with the slow cooling rates to even further decrease the martensite content of the final microstructure in the tailor hot stamped boron steel component [52, 83].

The different bainite volume fractions predicted by the ANN model for the corresponding die temperatures at given deformation amounts (low, medium and high) and fixed deformation temperature (800°C) are given in Figure 6.15. As can be seen from the Figure, the bainite content in the final microstructure increases with increasing die temperature irrespective of the deformation amount.

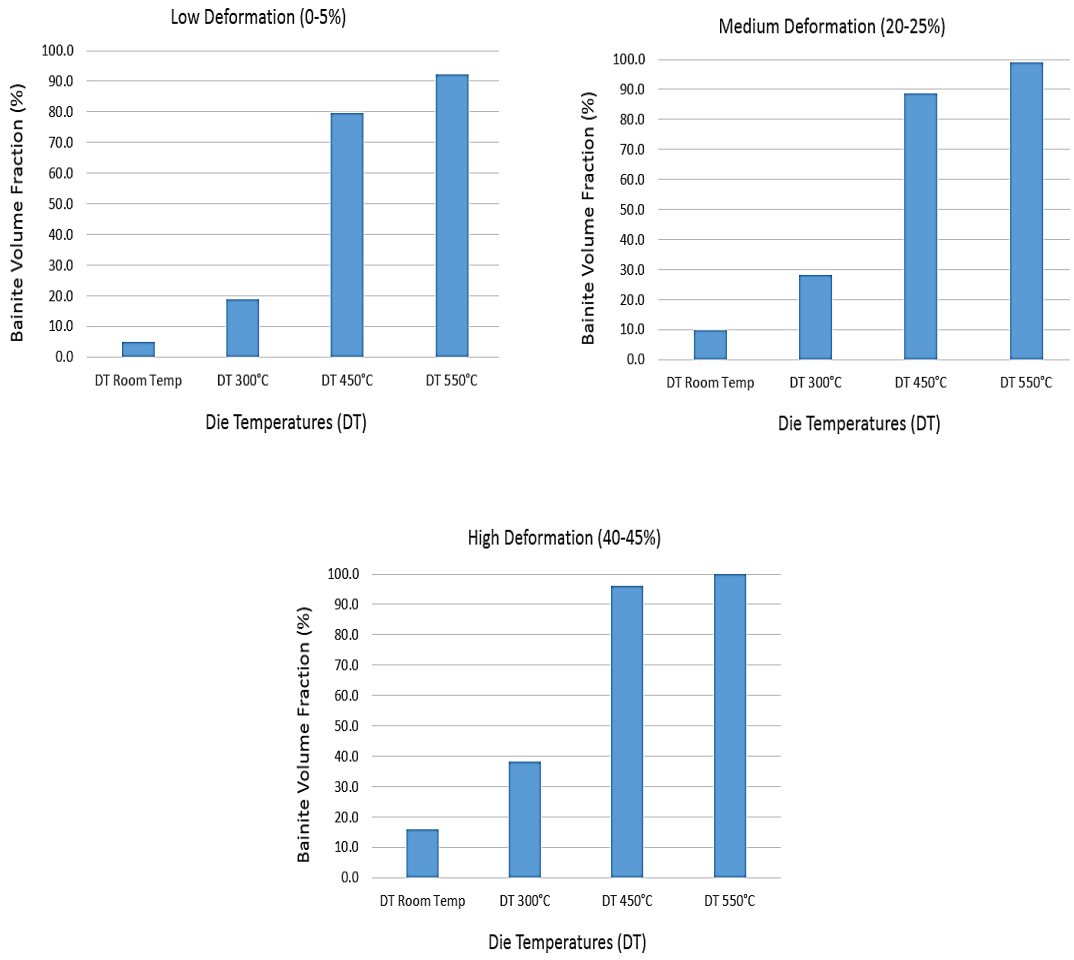

Figure 6.15: Bainite phase volume fractions (%) predicted by the ANN model for different die temperature–deformation amounts (Deformation temp of 800°C)

Most of the decrease in martensite volume fraction is directly compensated by increased bainite volume fractions in the corresponding microstructures. As has been reported in the literature, the increasing deformation amount should have a positive effect on bainite volume fraction at cooling rates above 2-6 °C/s [72, 76]. The cooling rates experienced by the boron steel in heated dies are indeed above

the reported threshold and hence the predictions made by the ANN model are in agreement with what is expected based on physical metallurgy principles. Also for the same die temperatures, it can be observed that increasing the deformation amount leads to higher bainitic content in the final microstructures.

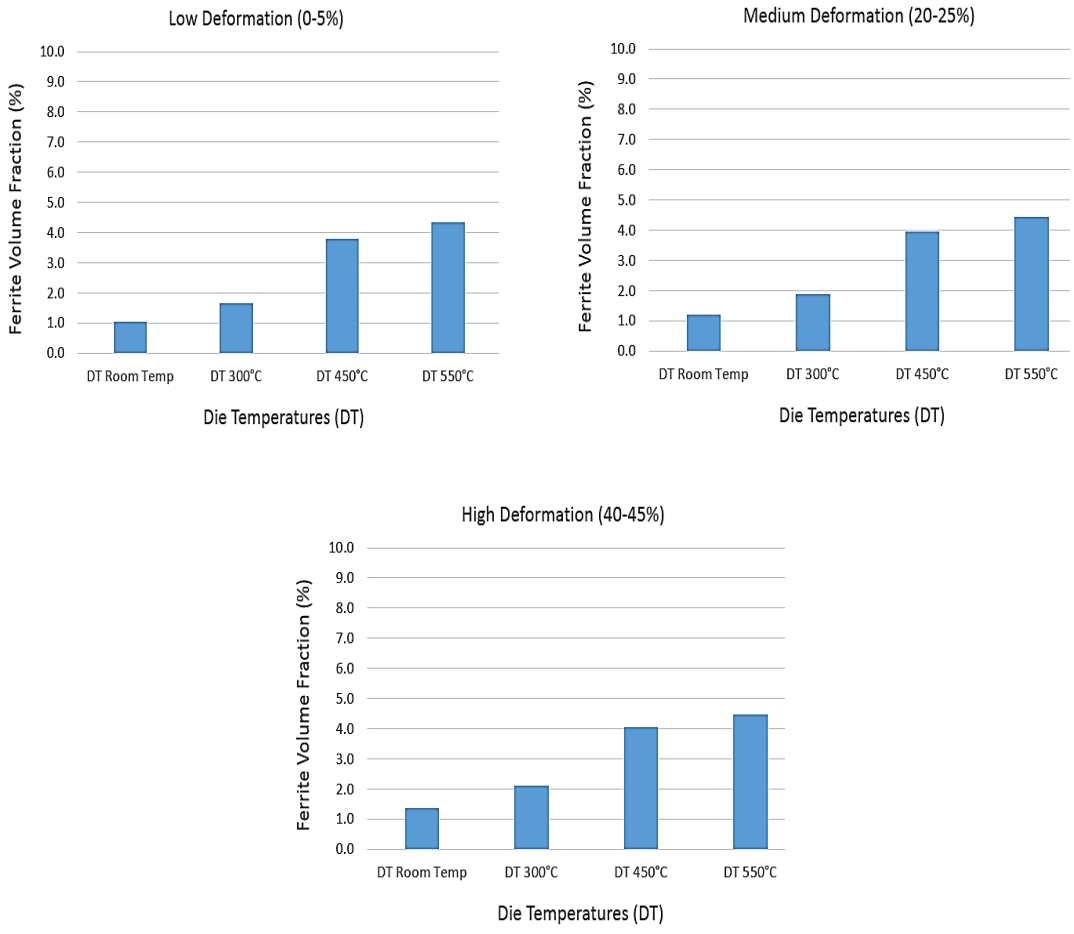

Figure 6.16: Ferrite phase volume fractions (%) predicted by the ANN model for different die temperature–deformation amounts (Deformation temp of 800°C)

Finally the different ferrite volume fractions predicted by the ANN model for

corresponding die temperatures at given deformation amounts (low, medium and high) and fixed deformation temperature (800°C) are given in Figure 6.16. As reported in the literature review, the positive effect of deformation on ferrite formation should be significantly suppressed in hot stamping because of the high strain rates and high deformation temperatures involved [70, 76]. The predictions made by the ANN model are in line with those observations and there was no significant change in the ferrite volume fractions predicted by the ANN model for different die temperatures or different deformation amounts.

Also based on this investigation it can be recommended that using die temperatures in excess of 450°C would lead to heavy bainitic microstructures with greater ductility and lower strength, irrespective of the deformation amount involved (at deformation temperature of 800°C). Similarly using room temperature dies would lead to heavy martensitic microstructures irrespective of the deformation amount involved (at deformation temperature of 800°C). Thus at high deformation temperatures, using dies with these two temperatures in conjunction would allow for the desired tailoring of mechanical properties in the final hot stamped part irrespective of the final part geometry.

This investigation of the ANN model demonstrated its potential for being used to better understand the relationships between the thermo-mechanical history and the final resulting phase distribution in boron steel after tailored hot stamping. It also

showcased how the model can be used for potential *computer aided engineering (CAE)* applications in future for tailored hot stamping process. All the predictions made by the ANN model were based on what it has learnt from the experimental Gleeble data and its predictions being in line with the physical metallurgical principles and trends reported in literature were proof of the robustness and reliability of the final developed ANN model.

In the next and final chapter of this thesis, a concluding summary of this current research project is given. That is followed by a discussion about ideas for future work that can be done for taking this research further and about the scope for industrial impact of this research.

Chapter 7

Conclusions and future scope

7.1 Concluding summary

Producing functionally optimized structural and passenger safety components with tailored mechanical properties is a major challenge facing the automotive industry. Solving it will enable the automotive industry to meet its two main requirements of increased passenger safety and reduced fuel emissions at the same time. Tailoring of mechanical properties in the automobile component by actively dividing the tooling into heated and cooled zones during its hot stamping is one of the most promising approach for developing such *optimized* components. One of the biggest barrier faced by automotive industry for adoption of this process is lack of a reliable model which can accurately quantify the final resulting phase distributions in different regions of a tailor hot stamped component.

The final resulting phase distribution in different regions of a tailor hot stamped component is a result of complex interplay between the thermal and mechanical history of those regions. Most of the existing available models for phase distribution prediction do not account for the effect of deformation on the final

microstructure and thus predictions made by them do not perform well for high deformation regions in the final component [17, 110-112]. The model developed by Tang et al which tried to account for the effect of deformation on the final microstructures in tailor hot stamped parts had limited success for heated dies at high temperatures [114]. Thus developing a reliable and robust phase distribution prediction model for tailored hot stamping which is able to account for both the effect of thermal history and the amount of deformation on the final microstructure was the main research challenge addressed in this thesis.

For developing such a model, an Artificial Neural Network (ANN) based approach was explored in this thesis to address this complex scientific and industrial problem. An ANN based model was developed for tailored hot stamping which uses the thermal history, deformation amount and deformation temperature as inputs for prediction of the final phase distribution. For development of the model, laboratory scale physical simulations of the tailored hot stamping process were done to generate the required data using Gleeble 3500 thermo-mechanical simulator. Then the resulting phase distributions in Gleeble samples were quantified using state of the art scanned surface nanoindentation technique. Metallography and optical microscopy were used to capture microstructural images of Gleeble samples for secondary qualitative analysis. All the data generated from the experimental work was used to prepare the ANN dataset, a part of which (input dataset) was then used for developing the final ANN model.

Once the ANN model had been developed, a rigorous performance analysis and validation of the final ANN model was carried out. The ANN model gave an excellent phase volume fraction prediction performance by having a RMS (Root Mean Square) error of just 5.4% on the input dataset and a RMS error of 7.7% on test dataset. The reliability and robustness of the ANN model was demonstrated by validating its performance against the completely new and independent experimental data; the Gleeble experimental data in the test dataset had never been encountered by the ANN model before and was thus used for validation of the final ANN model. All the predicted phase volume fractions by the model were compared against the actual measured values obtained from nanoindentation testing to establish the accuracy of the predictions made by the model.

The main research findings from this project are as presented below:

1. *Artificial Neural Network (ANN)* based approach was well suited for solving this complex scientific and industrial challenge of final phase distribution prediction in automotive structural and safety components produced by tailored hot stamping process using boron steel.

2. The developed ANN based model for phase distribution prediction during tailored hot stamping was able to successfully account for both the effect of thermal history and the effect of deformation on the final microstructures.

3. The Root Mean Square (RMS) error in phase volume fraction prediction performance of the ANN based model was found to be just 5.4% on the input dataset and 7.7% on the test dataset. This excellent prediction performance of the ANN model helped in establishing its reliability and robustness.

4. This prediction performance of the ANN model was a significant improvement over the currently available existing phase distribution prediction models which use only thermal history for making their phase distribution predictions.

5. Different statistical techniques used during the training and development of the final ANN model helped in making it highly robust and reliable. Application of these statistical techniques is highly recommended, especially when using ANN based modelling in materials science:

    a. The presently developed final ANN model was trained on experimental data generated through laboratory scale physical simulation of tailored hot stamping process using Gleeble 3500 thermo-mechanical simulator. Because of constraints on available experimental resources, data from only 40 Gleeble tests was available for model development. K-fold cross validation technique was used for achieving the full potential of this limited available data from Gleeble tests. This is an excellent statistical technique for the field of empirical modelling in material science, where usually the cost associated with generating experimental

data is high and because of that mostly limited experimental data is available for modelling purpose.

b. The *final ANN model* was actually a committee comprising of 180 different ANN models, the members of which were generated using K-fold cross validation, different network topologies and random weight initializations. Using this approach allowed the final ANN model to robustly learn all the functional relationships present in the input dataset without being limited by a fixed network topology or a fixed random weight initialization. Thus the final ANN model was able to successfully learn all the complex multivariate mathematical relationships between the input thermo-mechanical histories and the corresponding final phase distributions captured in the experimentally generated input dataset used for model development.

c. Also using this committee based approach allowed for calculation of the localized uncertainties in each unique prediction made by the final ANN model. The quantification of uncertainty for each individual prediction was customized for that prediction and reflected the constraint imposed by the limited amount of information captured in the experimentally generated input dataset used for the training and development of the final ANN model.

7.2 Future work and scope for industrial impact

In this thesis a completely new state of the art ANN based empirical model was developed and presented for phase distribution prediction during tailored hot stamping process. This developed final ANN model uses thermal history, amount of deformation and deformation temperature as its input for the final phase distribution prediction in boron steel during tailored hot stamping. These are the factors which have the greatest influence on the final phase distribution during tailored hot stamping and hence were investigated and used during development of the current model. However due to limited availability of experimental resources, the effects of other process parameters such as strain rate, austenitization temperature and austenitization time on the final phase distribution during tailored hot stamping could not be investigated during Gleeble physical simulation experiments in present research. All these process parameters should be investigated and added to the ANN model to gain further incremental improvements in its performance.

The final ANN model developed in this research work uses thermal and mechanical history for predicting final phase distribution in tailored hot stamping process. Accurate thermal and mechanical FE simulation models have already been developed and validated for tailored hot stamping process. This present ANN based phase distribution prediction model can be coupled with such thermal and

mechanical FE simulation models to develop a fully coupled thermal-mechanical-metallurgical model for simulating the complete tailored hot stamping process. Such a fully coupled model can be used for optimizing the tailored hot stamping process for developing tailored structural and safety automotive components with the greatest potential for improvements in light weighting and crash worthiness. Using such fully coupled models for simulation will eliminate the need to carry out expensive experimental investigations required for finding the optimal set of process parameters for achieving the desired tailoring of mechanical properties.

The available final ANN based empirical model can also be further investigated for gaining deeper insights into how varying thermo-mechanical history will affect the final phase distribution in boron steel during tailored hot stamping process. Such investigations can lead to discovery of new trends in the tailored hot stamping process, which can be potentially exploited for gaining further improvements in crash performance and weight reduction goals by the automotive industry. Thus the developed final ANN model in this research addresses a critical scientific and industrial challenge faced by the automotive industry and is well suited for *computer aided engineering (CAE)* applications for tailored hot stamping process in the future.

References:

[1] H. Karbasian and A.E. Tekkaya: A review of hot stamping; *Journal of Materials Processing Technology*, Vol. 210 (15), 2010, pp. 2103-2118

[2] S. Keeler and M. Kimchi: Advanced high-strength steels application guidelines Version 5.0; www.worldautosteel.org, May 2014

[3] J. Zhou, B. Wang and M. Huang: Two constitutive descriptions of boron steel 22MnB5 at high temperature; *Materials and Design*, Vol. 63, 2014, pp. 738-748

[4] R.S. Lee, Y.K. Lin and T.W. Chien: Experimental and theoretical studies on formability of 22MnB5 at elevated temperatures by Gleeble simulator; *Procedia Engineering*, Vol. 81, 2014, pp. 1682-1688

[5] M. Abbasi, M. Naderi and A. Saeed-Akbari: Isothermal versus non-isothermal hot compression process: A comparative study on phase transformations and structure–property relationships; *Materials and Design*, Vol. 45, 2013, pp. 1-5

[6] M. Naderi, M. Ketabchi, M. Abbasi and W. Bleck: Analysis of microstructure and mechanical properties of different high strength carbon steels after hot stamping; *Journal of Materials Processing Technology*, Vol. 211(6), 2011, pp. 1117-1125

[7] A. Saeed-Akbari: Determination of steels microstructural component based on novel characterization techniques; Institute of Ferrous Metallurgy, RWTH Aachen, *Master Thesis*, 2008

[8] A. Bardelcik, C.P. Salisbury, S. Winkler, M.A. Wells and M. J. Worswick: Effect of cooling rate on the high strain rate properties of boron steel; *International Journal of Impact Engineering*, Vol. 37(6), 2010, pp 694-702

[9] M. Merklein and J. Lechler: Determination of Material and Process Characteristics for Hot Stamping Processes of Quenchenable Ultra High Strength steels with Respect to a FE-based Process Design; *SAE International Journal of Materials Manufacturing*, Vol. 1(1) ,2009, pp. 411-426

[10] G. Berglund: The history of hardening of boron steel in Northern Sweden; *Proceedings of 1st International Conference on Hot Sheet Metal Forming of High Performance Steel,* 2008

[11] J. Aspacher: Form hardening concepts; *Proceedings of 1st International Conference on Hot Sheet Metal Forming of High Performance Steel,* 2008

[12] M. Maikranz-Valentin, J. Clobes, M. Schulz, S. Kulp, M.Alsmann and K. Steinhoff: Local characterization of mechanical properties of hot formed parts; *Proceedings of 3rd International Conference on Hot Sheet Metal Forming of High Performance Steel,* 2011

[13] M. Merklein and J. Lechler: Investigation of the thermo-mechanical properties of hot stamping steels; *Journal of Materials Processing Technology*, Vol. 177(1-3), 2006, pp. 452-455

[14] F. Borsetto, A. Ghiotti and S. Bruschi: Investigation of the high strength steel Al–Si coating during hot stamping operations; *Key Engineering Materials*, Vol. 410-411, 2009, pp. 289-296

[15] R. Kolleck, D. Steinhoefer, J.A. Feindt and P. Bruneau: Manufacturing methods for safety and structural body parts for lightweight body design; *International Deep Drawing Research Group Conference Proceedings*, 2004

[16] M. Geiger, M. Merklein, C. Hoff: Basic investigations on the hot stamping steel 22MnB5; *Advanced Materials Research*, Vol. 6-8, 2005, pp. 795-804

[17] R. George, A. Bardelcik and M.J. Worswick: Hot forming of boron steels using heated and cooled tooling for tailored properties: *Journal of Materials Processing Technology,* Vol. 212 (11), 2012, pp. 2386-2399

[18] M. Maikranz-Valentin, U. Weidig, U. Schoof, H. Becker and K. Steinhoff: Components with optimised properties due to advanced thermo-mechanical process strategies in hot sheet metal forming; *Steel Research International*, Vol. 79(2), 2008, pp. 92-97

[19] D. Munera, F. Pinard and L. Lacassin: Very and ultra high strength steels based tailored welded blanks - A step further towards crashworthiness improvement; *SAE Technical Paper 2006-01-1213*, 2006

[20] D. Munera, A. Pic, D. Abou-Khalil, F. Shmit and F. Pinard: Innovative press hardened steel based laser welded blanks solutions for weight savings and crash safety improvements; *SAE International Journal of Materials & Manufacturing*, Vol.1(1), 2009, pp. 472-479

[21] M. Naderi: Hot stamping of ultra high strength steels ; Faculty of Georesources and Materials Engineering, RWTH Aachen, *PhD Thesis*, 2008

[22] B. Abdulhay, B. Bourouga and C. Dessain: Experimental and theoretical

study of thermal aspects of the hot stamping process; *Applied Thermal Engineering,* Vol. 31(5) , 2011, pp. 674-685

[23] J. Lechler and M. Merklein: Hot stamping of ultra strength steels as a key technology for lightweight construction; *Proceedings of the Material Science & Technology Conference MS&T*, 2008 (Pittsburgh, USA)

[24] T. Altan and A.E. Tekkaya: *Sheet Metal Forming Processes and Applications*, ASM International, 2012

[25] K. Mori, S. Maki and Y. Tanaka: Warm and hot stamping of ultra high tensile strength steel sheets using resistance heating; *CIRP Annals — Manufacturing Technology,* Vol. 54 (1), 2005, pp. 209-212

[26] R. Kolleck, R. Veit, H. Hofmann and F. J. Lenze: Alternative heating concepts for hot sheet metal forming; *Proceedings of 1st CHS2 International Conference on Hot Sheet Metal Forming of High-Performance Steel,* 2008

[27] B. A. Behrens, S. Hubner and M. Demir: Conductive heating system for hot sheet metal forming; *Proceedings of 1st International Conference on Hot Sheet Metal Forming of High-Performance Steel,* 2008

[28] A. Naganathan: Hot Stamping of Manganese Boron Steel; Ohio State University, *Masters thesis*, 2010 (Ohio, USA)

[29] R. Kolleck, R. Veit, M. Merklein, J. Lechler and M. Geiger: Investigation on induction heating for hot stamping of boron alloyed steels; *CIRP Annals - Manufacturing Technology,* Vol. 58(1), 2009, pp. 275-278

[30] H. Steinbeiss, H. So, T. Michelitsch and H. Hoffmann: Method for optimizing the cooling design of hot stamping tools; *Production Engineering -Research and Development,* Vol. 1 (2), 2007, pp. 149-155

[31] B. Casas, D. Latre, N. Rodriguez and I. Valls: Tailor made tool materials for the present and upcoming tooling solutions in hot sheet metal forming; *Proceedings of 1st International Conference on Hot Sheet Metal Forming of High-Performance Steel,* 2008

[32] H. Hoffmann, H. So and H. Steinbeiss: Design of hot stamping tools with cooling system; *CIRP Annals - Manufacturing Technology,* Vol. 56(1), 2007, pp. 269-272

[33] R. Kolleck, J. Aspacher and R. Veit: Efficiency of hot forming processes; *Proceedings of 2nd International Conference on Hot Sheet Metal Forming of High-Performance Steel,* 2009

[34] H. So, H. Hoffmann and R. Golle: Blanking of press hardened ultra high strength steel; *Proceedings of 2nd International Conference on Hot Sheet Metal Forming of High-Performance Steel*, 2009

[35] H. So, D. Fabmann, H. Hoffman, R. Golle and M. Schaper: An investigation of the blanking process of the quenchable boron alloyed steel 22MnB5 before and after hot stamping process; *Journal of Materials Processing Technology*, Vol. 212 (2), 2012, pp. 437-449

[36] M. Braun and C. Fritzsche: Joining of Hot Formed Steels; *Proceedings of 2nd International Conference on Hot Sheet Metal Forming of High-Performance Steel,* 2009

[37] J. Faderl, S. Kolnberger, T. Kurz, G. Luckeneder, T. Martenreiter and M. Rosner: Phs ultraform® - continuous galvanizing meets press-hardening; *Proceedings of 2nd International Conference on Hot Sheet Metal Forming of High-Performance Steel,* 2009

[38] R. M. Iyengar, B. Fedewa, Y.W. Wang, D.F. Maatz Jr and R.L. Hughes: Implications of hot stamped boron steel components in automotive structures; *SAE Technical Paper*, 2008-01-0857, 2008

[39] E. P. DeGarmo, J. T. Black and R. A. Kohser: Materials and Processes in Manufacturing; *Wiley (10th Edition),* 2007

[40] F. Han, B. Hwang, D.W. Suh, Z. Wang, D.L. Lee and SJ Kim: Effect of Molybdenum and Chromium on Hardenability of Low-Carbon Boron-Added Steels; *Metals and Materials International*, Vol 14 (6), 2008, pp. 667

[41] F.C. Campbell: Elements of Metallurgy and Engineering Alloys; *ASM International*, 2008

[42] R.E. Smallman and R.J. Bishop. Modern physical metallurgy and materials engineering; *Butterworth Heinemann, 6th edition,* 1999

[43] W.C. Leslie: The Physical Metallurgy of Steels: *McGraw-Hill International Book Company, USA,* 1981

[44] K.E. Thelning: Steel and its Heat Treatment; *Butterworth Heinemann, 2nd edition,* 1984

[45] J.E. Morral and T.B. Cameron: Boron hardenability mechanisms; *Boron in Steel,* 1979

[46] J.E. Morral and T.B.Cameron: A Model for Ferrite Nucleation Applied to Boron Hardenability; *Metallurgical Transactions A*, Vol. 8(11), 1977, pp. 1817-1819

[47] W. Stumpf and K. Banks: The hot working characteristics of a boron bearing and a conventional low carbon steel; *Material Science and Engineering A*, Vol 418 (1-2), 2006, pp. 86-94

[48] G. F. Melloy, P. R. Slimmon and P. P. Podgursky: Optimizing the Boron Effect; *Metallurgical Transactions* , Vol. 4(10), 1973, pp. 2279-2289

[49] X.L. He, Y.Y. Chu and J.J. Jonas: The grain boundary segregation of boron during isothermal holding; *Acta Metallurgica.* Vol. 37(11), 1989, pp. 2905-2916

[50] X.L. He, Y.Y. Chu and J.J. Jonas: The grain boundary segregation of boron during continuous holding; *Acta Metallurgica.* Vol. 37(1), 1989, pp. 147-161

[51] L. Karlsson, H. Nordén and H. Odelius: Non-equilibrium grain boundary segregation of boron in austenitic stainless steel–I. Large Scale segregation behavior; *Acta Metallurgica*, Vol. 36(1), 1988, pp. 1-12

[52] M. Naderi, A. Saeed-Akbari and W. Bleck: The effects of non-isothermal deformation on martensitic transformation in 22MnB5 steel; *Materials Science and Engineering A*, Vol. 487(1-2), 2008, pp. 445-455

[53] M. Naderi, L. Durrenberger, A. Molinari and W. Bleck: Constitutive relationships for 22MnB5 boron steel deformed isothermally at high temperatures; *Materials Science and Engineering A*, Vol. 478(1-2), 2008, pp. 130-139

[54] A. Turetta, S. Bruschi, A. Ghiotti: Investigation of 22MnB5 mechanical and phase transformation behavior at high temperature; *International Deep-drawing Research Group conference proceedings*, 2007

[55] M. Nikravesha, M. Naderi and G.H. Akbari: Influence of hot plastic deformation and cooling rate on martensite and bainite start temperatures in 22MnB5 steel; *Materials Science and Engineering: A*, Vol. 540(1), 2012, pp. 24-29

[56] D. J. Mun, E. J. Shin, Y. W. Choi, J. S. Lee and Y.M. Koo: Effect of cooling rate, austenitizing temperature and austenite deformation on the transformation behavior of high strength boron steel; *Materials Science and Engineering: A*, Vol. 545, 2012, pp. 214-224

[57] P. Namklang and V. Uthaisangsuk: Description of microstructures and mechanical properties of boron alloy steel in hot stamping process; *Journal of Manufacturing Processes*, Vol. 21, 2016, pp. 87-100

[58] F.F. Li, M.W. Fu and J.P. Lin: Effect of cooling path on phase transformation of boron steel 22MnB5 in hot stamping process; *The International Journal of Advanced Manufacturing Technology*, Vol. 81(5), 2015, pp. 1391-1402

[59] T. Nishibata and N. Kojima: Effect of quenching rate on hardness and microstructure of hot-stamped steel; *Journal of Alloys and Compounds*, Vol. 577(1)(15), 2013, pp.S549-S554

[60] K.A. Taylor and S. S. Hansen: The boron hardenability effect in thermomechanically processed, direct-quenched 0.2 Pct C steels; *Metallurgical Transactions A*, Vol. 21(6), 1990, pp. 1697-1708

[61] H.J. Jun, J.S. Kang, D.H. Seo, K.B. Kang and C.G. Park: Effects of deformation and boron on microstructure and continuous cooling transformation in low carbon HSLA steels: *Materials Science and Engineering: A*, Vol. 422(1–2), 2006, pp. 157-162

[62] B. Abdulhay, B. Bourouga and C. Dessain: Experimental and theoretical study of thermal aspects of the hot stamping process; *Applied Thermal Engineering*, Vol. 31(5), 2011, pp. 674-685

[63] T. Svec and M. Merklein: Tailored tempering—heat transfer and resulting properties in dependency of tool temperatures; *Proceedings 3rd International Conference Hot Sheet Metal Forming of High-Performance Steel - CHS*^{2}, 2011

[64] B. Casas, D. Latre, N. Rodríguez and I. Valls: Tailor made tool materials for the present and upcoming tooling solutions in hot sheet metal forming; *Proceedings 1st International Conference Hot Sheet Metal Forming of High-Performance Steel - CHS*^{2}, 2008

[65] A. Turetta, S. Bruschi and A Ghiotti: Investigation of 22MnB5 formability in hot stamping operations; *Journal of Materials Processing Technology*, Vol. 177(1–3), 2006, pp. 396-400

[66] A. Barcellona and D. Palmeri: Effect of Plastic Hot Deformation on the Hardness and Continuous Cooling Transformations of 22MnB5 Microalloyed Boron Steel; *Metallurgical and Materials Transactions*, Vol. 40A, 2009, pp. 1160-1174

[67] J. Min, J. Lin and Y. Min: Effect of thermo-mechanical process on the microstructure and secondary-deformation behavior of 22MnB5 steels;

Journal of Materials Processing Technology, Vol. 213(6), 2013, pp. 818-825

[68] Z. Shi, K. Liu, M. Wang, J. Shi, H. Dong, J. Pu, B. Chi, Y. Zhang and L. Jian: Effect of non-isothermal deformation of austenite on phase transformation and microstructure of 22SiMn2TiB steel; *Material Science and Engineering: A*, Vol. 535, 2012, pp. 290-296

[69] J. Min, J. Lin, Y. Min and F. Li: On the ferrite and bainite transformation in isothermally deformed 22MnB5 steels; *Material Science and Engineering A*, Vol. 550, 2012, pp. 375-387

[70] M. Naderi, M. Ketabchi, M. Abbasi and W. Bleck: Analysis of microstructure and mechanical properties of different boron and non-boron alloyed steels after being hot stamped; *Procedia Engineering*, Vol. 10 , 2011, pp. 460-465

[71] T.Y. Hsu and W.Z. Chen: Effect of austenite strengthening on martensitic and bainitic transformations; *Scripta Metallurgica*, Vol. 21(10) ,1987, pp. 1289-1294

[72] X.J. Jin, N. Min, K.Y. Zheng and T.Y. Hsu: The effect of austenite deformation on bainite formation in an alloyed eutectoid steel; *Material Science and Engineering A*, Vol. 438–440, 2006, pp. 170-172

[73] K. Tsuzaki, K. Fujiwara and T. Maki: Bainite reaction in Fe–Ni–C alloys; *Journal of Materials Transactions*, Vol. 32, 1991, pp. 667-678

[74] L.C.D Fielding: The Bainite Controversy; *Materials Science and Technology*, Vol. 29(4), 2013, pp. 383-399

[75] T.Y. Hsu and Y. Mou: Thermodynamics of the bainitic transformation in Fe-

C alloys; *Acta Metallurgica*, Vol. 32(9), 1984, pp. 1469-1481

[76] M. Nikravesh, M. Naderi, G.H. Akbari and, W. Bleck: Phase transformations in a simulated hot stamping process of the boron bearing steel; *Materials and Design*, Vol. 84, 2015, pp. 18-24

[77] S.B. Singh and H.K.D.H. Bhadeshia: Quantitative evidence for mechanical stabilization of bainite; *Material Science and Technology*, Vol. 12(7), 1996, pp. 610-612

[78] K. Hase, C. Garcia-Mateo and H.K.D.H. Bhadeshia: Bainite formation influenced by large stress; *Material Science and Technology*, Vol. 20(12), 2004, pp. 1499-1505

[79] T.Y. Hsu: Effect of Stress on Bainitic Transformation in Steel; *Acta Metallurgica Sinica,* Vol. 40, 2004, pp. 113-119

[80] M. Naderi and W. Bleck: Martensitic transformation during simultaneous high temperature forming and cooling experiments; *Steel Research. International*, Vol. 78, 2007, pp. 914-920

[81] D.A. Porter and K.E. Easterling: Phase transformation in metals and alloys; *Nelson Thornes Ltd., Cheltenham*, 1992

[82] M. Maalekian, E. Kozeschink, S. Chatterjee and H.K.D.H. Bhadeshia: Mechanical stabilization of eutectoid steel; *Material Science and Technology, Vol. 23*, 2007, pp. 610-612

[83] C. Garcia-Mateo, F.G. Caballero, J. Chao, C. Capdevila and C. Garcia de Andres: Mechanical stability of retained austenite during plastic deformation

of super high strength carbide free bainite steels; *Journal of Material Science*, Vol. 44(17), 2009, pp. 4617-4624

[84] L.X. Du, H.L. Yi, H. Ding, X.H. Liu and G.D. Wang: Effects of Deformation on Bainite Transformation During Continuous Cooling of Low Carbon Steels**;** *International Journal of Iron and Steel Research*, Vol. 13(2), 2006, pp. 37-39

[85] L. He, G. Zhao, H. Li and Nan Xiang : Research on Mechanical Properties of 22MnB5 Steel Quenched in a Steel Die; *Journal of Shanghai Jiaotong University (Science)*, Vol. 16(2), 2011, pp. 129-132

[86] J. Zhou, B. Wang, M. Huang and D. Cui: Effect of hot stamping parameters on the mechanical properties and microstructure of cold-rolled 22MnB5 steel strips; *International Journal of Minerals, Metallurgy and Materials*, Vol. 21(6), 2014, pp. 544-555

[87] S.Watanabe, H.Otani and T. Kunitake: The Influence of Dissolution and Precipitation Behavior of $M_{23}(C, B)_6$ on the Hardenability of Boron Steels; *Transactions of Iron and Steel Institute of Japan*, Vol. 23(2), 1983, pp. 120-127

[88] M. Merklein, M. Wieland, M. Lechner , S. Bruschi and A. Ghiotti: Hot stamping of boron steel sheets with tailored properties - A review; *Journal of Materials Processing Technology*, Volume 228(), 2016, pp. 11-24

[89] M. Merklein and T. Svec: Hot stamping - manufacturing functional optimized components; *Production Process Production Engineering*, Vol. 7(2), 2013, pp. 141-151

[90] A. Ghiotti, D. Pellegrini and S. Bruschi: Feasibility of Producing Tailored Microstructures in Hot Stamped Sheet Components: *Proceedings of International Deep Drawing Research Group Conference* (USA), 2009

[91] K. Mori, T. Maeno and K. Mongkolkaji: Tailored die quenching of steel parts having strength distribution using bypass resistance heating in hot stamping; *Journal of Materials Processing Technology*, Vol. 213(3), 2013, pp. 508-514

[92] J. Bian and H. Mohrbacher: Novel alloying design for press hardening steels with better crash performance; *Proceedings of International Symposium on New Developments in Advanced High-Strength Sheet Steels*, 2013

[93] K. Mori and Y. Okuda; Tailor die quenching in hot stamping for producing ultra-high strength steel formed parts having strength distribution: *CIRP Annals - Manufacturing Technology*, Vol. 59(1), 2010, pp. 291-294

[94] K. Lamprecht, G. Deinzer, A. Stich, J. Lechler, T. Stoehr and M. Merklein; Thermo- mechanical properties of tailor welded blanks in hot sheet metal forming processes: *Proceedings of the International Deep Drawing Research Group Conference (Austria)*, 2010

[95] T. Svec, M. Gruener and M. Merklein: FE-simulation of the heat transfer by defined cooling condition during the hot stamping process; *Key Engineering Materials*, Vol. 473, 2011, pp. 699-706

[96] J. Banik, F.-J. Lenze, S. Sikora and R. Laurenz: Tailored properties—a pivotal question for hot forming; *Proceedings 3rd International Conference Hot Sheet Metal Forming of High-Performance Steel—CHS^2 (Germany)*, 2011

[97] A.N. Kolmogorov: On the Statistical Theory of Crystallization of Metals; *Academy of Sciences USSR, Mathematics Series 1*, 1937, pp. 355-359

[98] W.A Johnson and R.F. Mehl: Reaction kinetics in processes of nucleation and growth; *Transactions of the American Institute of Mining and Metallurgical Engineers*, Vol. 135(8), 1939, pp. 396-415

[99] M. Avrami: Kinetics of phase change I: general theory; *Journal of Chemical Physics*, Vol. 7(12), 1939, pp. 1103-1112

[100] D.P. Koistinen and R.E. Marburger: A general equation describing the extent of the austenite–martensite transformation in pure iron–carbon alloys and plain carbon steel; *Acta Metallurgica*, Vol. 7(1), 1959, pp. 59-60

[101] M. Umemoto, H. Ohtsuka and I. Tamura: Grain size estimation from transformation kinetics; *Acta Metallurgica*, Vol. 34(7), 1986, pp. 1377-1385

[102] T. Reti, L. Horvath and I. Felde: A comparative study of methods used for the prediction of non-isothermal austenite decomposition; *Journal of Materials Engineering and Performance*, Vol. 6(4), 1997, pp. 433-411

[103] Y.T. Zhang, D.Z. Li and Y.Y. Li: Modeling of austenite decomposition in plain carbon steels during hot rolling; *Journal of Materials Processing Technology*, Vol. 171(2), 2006, pp. 175-179

[104] J.S. Kirkaldy and D. Venugopalan: Prediction of microstructure and hardenability in low alloy steels ;*Proceedings of International Conference on Phase Transformations in Ferrous Alloys*, 1983 (Philadelphia USA)

[105] C. Henwood, M. Bibby, J. Goldak and D. Watt: Coupled transient heat

transfer—microstructure weld computations (Part B); *Acta Metallurgica*, Vol. 36(11), 1988, pp. 3037-3046

[106] A.S. Oddy, J.M.J. McDill and L. Karlsson: Microstructural predictions including arbitrary thermal histories, reaustenization and carbon segregation effects ; *Canadian Metallurgical Quarterly*, Vol. 35(3), 1996, pp. 275-283

[107] T. Olsson: An LS-DYNA material model for simulations of hot stamping processes of ultra high strength steels; *Proceedings of 2nd International Conference on Hot Sheet Metal Forming of High-Performance Steel*, 2009 (Lulea, Sweden)

[108] A.E. Tekkaya, H. Karbasian, W. Homberg and M. Kleiner: Thermo-mechanical coupled simulation of hot stamping components for process design; *Production Engineering*, Vol. 1(1), 2007, pp. 85-89

[109] B. Hochholdinger, H. Grass, A. Lipp and P. Hora: Modeling and determination of flow curves for the simulation of hot forming; *Proceedings of International Deep Drawing Research Group (IDDRG) Conference*, 2009 (CO, USA)

[110] P. Akerstrom and M. Oldenburg: Austenite decomposition during press hardening of a boron steel - Computer simulation and test; *Journal of Materials Processing Technology*, Vol. 174(1-3), 2006, pp. 399-406

[111] B.A. Behrens, P. Olle, F. Schafer and C. Schaffner: Numerical Simulation of Microstructural Evolution During Hot Stamping Process; *Proceeding of International Deep Drawing Research Group (IDDRG) Conference*, 2007 (Hungary)

[112] H.H. Bok, M.G. Lee, E.J. Pavlina, F. Barlat and H.D Kim: Comparative study of the prediction of microstructure and mechanical properties for a hot-stamped B-pillar reinforcing part; *International Journal of Mechanical Sciences*, Vol. 53(9), 2011, pp. 744-752

[113] M.V. Li, D.V Niebuhr, L.L. Meekisho and D.G. Atteridge: A Computational model for the prediction of steel hardenability; *Metallurgical and Materials Transactions B*, Vol. 29(3), 1998, pp. 661-672

[114] B.T.Tang, S.Bruschi, A.Ghiotti and P.F.Bariani : Numerical modelling of the tailored tempering process applied to 22MnB5 sheets; *Finite Elements in Analysis and Design*, Vol. 81, 2014, pp. 69-81

[115] W. Tan, Z.Y. Liu, D. Wu and G.D. Wang: Artificial Neural Network Modeling of Microstructure During C-Mn and HSLA Plate Rolling; *Journal of Iron and Steel Research International*, Vol. 16(2), 2009, pp. 80-83

[116] H. Cetinel, H.A. Ozyigit and L. Ozsoyeller: Artificial neural networks modeling of mechanical property and microstructure evolution in the Tempcore process; *Computer and Structures*, Vol. 80 (3-4), 2002, pp. 213-218

[117] A.M Hassan, A. Alrashdan, M.T. Hayajneh and A.T. Mayyas: Prediction of density, porosity and hardness in aluminum–copper-based composite materials using artificial neural network; *Journal of Materials Processing Technology*, Vol. 209(2), 2009, pp. 894-899

[118] C.S. Lee, W. Hwang. H. C. Park and K. S. Han: Static strength and failure mechanism of CFRP under biaxial loadings; *Mechanics of Composite Material*, Vol. 34 (1), 1998, pp. 28-42

[119] H.K.D.H Bhadeshia: Neural Networks in Material science: *Iron Steel Institute of Japan Intl*, Vol. 39(10), 1999, pp. 966-979

[120] Z. Guo and W. Sha: Modelling the correlation between processing parameters and properties of maraging steels using artificial neural network; *Computational Materials Science*, Vol. 29(1), 2004, pp. 12-28

[121] T. Cool. H. K. D. H. Bhadeshia and D. J. C. MacKay: The yield and ultimate tensile strength of steel welds; *Material Science and Engineering A*, Vol. 223(1-2), 1997, pp. 186-200

[122] J. Kusiak and R. Kuziak: Modelling of microstructure and mechanical properties of steel using the artificial neural network; *Journal of Materials Processing Technology*, Vol. 127(1), 2002, pp. 115-121

[123] G. Khalaj, H. Yoozbashizadeh, A. Khodabandeh, A. Nazari : Artificial neural network to predict the effect of heat treatments on Vickers microhardness of low-carbon Nb microalloyed steels; *Neural Computing and Application*, Vol. 22(5), 2013, pp. 879-888

[124] T. Bhattacharyya, S.B. Singh, S. Sikdar(Dey), S. Bhattacharyya, W. Bleck, D. Bhattacharjee: Microstructural prediction through artificial neural network (ANN) for development of transformation induced plasticity (TRIP) aided steel; *Materials Science & Engineering A*, Vol. 565, 2013, pp. 148-157

[125] D. Hughes: Ultra High Strength Steel – Opportunities for lightweight structures using boron steel; *LCVTP Workstream 7 Vehicle Lightweight Structures Report*, WMG – University of Warwick, 2012

[126] Gleeble 3500 System – Thermal-Mechanical Simulator: *http://www.gleeble.com/products/gleeble-3500.html (Accessed Aug'14)*

[127] R.E. Reed-Hill: Physical Metallurgy Principles; *East-West Press (New Delhi), Second Edition,* Reprint 2004

[128] R.W.K. Honeycombe: Steels-microstructure and properties; *Edward Arnold, Second Edition,* 1995

[129] M. Naderi, A. Saeed-Akbari and W. Bleck: Quantitative and qualitative investigation of the heterogeneous microstructures using surface hardness mapping and dilatation data; *Materials Letters 62,* 2008, pp. 1132-1135

[130] International Organization for Standardization: Metallic materials—Instrumented indentation test for hardness and materials parameters; *(ISO 14577),* 2007

[131] A.C. Fischer-Cripps: Nanoindentation; *Springer New York,* 2004

[132] Science City Research Alliance: Advanced, Materials Facilities and Equipment brochure (University of Birmingham & University of Warwick): *http://www2.warwick.ac.uk/fac/cross_fac/sciencecity/programmes/advanced-materials/ (Accessed on Nov'14)*

[133] W.S. Cleveland and C. Loader: Smoothing by local regression – Principles and Methods; *Statistical Theory and Computational Aspects of Smoothing, Physica-Verlag HD* ,1996, pp. 10-49

[134] Locally weighted scatter plot smoothing (Lowess function) – Matlab: http://uk.mathworks.com/help/curvefit/lowess-smoothing.html (Accessed

on Nov'14)

[135] 1-Dimension Data Interpolation (Interp1 function) – Matlab: http://uk.mathworks.com/help/matlab/ref/interp1.html(Accessed on Nov'14)

[136] J. Sola and J. Sevilla: Importance of input data normalization for the application of neural networks to complex industrial problems; *IEEE Transactions on Nuclear Science, Vol. 44 (3)*, 1997, pp. 1464-1468

[137] T. Mitchell: Machine Learning; *McGraw Hill International Edition* (1997)

[138] G. Cybenko: Continuous valued neural networks with two hidden layers are sufficient; *Technical Report, Department of Computer Science, Tufts University(Medford, USA)*, 1988

[139] S. Russel, P. Norvig: Artificial Intelligence – A Modern Approach; *Prentice Hall 3rd Edition* (2009)

[140] Andrew Ng: http://cs229.stanford.edu/notes/cs229-notes1.pdf; *Machine Learning - CS229 Lecture notes*, Stanford University (accessed on Dec'14)

[141] Andrew Ng: https://www.coursera.org/learn/machine-learning; *Machine Learning* (accessed on Jan'14)

[142] M.J. Berry and G. Linoff: Data Mining Techniques; *John-Wiley and Sons (NY)*, 1997

[143] J. Trzaska: Calculation of volume fractions of microstructural components in steels cooled from the austenitizing temperature; *Journal of Achievements in Materials and Manufacturing Engineering*; Vol. 65(1), 2014, pp. 38-44

[144] M. Vasudevan, A.K Bhaduri, B. Raj & K.P. Rao: Delta ferrite prediction in stainless steel welds using neural network analysis and comparison with other prediction methods: *Journal of Materials Processing Technology*; Vol. 142(1), 2003, pp. 20-28

[145] A. Bahrami, S.M Anijdan, H.M Hosseini, A. Shafyei & R. Narimani: Effective parameters modeling in compression of an austenitic stainless steel using artificial neural network; *Computational Materials Science*, Vol. 34(4), 2005, pp. 335-341

[146] W. Horvath, B. Tabernig, E. Werner & P. Uggowitzer: Microstructures and yield strength of nitrogen alloyed super duplex steels; *Acta materialia*, Vol. 45(4), 1997, pp. 1645-1654

[147] A. Bahrami, S.M Anijdan, & A. Ekrami: Prediction of mechanical properties of DP steels using neural network model; *Journal of alloys and compounds*, Vol. 392(1), 2005, pp. 177-182

[148] R. Honysz: Prediction optimization of mechanical properties of ferrite stainless steels after rolling treatment with use of genetic algorithms; *Manufacturing Engineering*, Vol. 68(1), 2015, pp 17-24

[149] T. Henke, M. Bambach, & G. Hirt: Quantification of uncertainties in grain size predictions of a microstructure-based flow stress model and application to gear wheel forging; *CIRP Annals-Manufacturing Technology*, Vol. 62(1), 2013, pp. 287-290